

NORTHWESTERN UNIVERSITY

Modeling of the Detection of
Surface-Breaking Cracks by Laser Ultrasonics

A DISSERTATION

SUBMITTED TO THE GRADUATE SCHOOL
IN PARTIAL FULFILLMENT OF THE REQUIREMENTS

for the degree

DOCTOR OF PHILOSOPHY

Field of Mechanical Engineering

By

Irene Arias

EVANSTON, ILLINOIS

June 2003

© Copyright by Irene Arias 2003
All Rights Reserved

ABSTRACT

Modeling of the Detection of Surface-Breaking Cracks by Laser Ultrasonics

Irene Arias

A model for the Scanning Laser Source (SLS) technique, a novel laser-based inspection method for the ultrasonic detection of small surface-breaking cracks, is presented. The modeling approach is based on the decomposition of the field generated by a line-focused laser in a half-space containing a surface-breaking crack, by using linear superposition of the incident and the scattered fields. The incident field is that generated by laser illumination of a defect-free half-space. A model which accounts for the effects of thermal diffusion and optical penetration, as well as the finite width of the line-source and the duration of the laser pulse, is formulated, and solved by Fourier–Laplace transform techniques. The inversion of the transforms is performed numerically. The well-known dipole model follows from appropriate limits, and it is shown by simple elasticity arguments that the strength of the dipole can be related a-priori to the heat input and certain material properties. Some illustrative results provide insight on the relevance of the different mechanisms that have been taken into account in the model. The scattered field incorporates the interactions of the incident field with the surface-breaking crack. It is analyzed numerically by the boundary element method. A simple and elegant technique for the treatment of non-decaying Rayleigh waves propagating along the unbounded surface of a half-spaces is developed and verified. An efficient practical implementation of

the method is obtained by an application of the reciprocal theorem of elastodynamics. A computational exploration of the acoustic emissions from nucleating cracks which benefits from this numerical technique is presented. Simulations of the SLS technique are compared with an experiment for a large defect, showing that the model captures the observed phenomena. An example for a small crack illustrates the ability of the SLS technique to detect small defects, beyond the sensitivity of conventional ultrasonic methods.

ACKNOWLEDGEMENTS

I am most grateful to my advisor Professor Jan D. Achenbach for his dedicated guidance and support. Working with him has been a very enriching experience, which has inspired me in many ways. I would also like to thank the members of the committee Professors Sridhar Krishnaswamy, Brian Moran, and John G. Harris.

The discussions and experimental results provided by Younghoon Sohn and Professor Krishnaswamy are gratefully acknowledged, as well as the computing resources generously provided by Professors Wing Kam Liu and Ted Belytschko. I am most thankful for the financial support of the BSCH/Fulbright program.

I want to thank Professor Todd W. Murray and Dr. John C. Aldrin for their guidance in the initial stages of this work. I would also like to thank my officemates Anping, Carmen, Joon, Yi, and Younghoon for their friendship, and Jandro for his emphatic optimism. From the other side of the bridge, Hiroshi Kadowaki deserves special thanks for his endless patience and kindness.

It has been a privilege to share so many moments with Arancha and Mark. I am very grateful for their warm welcoming and the true friendship they have offered since then. I have enjoyed very much watching their family grow with James and Lucas.

I would like to thank my family and friends for their unconditional support and love, and most of all Marino, my companion and soulmate.

Contents

Abstract	iii
Acknowledgments	v
Contents	vi
List of Figures	viii
List of Tables	xii
1 Introduction	1
1.1 Motivation	1
1.2 The Scanning Laser Source (SLS) technique	3
1.3 Outline	6
2 Thermoelastic Generation of Ultrasound by Line-Focused Laser Irradiation	8
2.1 Introduction	9
2.2 Generation mechanisms and heat source representation	13
2.3 Equivalent Dipole Loading	15
2.4 Formulation and solution of the thermoelastic problem	20
2.4.1 Governing Equations	20
2.4.2 Line-source on an isotropic half-space	22
2.5 Summary of the relevant models	27
2.6 Representative Results	29
2.6.1 Quantitative comparison with experiment	29
2.6.2 The effect of thermal diffusion	31
2.6.3 The effect of the width of the line-source and the duration of the laser pulse	35
2.6.4 Distribution of stresses	37
2.7 Conclusions	43

3	Rayleigh wave correction for the BEM analysis of two-dimensional elastodynamic problems in a half-space	45
3.1	Introduction	46
3.2	Formulation	50
3.2.1	Reciprocity theorem in time-harmonic elastodynamics	50
3.2.2	Asymptotic behavior of the displacement far-field solution	51
3.2.3	Matching with the far-field solution at the ends of the computational boundary	54
3.2.4	Integral over the omitted part of the infinite boundary	56
3.3	Numerical implementation	58
3.4	Numerical results	63
3.4.1	Free Rayleigh pulse problem	64
3.4.2	Transient Lamb's problem	68
3.5	Conclusions	72
4	Modeling of the Scanning Laser Source technique	74
4.1	Introduction	75
4.2	The incident field	81
4.3	The scattered field	89
4.4	Representative examples	94
4.4.1	Comparison with experiment for a large notch	94
4.4.2	SLS simulation for a small surface-breaking crack	98
4.5	Conclusions	100
5	Modeling of acoustic emission from surface-breaking and buried cracks	103
5.1	Introduction	104
5.2	Modeling approach	107
5.3	Numerical simulations	110
5.4	Conclusions	115
6	Conclusions	117
	References	121

List of Figures

1.1	Configuration for the SLS technique. Three positions of the laser line-source (I,II, and III) are displayed.	3
1.2	Characteristic time signal recorded at receiver for three different positions of the laser source relative to the crack. Copyright 2000 © The American Society for Nondestructive Testing, Inc. Reprinted from Kromine <i>et al</i> (2000a) with permission from Materials Evaluation. . .	4
1.3	Experimental signatures of the defect in the ultrasonic amplitude (left) and the maximum frequency (right) of the generated signal as the laser source scans over a surface-breaking crack. Copyright 2000 © The American Society for Nondestructive Testing, Inc. Reprinted from Kromine <i>et al</i> (2000a) with permission from Materials Evaluation.	4
2.1	Spatial and temporal profile of the heat source due to line-focused laser illumination.	15
2.2	Elementary surface disk (a), schematic of forces acting on the surrounding material (b) and schematic of point-source superposition (c).	17
2.3	Schematic summary of the relevant models.	28
2.4	Key features of the Rayleigh pulse used for the quantitative comparison.	31
2.5	Vertical displacement on the surface calculated with model B (solid line) and model D (dashed line). The numbers next to the waveforms indicate the distance in mm from the axis of the laser line-source. The labels L, S and R denote longitudinal, shear and Rayleigh surface waves, respectively.	33
2.6	Vertical displacement on the epicentral axis calculated with model B (solid line) and model D (dashed line). The numbers next to the waveforms indicate the depth in mm.	35
2.7	Influence of the width of the line-source (a) and the duration of the laser pulse (b) on the vertical displacement waveform at the epicentral axis.	36

2.8	Snapshots of the stress components σ_{11} (top), σ_{33} (middle) and σ_{31} (bottom) due to the laser line-source at times 0.01 (left), 0.02 (center-left), 0.15 (center-right) and 0.2 μs (right), computed for $R_G = 0.45$ mm and $\nu = 10$ ns. The region shown corresponds to 1 mm in depth per 1 mm to the right of the epicentral axis. Positive normal stresses indicate compression.	38
2.9	Stress component σ_{11} on the surface. The legend indicates the distance to the epicentral axis. A positive value indicates compression.	41
2.10	Stress component σ_{11} on the epicentral axis. The legend indicates the depth. A positive value indicates compression.	41
2.11	Stress component σ_{33} on the epicentral axis. The legend indicates the depth. A positive value indicates compression.	42
3.1	Schematic definition of the computational domain. $\Gamma^\pm = \Gamma_\infty^\pm \cup \Gamma_0^\pm \cup \Gamma_1^\pm$	53
3.2	Time signal at $x_1 = 0.5\lambda_R$ (λ_R is the Rayleigh wavelength for the central frequency) for the free Rayleigh pulse problem. The solid line corresponds to the analytical solution. The dashed line and the circles correspond to the truncated and the corrected BEM models, respectively.	66
3.3	Time signal at the truncation point ($x_1 = 10\lambda_R$, λ_R being the Rayleigh wavelength for the central frequency) for the free Rayleigh pulse problem. The solid line corresponds to the analytical solution. The dashed line and the circles correspond to the truncated and the corrected BEM models, respectively.	67
3.4	Schematic of Lamb's problem with Gaussian spatial distribution.	68
3.5	Time signal at $x_1 = 45\lambda_R$ (λ_R is the Rayleigh wavelength for the central frequency) for the transient Lamb's problem with Gaussian spatial distribution. The solid line corresponds to the analytical solution. The dashed line and the circles correspond to the truncated and the corrected BEM models, respectively.	70
3.6	Time signal at the truncation point ($x_1 = 60\lambda_R$, λ_R being the Rayleigh wavelength for the central frequency) for the transient Lamb's problem with Gaussian spatial distribution. The solid line corresponds to the analytical solution. The dashed line and the circles correspond to the truncated and the corrected BEM models, respectively.	71
4.1	Configuration for the SLS technique.	76
4.2	Decomposition of the total field into incident and scattered fields	78

4.3	Normal displacement on the surface. The numeric labels next to the waveforms indicate the distance in mm from the axis of the laser line-source. The labels L, S and R denote longitudinal, shear and Rayleigh surface waves, respectively. A negative value represents an inward normal displacement.	86
4.4	Stress σ_{11} on the surface. The legend indicates the distance to the epicentral axis. A negative value indicates compression.	87
4.5	Tractions on the vertical plane at 0.05 mm (left) and 1.4 mm (right) distance from the axis of the laser line-source at various depths. The numbers next to the waveforms indicate the depth in mm. A negative normal traction indicates compression and a positive shear traction on the top face of an element points in the negative x_1 direction. . . .	88
4.6	Decomposition into the symmetric and the anti-symmetric problems in a quarter-space.	90
4.7	Experimental setup for the SLS inspection of a notched specimen. . .	95
4.8	Experimental (left column) and simulated (right column) signals detected at the receiver when the laser is located at distances of 3 mm, 2 mm and 1 mm from the left face of the notch.	96
4.9	Experimental (left column) and simulated (right column) signals detected at the receiver when the laser is located at distances of 0.75 mm, 0.5 mm and 0.25 mm from the left face of the notch.	97
4.10	Experimental (left) and simulated (right) peak-to-peak amplitude vs. position of the source relative to the crack (SLS position).	98
4.11	Configuration for the SLS technique. Three positions of the laser line-source (I,II, and III) are displayed.	99
4.12	Characteristic time signal at receiver simulated for three different positions of the laser source relative to the crack.	100
4.13	Simulated signatures of the defect in the ultrasonic amplitude (left) and the maximum frequency (right) of the generated signal as the laser source scans over a surface-breaking crack.	101
5.1	Modeling approach to the nucleation of surface-breaking and buried cracks.	107
5.2	Modeling approach to the propagation of surface-breaking and buried cracks.	108
5.3	Regularized S-shaped step	109
5.4	Surface normal displacement due to the acoustic emission from the nucleation of a very small surface-breaking crack ($a = 10\mu\text{m}$) at a distance of 12.0 mm from the plane of the crack. The labels L, S and R denote longitudinal, shear and Rayleigh surface waves, respectively.	110

5.5	Surface normal displacement due to the acoustic emission from the nucleation of surface-breaking cracks of different lengths a at 16.0 mm distance from the plane of the crack.	111
5.6	Surface normal displacement due to the acoustic emission from the propagation of a surface-breaking crack ($a = 1.0\text{mm}$) for different growth lengths Δa , at distances of 3 mm (left) and 16 mm (right) from the plane of the crack.	112
5.7	Surface normal displacement due to the acoustic emission from the nucleation of buried cracks of different lengths a at a distance of 5.0 mm from the plane of the crack. The midpoints of the cracks are located at a depth $d = 5.0$ mm beneath the surface.	113
5.8	Surface normal displacement due to the acoustic emission from the propagation of a buried crack ($a = 1.0$ mm and $d = 0.5$ mm) for different growth lengths Δa , at distances of 4 mm (left) and 16 mm (right) from the plane of the crack.	114
5.9	Surface normal displacement due to the acoustic emission from the nucleation of buried cracks of length $a = 1.0$ mm at a distance of 5.0 mm from the plane of the crack. The midpoints of the cracks are located at different depths d beneath the surface.	115
5.10	Surface normal displacement due to the acoustic emission from the nucleation of a buried crack ($a = 1.0$ mm and $d = 1.0$ mm) at different distances from the plane of the crack.	116

List of Tables

2.1 Values of the key features of the Rayleigh waveform. 31

Chapter 1

Introduction

1.1 Motivation

Ultrasound has been extensively used in nondestructive evaluation (NDE) techniques in a wide range of applications, in particular the detection and characterization of defects. An incident ultrasonic wave package is scattered by the presence of flaws in the specimen, such as discontinuities, cracks, voids, and inclusions. This scattered field carries information about the geometry of these anomalies. It is the purpose of ultrasound based quantitative nondestructive techniques to infer precise information about the size and location of the defect by monitoring their interactions with ultrasound.

Over the last decades, lasers have emerged as a powerful tool to generate and detect ultrasound. Laser based ultrasonic techniques provide a number of advantages over conventional ultrasonic methods such as higher spatial resolution, noncontact generation, and detection of ultrasonic waves, as well as the ability to operate on curved or rough surfaces (Scruby and Drain, 1990). Depending on the level of energy density deposited by the laser, ultrasound is generated by two different mechanisms:

ablation at very high power, and thermoelastic processes at moderate power operation. The latter mechanism does not damage the surface of the specimen and is therefore suitable for NDE applications.

Ultimately, an ultrasound-based nondestructive inspection technique produces experimental waveforms, which must be analyzed. Quantitative information can be statistically extracted from an extensive set of experimental data. Nevertheless, it is generally agreed that a model which reproduces the processes involved in the experimental technique is a key element in the interpretation of experimental records, and the identification of characteristic features in the signal. Thus, the inspection process greatly benefits from predictive models which allow not only to enhance the performance of existing experimental techniques, but also to select and design the inspection system to be used in a particular situation. Moreover, models are fundamental tools for the solution of inverse problems from quantitative data (Thompson and Gray, 1986).

The main practical objective of the present work is to develop a model for an ultrasonic technique for the detection of surface-breaking cracks, the Scanning Laser Source (SLS) technique recently proposed by Kromine et al. (2000a). In order to identify the relevant physical mechanisms responsible for the observed behavior, the fundamental thermoelastic processes involved in the generation of ultrasound by lasers are studied in detail. On the other hand, the numerical methods we have developed for the analysis of the interactions of ultrasound with surface-breaking cracks are well-suited for other ultrasonic nondestructive techniques, such as acoustic emission.

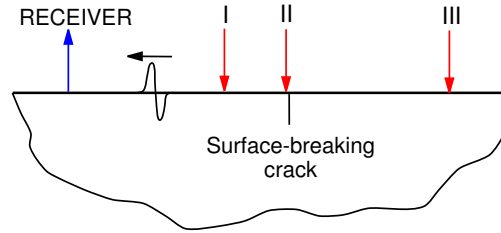


Figure 1.1: Configuration for the SLS technique. Three positions of the laser line-source (I,II, and III) are displayed.

1.2 The Scanning Laser Source (SLS) technique

Conventional techniques for the detection of surface-breaking cracks rely on monitoring the reflections (pulse-echo) or the changes in the amplitude of the transmission (pitch-catch) of a given well-defined incident signal caused by the presence of a defect. However, for small defects as compared to the wavelength of the generated Rayleigh wave, these reflections and changes in the transmission are often too weak to be detected with existing laser detectors. By contrast, the Scanning Laser Source (SLS) technique monitors the changes in the laser generated ultrasonic signal as the laser source passes over the discontinuity. There is experimental evidence that this alternative method is able to detect very small cracks, beyond the sensitivity of traditional pulse-echo and pitch-catch methods, as well as cracks of arbitrary orientation with respect to the direction of scanning (Kromine et al., 2000b).

The SLS technique employs a line-focused high-power laser source which is swept across the test specimen and passes over surface-breaking anomalies (Kromine et al., 2001; Fomitchov et al., 2002). The generated ultrasonic waves are detected with a laser interferometer located either at a fixed distance from the laser source or at a fixed position on the test specimen. Figure 1.1 sketches the inspection technique,

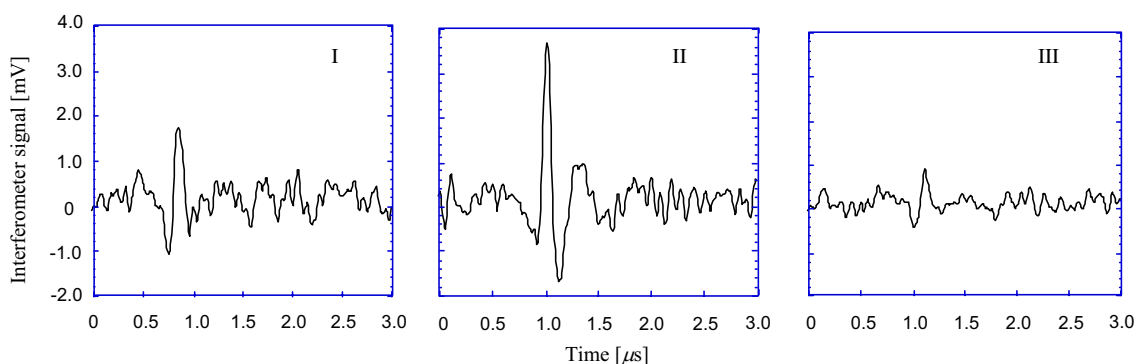


Figure 1.2: Characteristic time signal recorded at receiver for three different positions of the laser source relative to the crack. Copyright 2000 © The American Society for Nondestructive Testing, Inc. Reprinted from Kromine *et al* (2000a) with permission from Materials Evaluation.

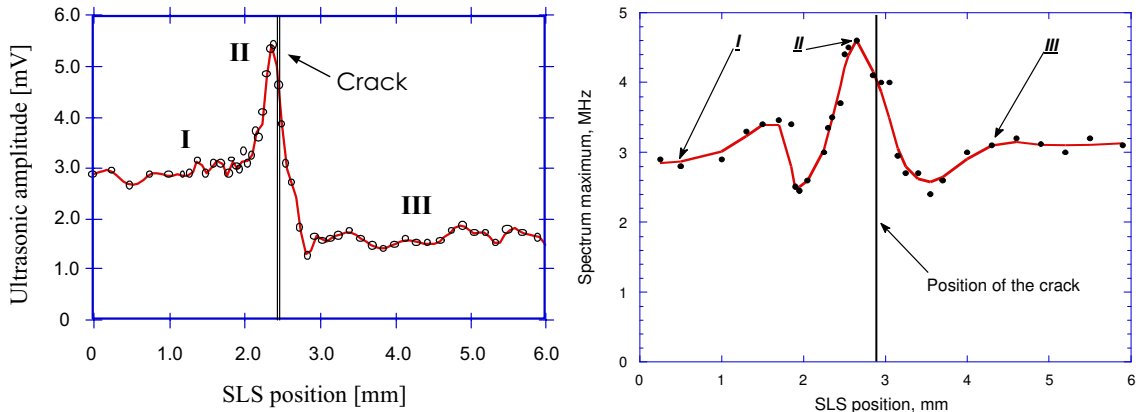


Figure 1.3: Experimental signatures of the defect in the ultrasonic amplitude (left) and the maximum frequency (right) of the generated signal as the laser source scans over a surface-breaking crack. Copyright 2000 © The American Society for Nondestructive Testing, Inc. Reprinted from Kromine *et al* (2000a) with permission from Materials Evaluation.

where three representative positions of the source relative to the crack are shown: (I) far ahead, (II) very near, and (III) behind the defect. The recorded time signals at the receiver when the laser is located at these positions are presented in Fig. 1.2. The evolutions of the peak-to-peak amplitude and the frequency content of these signals as the laser is swept across the crack have been studied, and specific signatures indicating the presence of a defect have been identified. The left plot in Fig. 1.3 shows the peak-to-peak amplitude as a function of the position of the laser. Two plateaux can be observed far ahead and, at a lower level, behind the position of the crack. As the line-focused laser approaches the crack, the peak-to-peak amplitude increases, reaching a maximum slightly ahead of the crack. Then, this amplitude rapidly drops to the lower value of the second plateau. This lower peak-to-peak amplitude is due to the scattering of the signal by the crack. The difference between the two plateaux levels is related to the size of the crack as compared to the Rayleigh wavelength. This characteristic signature of the defect is attributed to (a) interactions of the direct ultrasonic wave with the reflections from the crack, and (b) changes in the generation conditions when the laser source is in the vicinity of the crack.

As can be noted from Fig. 1.2, the increase in the peak-to-peak amplitude near the crack is sufficiently large to be easily differentiated from the background noise, unlike the weak echoes from the crack in the signal corresponding to position (I). This illustrates the enhanced sensitivity of the SLS technique as compared to conventional methods.

1.3 Outline

Chapter 2 deals with the generation of ultrasound by line-focused laser illumination of a homogeneous, isotropic, linearly elastic half-space. The source representation accounts for optical penetration of the energy deposited by the laser, as well as the finite width and duration of the laser source. The thermoelastic nature of the generation process is included in the governing one-way coupled equations of generalized thermoelasticity. The plane strain initial-boundary value problem is analyzed semi-analytically by the use of double integral transforms which are inverted numerically (see Section 4.2). The relation between the obtained solutions and those resulting from a simplified point-source representation of the thermal loading is investigated. The effects of the finite width of the illumination strip and the finite duration of the laser pulse are studied in detail, as well as the effect of thermal diffusion. Selected results provide physical insight into the generation process and illustrate the resulting fields.

Next, the interaction of the laser-generated ultrasonic waves with surface-breaking cracks is analyzed numerically by the boundary element method. The analysis of wave propagation in two-dimensional elastic half-spaces presents some difficulties, due to the propagation of non-decaying Rayleigh waves along the unbounded surface. A simple and elegant treatment of this issue is developed and verified in Chapter 3. This method exploits the knowledge of the far-field asymptotic behavior of the solution. An efficient practical implementation of the method is obtained by an application of the reciprocal theorem of elastodynamics. The modeling of the SLS is presented in Chapter 4. By virtue of linear superposition, the total field is decomposed into the incident field and the scattered field. The incident field is that

generated by the line-focused laser source in the uncracked half-space, and follows from the model in Chapter 2. The scattered field incorporates the interactions of this incident field with the defect, and is analyzed with the technique developed in Chapter 3. Illustrative numerical results, as well as comparisons with experimental data are reported.

Finally, the acoustic emissions from surface-breaking and buried cracks are explored numerically with the boundary element method in Chapter 5. This analysis benefits from the technique developed in Chapter 3. It is shown that in the limit of a small nucleating surface-breaking crack, the surface disturbances tend to those generated by a shear dipole at the surface, which is also a common point-source representation for a line-focused pulsed laser. We have analyzed the effect of the size of the nucleating crack, as well as the surface disturbances for various observation locations.

Chapter 2

Thermoelastic Generation of Ultrasound by Line-Focused Laser Irradiation

A two-dimensional theoretical model for the field generated in the thermoelastic regime by line-focused laser illumination of a homogeneous, isotropic, linearly elastic half-space is presented. The model accounts for the effects of thermal diffusion and optical penetration, as well as the finite width and duration of the laser source. The model is obtained by solving the thermoelastic problem in plane strain, rather than by integrating available solutions for the point-source, leading to a lower computational effort. The well-known dipole model follows from appropriate limits. However, it is shown that, by simple elasticity arguments, the strength of the dipole can be related a-priori to the heat input and certain material properties. The strength is found to be smaller than that of the dipoles equivalent to a buried source due to the effect of the free surface. This fact has been overlooked by some previous researchers. Excellent quantitative agreement with experimental observations provides validation for the model. Some representative results are presented to

illustrate the generated field and provide insight into the relevance of the different mechanisms taken into account in the model.

2.1 Introduction

The irradiation of the surface of a solid by pulsed laser light generates wave motion in the solid material. Since the dominant frequencies of the generated wave motion are generally above 20,000 Hz, the waves are not audible to the human ear, and they are therefore termed ultrasonic waves. There are generally two mechanisms for such wave generation, depending on the energy density deposited by the laser pulse. At high energy density a thin surface layer of the solid material melts, followed by an ablation process whereby particles fly off the surface, thus giving rise to forces which generate the ultrasonic waves. At low energy density the surface material does not melt, but it expands at a high rate and wave motion is generated due to thermoelastic processes. As opposed to generation in the ablation range, laser generation of ultrasound in the thermoelastic range does not damage the surface of the material. For applications in nondestructive evaluation (NDE), ultrasound generated by laser irradiation in the thermoelastic regime is of interest and will be dealt with in this paper.

The generation of ultrasound by laser irradiation provides a number of advantages over conventional generation by piezoelectric transducers. These are: higher spatial resolution, non-contact generation and detection of ultrasonic waves, use of fiber optics, narrow-band and broad-band generation, absolute measurements, and ability to operate on curved and rough surfaces and at hard-to-access locations.

On the receiving side, surface ultrasonic waves can be detected using piezoelectric (PZT) or EMAT transducers, or optical interferometers in a completely laser-based system. Ultrasound generated by laser irradiation contains a large component of surface wave motion, and is therefore particularly useful for the detection of surface-breaking cracks. A Scanning Laser Source technique (SLS) has been proposed by Kromine et al. (2000a) for this purpose.

Since White (1963) first demonstrated the generation of high frequency acoustic pulses by laser irradiation of a metal surface, considerable progress has been made in developing theoretical models to explain and provide fruitful interpretation of experimental data. Scruby et al. (1980) assumed that, in the thermoelastic regime, the laser heated region in the metal sample acts as an expanding point volume at the surface, which then was postulated to be equivalent to a set of two mutually orthogonal force dipoles. Based on intuitive arguments, these authors related the strength of the dipoles to the heat input and certain physical properties of the material. In this manner, the thermoelastic circular source was reduced to a purely mechanical point-source acting on the surface of the sample. This point-source representation neglected optical absorption of the laser energy into the bulk material and thermal diffusion from the heat source. Furthermore, it did not take account of the finite lateral dimensions of the source. Rose (1984) gave a rigorous mathematical basis for the point-source representation on an elastic half-space, which he called a Surface Center of Expansion (SCOE), starting from a general representation theorem for volume sources. Although a formal expression for the double (Hankel-Laplace) transformed solution was given, its inverse could only be determined in a convenient analytical form for special configurations.

The SCOE model predicts the major features of the waveform and agrees with experiments particularly well for highly focused and short laser pulses. However, it fails to predict the so-called precursor in the ultrasonic epicentral waveform. The precursor is a small, but relatively sharp initial spike observed in metals at the longitudinal wave arrival. Doyle (1986) proved that the presence of the precursor in metals is due to subsurface sources equivalent to those arising from thermal diffusion. Although the focus was on metallic materials, these results showed that the precursor is present whenever subsurface sources exist. In metals, the subsurface sources arise mainly from thermal diffusion, since the optical absorption depth is very small compared to the thermal diffusion length.

The early work discussed above, suggested that a complete theory based on the treatment of the thermoelastic problem was necessary in order to provide understanding of the characteristics of the generated waveforms and assess the approximations introduced in the formulation of previously proposed models. Based on previous work by McDonald (1989), Spicer (1991) used the generalized theory of thermoelasticity to formulate a realistic model for the circular laser source, which accounted for both thermal diffusion and the finite spatial and temporal shape of the laser pulse.

All the works cited to this point deal with the modeling for a circular spot of laser illumination. One major problem associated with laser ultrasonics is poor signal to noise ratio. By focusing the laser beam into a line rather than a circular spot, the signal to noise ratio can be improved, since more energy can be injected into the surface while keeping the energy density low enough to avoid ablation. In addition, the generated surface waves have almost plane wavefronts parallel to

the line-source, except near the ends of the line, which is advantageous for surface crack sizing and for material characterization. Therefore, line-sources are used in inspection techniques such as the Scanning Laser Source technique for detection of surface-breaking cracks (Kromine et al., 2000a).

Although the laser line-source offers several advantages, it has received considerably less attention than the circularly symmetric source. Three-dimensional representations for a line of finite width and length can be derived by superposition of surface centers of expansion. In some particular situations, when the effects of thermal diffusion and optical penetration can be neglected and interest is directed only to specific features of the generated field, such as surface wave displacements for instance (Doyle and Scala, 1996), the superposition can be performed readily by analytical integration of the formal expressions put forth by Rose (1984). However, in more general cases, when the finite size of the laser source and the effects of thermal diffusion and optical penetration are accounted for, no analytical solution is available in the physical domain. Then, the superposition has to be performed numerically, resulting in a considerable computational effort. For these more general cases, a two-dimensional approach in which the line-source is considered to be infinitely long becomes highly advantageous. Bernstein and Spicer (2000) formulated a two-dimensional representation for an infinitely long and thin line-source. Their model results in a line of force dipoles acting normal to the line of laser illumination. Thus, they did not consider neither thermal diffusion nor optical penetration nor the finite width of the laser line-source.

In this paper we derive a two-dimensional model for the line-source based on a unified treatment of the corresponding thermoelastic problem in plane strain,

rather than integration of available results for the point-source. As opposed to Bernstein and Spicer (2000), this model takes account of the finite width of the source, the shape of the pulse and the subsurface sources arising from thermal diffusion and optical penetration. The thermoelastic problem in an isotropic half-space is solved analytically in the Fourier-Laplace transform domain. The doubly transformed solution is inverted numerically to produce theoretical waveforms. This approach alleviates much of the computational effort required by the superposition of point-source solutions.

2.2 Generation mechanisms and heat source representation

Several physical processes may take place when a solid surface is illuminated by a laser beam depending on the incident power (Scruby and Drain, 1990). Here only low incident powers will be considered, since high powers produce damage on the material surface rendering the technique unsuitable for nondestructive testing. At low incident powers the laser source induces heating, the generation of thermal waves by heat conduction, and the generation of elastic waves (ultrasound). In materials such as semiconductors, electric current may be caused to flow.

For application in NDE, generation of elastic waves is required in the ultrasonic frequency range and with reasonable amplitudes. This can be achieved without damage of the material surface only with short-pulsed lasers. The majority of published work has employed Q-switched laser pulses of duration of 10 – 40 ns. A suitable expression for the heat deposition in the solid along an infinitely long line

is

$$q = \hat{E}(1 - R_i)\gamma e^{-\gamma x_3} f(x_1)g(t), \quad (2.1)$$

with

$$f(x_1) = \frac{1}{\sqrt{2\pi}} \frac{2}{R_G} e^{-2x_1^2/R_G^2}, \quad (2.2)$$

and

$$g(t) = \frac{8t^3}{v^4} e^{-2t^2/v^2}, \quad (2.3)$$

where \hat{E} is the energy of the laser pulse per unit length, R_i is the surface reflectivity, R_G is the Gaussian beam radius, v is the laser pulse risetime (full width at half maximum), and γ is the extinction coefficient. The temporal and spatial profiles are schematically shown in Fig. 2.1. The coordinate axis x_1 and x_3 are directed along the surface, perpendicular to the line-source and normal inwards from the surface, respectively.

Equation (2.1) represents a strip of illumination since it is defined by a Gaussian in x_1 . The Gaussian does not vanish completely with distance, but its value becomes negligible outside a strip. The source is spread out in time according to the function proposed by Schleichert et al. (1989). For both the temporal and the spatial profile, the functional dependence has been constructed so that in the limit $v \rightarrow 0$ and $R_G \rightarrow 0$ an equivalent concentrated line-source is obtained

$$q = \hat{E}(1 - R_i) \delta(x_3) \delta(x_1) \delta(t). \quad (2.4)$$

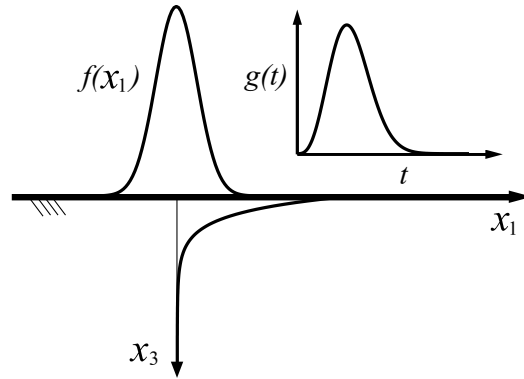


Figure 2.1: Spatial and temporal profile of the heat source due to line-focused laser illumination.

2.3 Equivalent Dipole Loading

It is well established that a thermoelastic source at a point in an unbounded medium can be modeled as three mutually orthogonal dipoles (Achenbach, 1973). The magnitude of the dipoles D depends on the temperature change and certain mechanical and thermal constants of the material. On the basis of intuitive arguments, Scruby and Drain (1990) postulated that when the source is acting at a point on the surface, the dipole directed along the normal to the surface vanishes and only the dipoles on the surface remain, their strength left unaltered.

We propose a simple approach to derive the magnitude of the surface dipoles. First we simplify the heat deposition process. We consider an instantaneous ($\nu \rightarrow 0$) point-source ($R_G \rightarrow 0$ in the expression for the corresponding circularly symmetric Gaussian distribution) and assume that all the energy is absorbed at the surface ($\gamma \rightarrow \infty$). The expression for q then adopts the form, in cylindrical coordinates,

$$q = E(1 - R_i) \frac{\delta(r)}{2\pi r} \delta(x_3) \delta(t), \quad (2.5)$$

where E now represents total energy rather than energy per unit length. This expression can be interpreted as the energy deposited in an infinitesimal circular disc of radius r_0 and depth l_3 , which both tend to zero. Equation (2.5) then becomes

$$q = E(1 - R_i) \frac{1}{\pi r_0^2} \frac{1}{l_3} \delta(t). \quad (2.6)$$

In addition heat conduction or heat propagation is neglected, so that the equation for the temperature reduces to

$$\frac{\dot{T}}{\kappa} = \frac{E}{k} (1 - R_i) \frac{1}{\pi r_0^2} \frac{1}{l_3} \delta(t), \quad (2.7)$$

where T represents the absolute temperature, k is the thermal conductivity and κ is the thermal diffusivity such that $\kappa = k/(\rho c_V)$, ρ and c_V being the density and the specific heat of the material at constant deformation, respectively. Hence the temperature increment in the surface element is

$$\Delta T = \frac{E}{\rho c_V} (1 - R_i) \frac{1}{\pi r_0^2} \frac{1}{l_3} H(t). \quad (2.8)$$

Since the dimension of $E/\rho c_V$ is temperature·(length)³, Eq. (2.8) has the proper dimension for ΔT . Since heat conduction is not considered, the temperature increment ΔT is maintained at its initial level.

When the laser impinges the surface of the half-space, the very thin circular surface element undergoes thermal expansion due to a temperature increment of ΔT . The element is located at the surface and therefore the normal stress in the x_3 direction is zero. The elementary disc is shown in Fig. 2.2(a). If the element is

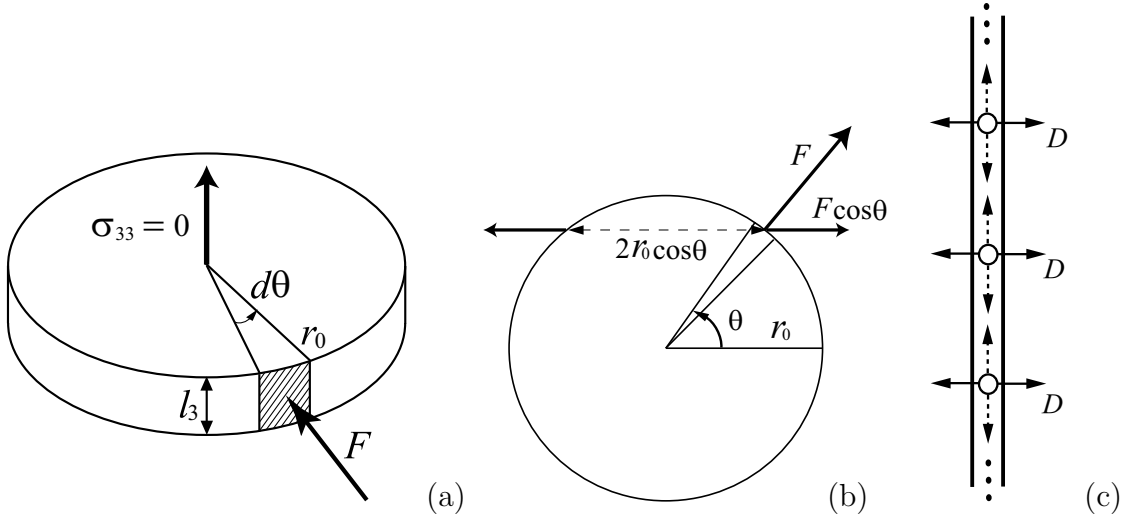


Figure 2.2: Elementary surface disk (a), schematic of forces acting on the surrounding material (b) and schematic of point-source superposition (c).

removed from the half-space, it can deform freely in its plane, so that the strains in the radial and circumferential directions are $\alpha_T \Delta T$, where α_T is the coefficient of linear thermal expansion. To place the element back into the half-space we consider the same surface element subjected to an imposed deformation in its plane of the same magnitude but opposite sign. Let us call this imposed state of strain $\bar{\varepsilon}_{rr} = \bar{\varepsilon}_{\theta\theta} = -\alpha_T \Delta T = \varepsilon$. The corresponding normal stress in the x_3 direction is

$$\sigma_{33} = (\lambda + 2\mu) \varepsilon_{33} + 2\lambda \varepsilon = 0, \quad (2.9)$$

and thus

$$\varepsilon_{33} = -\frac{2\lambda}{\lambda + 2\mu} \varepsilon. \quad (2.10)$$

Hence

$$\begin{aligned}
\sigma_{rr} &= 2(\lambda + \mu) \varepsilon + \lambda \varepsilon_{33} = \frac{2\mu(3\lambda + 2\mu)}{\lambda + 2\mu} \varepsilon = -\frac{2\mu}{\lambda + 2\mu} (3\lambda + 2\mu) \alpha_T \Delta T \equiv \sigma, \\
\sigma_{\theta\theta} &= \sigma, \\
\sigma_{r\theta} &= 0,
\end{aligned} \tag{2.11}$$

where the relevant expression for ΔT is given by Eq. (2.8). The reaction of the state of stress given in Eq. (2.11) on the surface of the hole, shown in Fig. 2.2(b), is equivalent to that produced by two orthogonal dipoles of magnitude D . As illustrated in Fig. 2.2(a), the force acting on an elementary sector of the circular disc is directed along its normal and its magnitude is

$$F = \sigma dS = l_3 \sigma r_0 d\theta. \tag{2.12}$$

Consider now two orthogonal directions defined by $\theta = 0$ and $\theta = \pi/2$ in the plane of the element. As shown in Fig. 2.2(b), the component along one of these directions ($\theta = 0$) of the force acting on the surrounding material is given by $F \cos \theta$. The elementary dipole is obtained multiplying by the separation of the corresponding elementary forces, i.e. $2r_0 \cos \theta$, as

$$dD = 2r_0 F \cos^2 \theta, \tag{2.13}$$

and hence, integration along the half-circumference of the hole yields

$$D = \int_{-\pi/2}^{\pi/2} 2r_0^2 l_3 \sigma \cos^2 \theta d\theta = \pi r_0^2 l_3 \sigma. \tag{2.14}$$

Thus, finally

$$D = -\frac{2\mu}{\lambda + 2\mu} (3\lambda + 2\mu) \alpha_T \frac{E}{\rho c_V} (1 - R_i) H(t). \quad (2.15)$$

The same result is obtained for the dipole in the $\theta = \pi/2$ direction.

The dipole has dimension force-length. Note that Eq. (2.15) coincides with that given by Scruby and Drain (1990) except for the factor $2\mu/(\lambda + 2\mu)$. For materials such as aluminum for which $\lambda \simeq 2\mu$, this factor is approximately 0.5. The simple derivation presented above shows that, contrary to the conclusion by Scruby and Drain (1990), the free surface does in fact reduce the strength of the surviving dipoles by a factor of $2\mu/(\lambda + 2\mu)$. In a recent work, Royer (2001) reached the same conclusion by comparing a model for an infinitely long and thin line-source based on a mixed matrix formulation to the line-source representation obtained by superposition of point-sources.

Based on the same arguments, the line-source can be modeled as a line of dipoles acting on the surface perpendicularly to the axis of the line. The strength of the dipole can also be derived following simple elasticity arguments, by obtaining the lateral stresses acting on a very thin surface element which is submitted to ΔT and is laterally constrained. The resulting expression for the strength of the dipole coincides with that given in Eq. (2.15) for the point-source where, for this case, E and D , redefined as \hat{E} and \hat{D} , have to be understood as magnitudes per unit length. This result is not surprising if the line-source is viewed as a superposition of point-sources as shown in Fig. 2.2(c). The dipoles directed along the axis of the line cancel out, leaving only the dipoles directed normal to the line, their magnitude being unchanged.

2.4 Formulation and solution of the thermoelastic problem

In this section we present the governing equations of the thermoelastic problem with a brief discussion about the appropriate heat conduction representation. We then describe the solution procedure for line illumination of an isotropic half-space. The extension of the formulation to plates is straightforward.

2.4.1 Governing Equations

The thermoelastic fields are governed by the coupled equations of thermoelasticity. Based on the hyperbolic generalized theory of thermoelasticity, the governing equations for an isotropic solid are

$$k\nabla^2 T = \rho c_V \tau \ddot{T} + \rho c_V \dot{T} + T_0 \beta \nabla \cdot \dot{\mathbf{u}} - q \quad (2.16)$$

$$\mu \nabla^2 \mathbf{u} + (\lambda + \mu) \nabla (\nabla \cdot \mathbf{u}) = \rho \ddot{\mathbf{u}} + \beta \nabla T \quad (2.17)$$

where T_0 is the ambient temperature, \mathbf{u} is the displacement vector field, τ is the material relaxation time, β is the thermoelastic coupling constant: $\beta = (3\lambda + 2\mu)\alpha_T$. In the thermoelastic regime the heat produced by mechanical deformation, given by the term $T_0 \beta \nabla \cdot \dot{\mathbf{u}}$ can be neglected. With this approximation, Eq. (2.16) reduces to

$$\nabla^2 T - \frac{1}{\kappa} \dot{T} - \frac{1}{c^2} \ddot{T} = -\frac{q}{k}, \quad c^2 = \frac{k}{\rho c_V \tau}. \quad (2.18)$$

The mathematical expression for q for the case of a line-source is given in Eq (2.1). Equation (2.18) is hyperbolic because of the presence of the term \ddot{T}/c^2 . On the other hand, its counterpart in the classical theory, i.e. Eq. (2.18) without the term \ddot{T}/c^2 is parabolic. In the parabolic description of the heat flow, an infinite heat propagation speed is predicted, while the hyperbolic description introduces a finite propagation speed c , which is not known.

Both the classical and hyperbolic heat equations have been used to model thermoelastic laser generated ultrasound. As an accurate determination of the temperature field is vital to accurate predictions of laser generated ultrasonic waves, the question of which equation should be used arises naturally, and has been addressed in the literature by Sanderson et al. (1997).

In order to provide an answer to the question which equation should be used for our particular modeling purposes, the temperature field generated by line illumination of a half-space has been determined based on the two heat equations. Unlike the hyperbolic solution, the classical solution shows no distinct wavefront and temperature increase starts at the initial time as expected. However, the differences in the predicted temperature between the two theories are small and only apparent for very small time scales (in the order of hundred picoseconds). In the case of laser generation of ultrasound for NDE applications, we are typically interested in time scales of the order of microseconds. These time scales are large enough for the solutions given by both theories to be numerically undistinguishable. Consequently, the selection of the theory for the time scales of interest can be done for convenience, with no practical effect on the calculated results. Likewise, the choice of a specific value for the heat propagation speed in the hyperbolic equation does not

affect the results. From the practical point of view, the choice of a value for the heat propagation speed equal to the speed of the longitudinal waves in the hyperbolic formulation presents some numerical advantages in that it simplifies the inversion of the transforms. It is therefore adopted in this paper.

2.4.2 Line-source on an isotropic half-space

The system of governing equations, which we consider in the plane strain approximation for the case of an infinitely long line-source, must be supplemented by initial and boundary conditions. The initial conditions are that the half-space is initially at rest. The boundary conditions include thermal and mechanical conditions. If the boundary is defined by $x_3 = 0$, then the considered thermal boundary condition is

$$\frac{\partial T}{\partial x_3} = 0 \quad \text{at } x_3 = 0. \quad (2.19)$$

This condition implies that heat does not flow into or out of the half-space via the boundary. The heat that is generated by the laser is deposited inside the half-space just under the surface. The mechanical condition is that the tractions are zero on the surface ($x_3 = 0$). The tractions follow from the stress-strain relation

$$\sigma_{ij} = \lambda \delta_{ij} \epsilon_{kk} + \mu (u_{i,j} + u_{j,i}) - \beta \delta_{ij} \Delta T. \quad (2.20)$$

The term $\beta\delta_{ij}\Delta T$ represents the volumetric stress induced by the temperature change. The conditions of vanishing tractions on the surface become

$$\sigma_{31} = \mu(u_{3,1} + u_{1,3}) = 0 \quad \text{at } x_3 = 0, \quad (2.21)$$

$$\sigma_{33} = \lambda(u_{1,1} + u_{3,3}) + 2\mu u_{3,3} - \beta\Delta T = 0 \quad \text{at } x_3 = 0. \quad (2.22)$$

Equation (2.16) without the mechanically induced heat source, Eq. (2.17) and Eq. (2.18) with the above boundary and initial conditions are solved using standard Fourier-Laplace transform techniques for two-dimensional, time dependent systems. First of all, the problem is reformulated in terms of the usual displacement potentials. The elastic displacements may be expressed as

$$\mathbf{u} = \nabla\phi + \nabla \times \boldsymbol{\psi} \quad (2.23)$$

where ϕ is the dilatational potential and $\boldsymbol{\psi} = \nabla \times (0, 0, \psi)$ is the rotational potential. These potentials satisfy the following wave equations

$$\nabla^2\phi - a^2\ddot{\phi} = \frac{a^2\beta}{\rho} T, \quad (2.24)$$

$$\nabla^2\psi - b^2\ddot{\psi} = 0, \quad (2.25)$$

where $a = 1/c_L$ and $b = 1/c_T$ are the slownesses of the longitudinal and the transverse waves, respectively. The exponential Fourier transform in the spatial coordinate x_1 and the one-sided Laplace transform in time are then applied to the governing equations, and the boundary and initial conditions. In the transformed

domain the thermoelastic problem may then be written as

$$(p^2 + a^2 s^2 + \frac{s}{\kappa})\tilde{T} - \frac{\partial^2 \tilde{T}}{\partial x_3^2} = \frac{\tilde{q}}{k}, \quad (2.26)$$

$$(p^2 + a^2 s^2)\tilde{\phi} - \frac{\partial^2 \tilde{\phi}}{\partial x_3^2} = -\frac{a^2 \beta}{\rho} \tilde{T}, \quad (2.27)$$

$$(p^2 + b^2 s^2)\tilde{\psi} - \frac{\partial^2 \tilde{\psi}}{\partial x_3^2} = 0, \quad (2.28)$$

with the transformed boundary conditions

$$\frac{\partial \tilde{T}}{\partial x_3} = 0 \quad \text{at } x_3 = 0, \quad (2.29)$$

$$\tilde{\sigma}_{33} = \mu \left[\frac{b^2}{a^2} \left(\frac{\partial^2}{\partial z^2} - p^2 \right) \tilde{\phi} + 2p^2 \left(\tilde{\phi} + \frac{\partial \tilde{\psi}}{\partial z} \right) \right] - \beta \tilde{T} = 0 \quad \text{at } x_3 = 0, \quad (2.30)$$

$$\tilde{\sigma}_{31} = \mu i p \left[2 \frac{\partial \tilde{\phi}}{\partial z} + \left(\frac{\partial^2}{\partial z^2} + p^2 \right) \tilde{\psi} \right] = 0 \quad \text{at } x_3 = 0, \quad (2.31)$$

where (t, s) is the Laplace pair and (x, p) is the Fourier pair. The Laplace transformed and the Fourier transformed variables are denoted with an bar and a tilde, respectively. The initial conditions for the transformed potentials are that the body is at rest prior to $t = 0$. The thermal problem defined by Eqs. (2.26) and (2.29) with the corresponding initial conditions may be solved first for the transformed temperature distribution \tilde{T} . This transformed temperature distribution serves as a source term for Eqs. (2.27) and (2.28). The transformed potentials can then be obtained by solving the problem defined by Eqs. (2.27), (2.28), (2.30) and (2.31) with the corresponding initial conditions. The expressions for the transformed displacements

and stresses can be derived from the solution for the transformed potentials as:

$$\tilde{u}_1 = -ip \left[Ae^{-\zeta x_3} - \frac{2\zeta\eta}{\eta^2 + p^2} Ae^{-\eta x_3} + \tilde{\phi}_0 \right], \quad (2.32)$$

$$\tilde{u}_3 = -\zeta Ae^{-\zeta x_3} + \frac{2\zeta p^2}{\eta^2 + p^2} Ae^{-\eta x_3} + \tilde{\phi}'_0, \quad (2.33)$$

$$\tilde{\sigma}_{11} = \mu \left[\zeta \Upsilon(\zeta) Ae^{-\zeta x_3} + \frac{4\zeta\eta p^2}{\eta^2 + p^2} Ae^{-\eta x_3} + \tilde{\phi}_1 \right], \quad (2.34)$$

$$\tilde{\sigma}_{33} = \mu \left[(\eta^2 + p^2) Ae^{-\zeta x_3} - \frac{4\zeta\eta p^2}{\eta^2 + p^2} Ae^{-\eta x_3} + (\eta^2 + p^2) \tilde{\phi}_0 \right], \quad (2.35)$$

$$\tilde{\sigma}_{31} = 2\mu ip \left[\zeta A(e^{-\eta x_3} - e^{-\zeta x_3}) + \tilde{\phi}'_0 \right], \quad (2.36)$$

where

$$A = \frac{(\eta^2 + p^2)^2}{R} \Gamma \frac{\gamma^2}{\gamma^2 - \xi^2} \left\{ \frac{\kappa}{s} \left[\frac{1}{\zeta} - \frac{1}{\xi} \right] + \frac{1}{\zeta^2 - \gamma^2} \left[\frac{1}{\zeta} - \frac{1}{\gamma} \right] \right\}, \quad (2.37)$$

$$\tilde{\phi}_0 = \Gamma \frac{\gamma^2}{\gamma^2 - \xi^2} \left\{ \frac{\kappa}{s} \left[\frac{e^{-\xi x_3}}{\xi} - \frac{e^{-\zeta x_3}}{\zeta} \right] + \frac{1}{\zeta^2 - \gamma^2} \left[\frac{e^{-\gamma x_3}}{\gamma} - \frac{e^{-\zeta x_3}}{\zeta} \right] \right\}, \quad (2.38)$$

$$\tilde{\phi}'_0 = \Gamma \frac{\gamma^2}{\gamma^2 - \xi^2} \left[\frac{\kappa}{s} (e^{-\zeta x_3} - e^{-\xi x_3}) + \frac{e^{-\zeta x_3} - e^{-\gamma x_3}}{\zeta^2 - \gamma^2} \right], \quad (2.39)$$

$$\begin{aligned} \tilde{\phi}_1 = \Gamma \frac{\gamma^2}{\gamma^2 - \xi^2} & \left\{ \frac{\kappa}{s} [\Upsilon(\xi)e^{-\xi x_3} - \Upsilon(\zeta)e^{-\zeta x_3}] \right. \\ & \left. + \frac{\Upsilon(\gamma)e^{-\gamma x_3} - \Upsilon(\zeta)e^{-\zeta x_3}}{\zeta^2 - \gamma^2} \right\}, \end{aligned} \quad (2.40)$$

with $\zeta^2 = p^2 + a^2 s^2$, $\eta^2 = p^2 + b^2 s^2$, $\xi^2 = \zeta^2 + \frac{s}{\kappa}$ and $\Upsilon(h) = (b^2 s^2 - 2h^2)/h$. Also, $R = (\eta^2 + p^2)^2 - 4\zeta\eta p^2$, $\Gamma = \beta Q_0 Q_p(p) Q_s(s)/(\lambda + 2\mu)$ and

$$Q_0 = \frac{\hat{E}}{k} (1 - R_i), \quad (2.41)$$

$$Q_p(p) = \frac{1}{\sqrt{2\pi}} e^{-p^2 R_G^2/8}, \quad (2.42)$$

$$Q_s(s) = \mathcal{L} \left\{ \frac{8t^3}{v^4} e^{-2t^2/v^2} \right\}, \quad (2.43)$$

where \mathcal{L} indicates Laplace transform. The solution in the transformed domain is then inverted numerically. The integral of the inverse Fourier transform is evaluated by using a Romberg integration routine with polynomial extrapolation (Press et al., 1986). The general method used for the numerical inversion of the Laplace transform is based on a technique developed by Crump (1976).

It is of interest to point out that taking the appropriate limits for an instantaneous ($v \rightarrow 0$) infinitely thin ($R_G \rightarrow 0$) line-source with no optical penetration ($\gamma \rightarrow \infty$) and no thermal diffusion ($\xi^2 \rightarrow s/\kappa$) the dipole model is recovered. In the above mentioned limits, Eq. (2.36) takes the form

$$\tilde{\sigma}_{31} = -\frac{2\mu}{\lambda + 2\mu} (3\lambda + 2\mu) \alpha_T \frac{\hat{E}}{\rho c_V} (1 - R_i) \frac{ip}{s}. \quad (2.44)$$

By defining

$$\hat{D} = -\frac{2\mu}{\lambda + 2\mu} (3\lambda + 2\mu) \alpha_T \frac{\hat{E}}{\rho c_V} (1 - R_i), \quad (2.45)$$

Eq. 2.44 may be rewritten as

$$\tilde{\sigma}_{31} = \hat{D} \frac{ip}{s}. \quad (2.46)$$

The inversion of the Fourier and Laplace transforms yields

$$\sigma_{31} = \hat{D} \delta'(x_1) H(t), \quad (2.47)$$

which may be identified as the shear stress induced by a suddenly applied force dipole of magnitude \hat{D} acting on the surface. Taking into account Eq. (2.45) yields

the same expression for the strength of the dipole as given in Eq. (2.15).

2.5 Summary of the relevant models

The relationships between the different models considered in the present work are schematically summarized in Fig. 2.3. Model A corresponds to the complete thermoelastic problem (including thermal diffusion) with a volumetric source (accounting for optical penetration). From this model, model B is obtained by neglecting optical penetration and thus confining the thermoelastic source to the surface. The problem is still thermoelastic.

On the other hand, model C can be obtained from the complete model A by neglecting thermal diffusion. In this manner, the heat equation can be integrated directly. Therefore, the problem may be considered as equivalent to a purely elastic problem. The source term for the elastic problem obtained by integrating Eq. (2.7) can be understood as a mechanical volumetric source. Model D can be derived in two different ways, namely by neglecting thermal diffusion in model B or by neglecting optical penetration in model C. In both cases, the resulting model corresponds to the purely elastic problem of a purely mechanical surface load. The shape of the source in the spatial variable x_1 and in time is the same as the one for the complete model (model A) but is confined to the surface. By concentrating the source to an instantaneous line-source, i.e. by assuming a delta function dependence in both space and time, the shear traction dipole model (model E) is obtained. The procedure of deriving the shear traction dipole model (model E) from the complete model (model A) by neglecting thermal diffusion and optical penetration and concentrat-

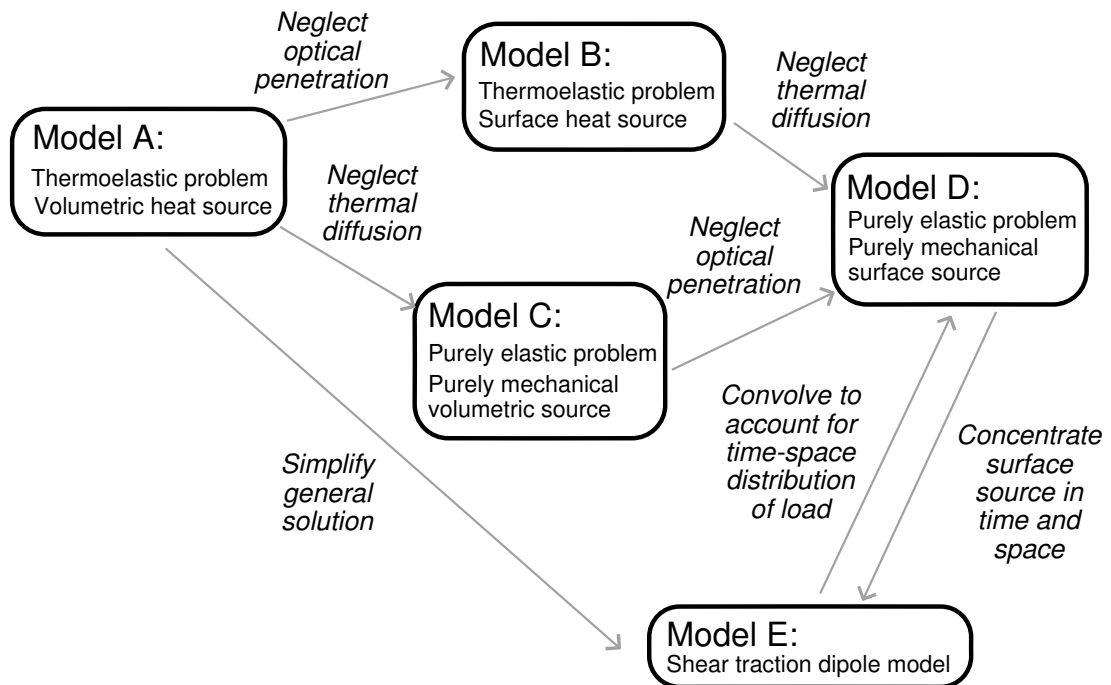


Figure 2.3: Schematic summary of the relevant models.

ing the source in space and time has been demonstrated in detail in the previous section.

It is obvious that model D may also be obtained from the shear stress dipole model by a convolution with the spatial and temporal distribution of the source. In this sense, the shear traction dipole can be understood as providing a fundamental solution for the purely elastic problem with a surface mechanical load, i.e. when thermal diffusion and optical penetration are neglected.

2.6 Representative Results

In this section we present some relevant results obtained with the models described in the previous section. Unless stated otherwise, the values used for the material properties correspond to aluminum alloy 2024-T6 and are: $c_L = 6.321 \text{ mm}/\mu\text{s}$, $c_T = 3.11 \text{ mm}/\mu\text{s}$, $\alpha_T = 2.2 \cdot 10^{-5} \text{ 1/K}$, $\kappa = 6.584 \cdot 10^{-5} \text{ mm}^2/\mu\text{s}$, $k = 160 \text{ W/mK}$, $R_i = 91\%$, $\gamma = 2 \cdot 10^8 \text{ 1/m}$. The values used for the parameters of the laser are: $E = 1 \text{ mJ}$ per unit length of the line-source, $R_G = 0.45 \text{ mm}$ and $v = 10 \text{ ns}$.

2.6.1 Quantitative comparison with experiment

There are not many experimental measurements of ultrasonic waves generated by laser line-sources available in the literature. Most of the data focuses on surface displacements, which are mainly due to the Rayleigh wave. Doyle and Scala (1996) report data of normal surface displacements of Rayleigh waves in an aluminium alloy at several distances along an axis perpendicular to the line-source. They also give precise values of the material properties and the characteristics of the

laser source. In this section we present a quantitative comparison between the experimental waveforms reported by Doyle and Scala (1996) and the theoretical waveforms computed with the thermoelastic model (model B). This comparison has been performed without adjusting any parameter in the model to obtain quantitative agreement. Rather, values for the parameters of the thermoelastic model have been taken directly from the experiments. These values are: $c_L = 6.42 \text{ mm}/\mu\text{s}$, $\lambda = 57.69 \text{ GPa}$, $\mu = 26.45 \text{ GPa}$, $\alpha_T = 2.3 \cdot 10^{-5} \text{ 1/K}$, $\kappa = 9.8 \cdot 10^{-5} \text{ mm}^2/\mu\text{s}$, $k = 2.38 \cdot 10^2 \text{ W/mK}$, $R_i = 91\%$, $E = 2.9 \text{ mJ}$ per unit length of the line-source, $R_G = 10 \text{ }\mu\text{m}$ and $v = 75 \text{ ns}$.

Although the length of the line is obviously finite (20 mm) in the experiment, the distances of the observation points are close enough for the line-source to be considered infinitely long without significant loss of accuracy. Therefore, as expected for a line-source, the experimental Rayleigh surface wave appears as a monopolar inward displacement which agrees qualitatively with predictions of the thermoelastic model ($x_1 = 2.5 \text{ mm}$ in Fig. 2.5). The quantitative comparison with the experiment has been based on three key features of the Rayleigh pulse shown in Fig. 2.4, namely the peak amplitude A , the full width of the pulse at $1/e$ of the peak amplitude τ_1 , and the duration of the pulse τ_0 . The experimental and the calculated values for these parameters are listed in Table 2.1. In every case the calculated values are within experimental uncertainty which is evidence of the excellent quantitative agreement between experiment and model.

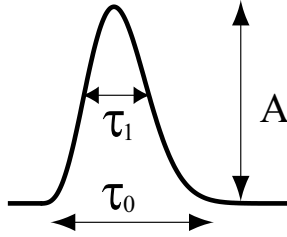


Figure 2.4: Key features of the Rayleigh pulse used for the quantitative comparison.

Table 2.1: Values of the key features of the Rayleigh waveform.

	experiment	theory
A	$0.37 \pm 10\%$ nm	0.35 nm
τ_1	$63 \pm 10\%$ ns	65 ns
τ_0	$185 \pm 5\%$ ns	180 ns

2.6.2 The effect of thermal diffusion

In order to identify the effects of thermal diffusion on the predicted waveforms, calculations provided by the model that includes thermal diffusion (model B) are compared with those obtained with the model that only accounts for the spatial and temporal distribution of the laser source (model D). The attention has been directed towards the vertical displacements generated by line-focused laser illumination of an aluminum half-space both on the surface ($x_3 = 0$) and on the epicentral axis ($x_1 = 0$).

Figure 2.5 shows the computed waveforms for vertical displacements on the surface, where a positive displacement is in the positive x_3 direction, i.e. inwards. The waveforms exhibit a significantly different shape and amplitude depending on the distance from the axis of application of the laser line-source. The portion of the surface which is irradiated undergoes the most extreme variations in displacement.

Furthermore, when the point of observation is located well inside the heated region ($x_1 = 0.05$ mm in Fig. 2.5), the thermal phenomena taking place right under the source dominate the waveform. Consequently, the disagreement between the two predictions is significant, as the purely elastic dipole model (model D) is unable to capture the thermal mechanisms. However, even inside the heated region, the two models show better agreement as the distance to the axis of the line-source increases. The waveforms are undistinguishable for distances larger than $x_1 = 0.6 R_G$.

Experimental measurements of surface vertical displacements generated by a point laser source inside the heated region have been reported in the literature (Spicer and Hurley, 1996) and agree qualitatively with the theoretical waveform for $x_1 = 0.05$ mm, the shortest distance shown in Fig. 2.5. The fact that the experiment is conducted with an axially symmetric source instead of the infinitely long line considered in the calculations does not seem to have a significant effect in the comparison for very short distances relative to the size of the irradiated region.

The above described near-field, i.e. the field generated inside the heated region or very close to it, is of interest in many applications. In particular, one can study theoretically the interactions of the field generated by a scanning laser source with a surface-breaking crack as the source passes over the defect (Kromine et al., 2000a). In such a setup, an accurate description of the near-field is vital to quantitative modeling of experimental measurements. The above results show the need for the thermoelastic model.

In the far-field, i.e. well outside the irradiated region ($x_1 \geq 1.0$ mm in Fig. 2.5), the waveform is dominated by the Rayleigh surface wave which travels along the surface without geometrical attenuation. The attenuating longitudinal and shear waves

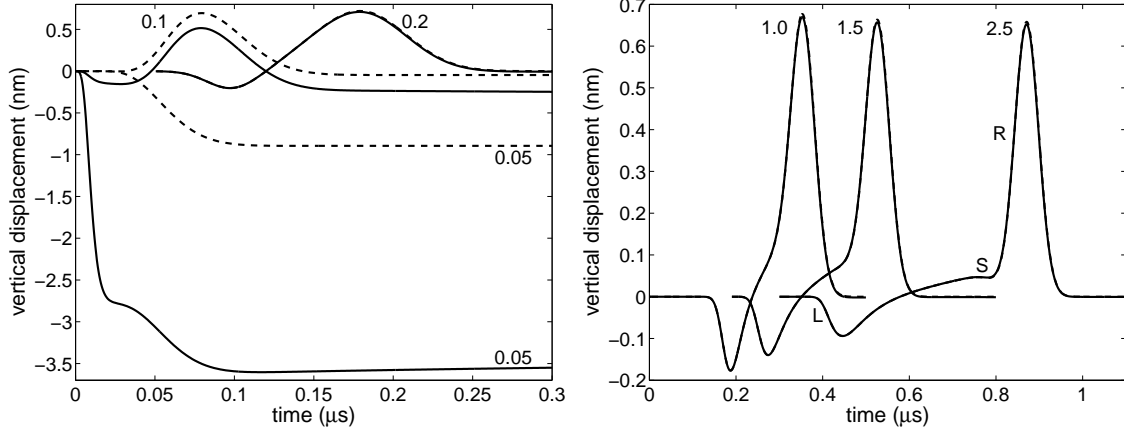


Figure 2.5: Vertical displacement on the surface calculated with model B (solid line) and model D (dashed line). The numbers next to the waveforms indicate the distance in mm from the axis of the laser line-source. The labels L, S and R denote longitudinal, shear and Rayleigh surface waves, respectively.

can also be identified in the waveforms for short enough distances. In this region, both models show perfect agreement, as can be expected since the thermal effects are not significant outside a relative small distance from the heated region. The Rayleigh pulse is a monopolar inward displacement, whose temporal profile reproduces that of the laser beam, in contrast with the bipolar Rayleigh pulse produced by a point-source.

Figure 2.6 shows the computed waveforms for vertical displacements on the epical axis. Again, a positive displacement is in the positive x_3 direction. The precursor, although small, can be clearly identified in the waveform computed with the thermoelastic model (model B). It is not predicted by the simplified model (model D). For the smaller depths, there is also a disagreement between the two waveform predictions after the arrival of the elastic waves, the signal predicted by the ther-

thermoelastic model being weaker. Furthermore, as a consequence of heat diffusion, the temperature field slowly tends to zero with time, and so does the displacement field obtained with model B as shown in Fig. 2.6 for $x_3 = 0.05$ mm. It is clear that, if thermal diffusion is neglected, the heat deposited in the material by the laser will not dissipate and, as follows from Eq. (2.8), the corresponding temperature field will not vanish as time approaches infinity, even if convolved with the finite laser pulse temporal profile. Thus, the displacement field obtained with model D exhibits a non-physical, non-zero solution for large times relative to the arrival times of the elastic waves as shown in Fig. 2.6 for $x_3 = 0.05$ mm. Differences between the waveforms predicted by the two models for the time scales of interest are noticeable for distances smaller than around seven times the width of the laser line-source. However, it takes a much larger distance for the disagreement in the precursor part of the waveform to disappear. It should be pointed out that, although the precursor appears to be small relative to the main part of the waveform, it has attracted considerable attention for its potential applications. As a relative sharp, distinct feature of the waveform, it has been used quite effectively for velocity and attenuation measurements. In addition, the precursor may be relevant for calibration purposes. In these applications, a model capable of an accurate prediction of the precursor is of interest.

Although the above results have been obtained for a half-space, one may conclude that in the case of laser generation in plates, the thickness of the plate relative to the size of the irradiated region will dictate the appropriateness of the use of the simplified model to predict the displacements at the epicenter. For thin plates, the thermoelastic model should be used to accurately determine the epicentral displace-

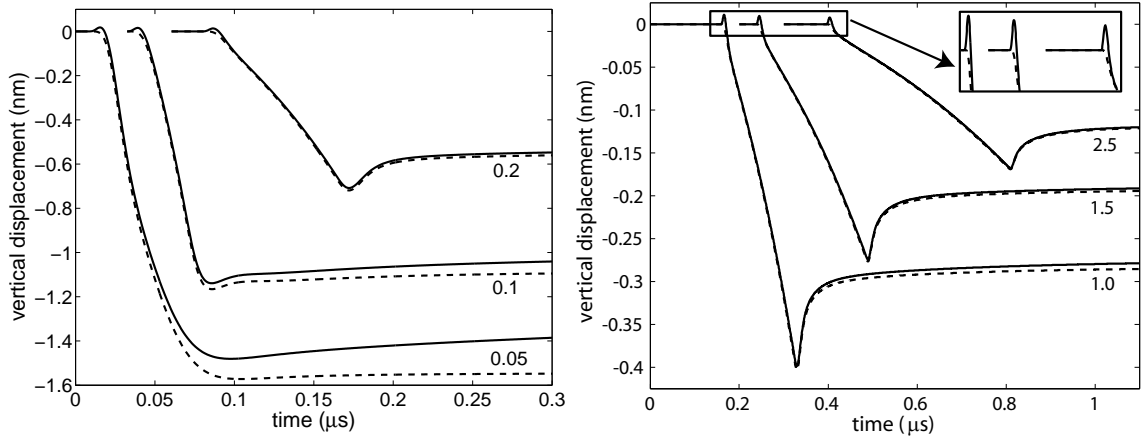


Figure 2.6: Vertical displacement on the epicentral axis calculated with model B (solid line) and model D (dashed line). The numbers next to the waveforms indicate the depth in mm.

ment.

2.6.3 The effect of the width of the line-source and the duration of the laser pulse

A parametric study has been carried out to investigate the influence of the width of the line-source (R_G) and the duration of the pulse (v) on the characteristics of the generated signal. Several waveforms for the vertical displacement at 1 mm depth on the epicentral axis have been calculated by varying the width of the line-source and the duration of the laser pulse independently and assuming a fixed value for the energy of the laser. The calculated time signals are shown in Fig. 2.7(a) for the case of increasing width for a fixed pulse duration ($v = 10$ ns) and Fig. 2.7(b) for the case of increasing pulse duration for a fixed width ($R_G = 0.5$ mm).

In both cases, as the dimensions of the pulse are increased in space and time, the

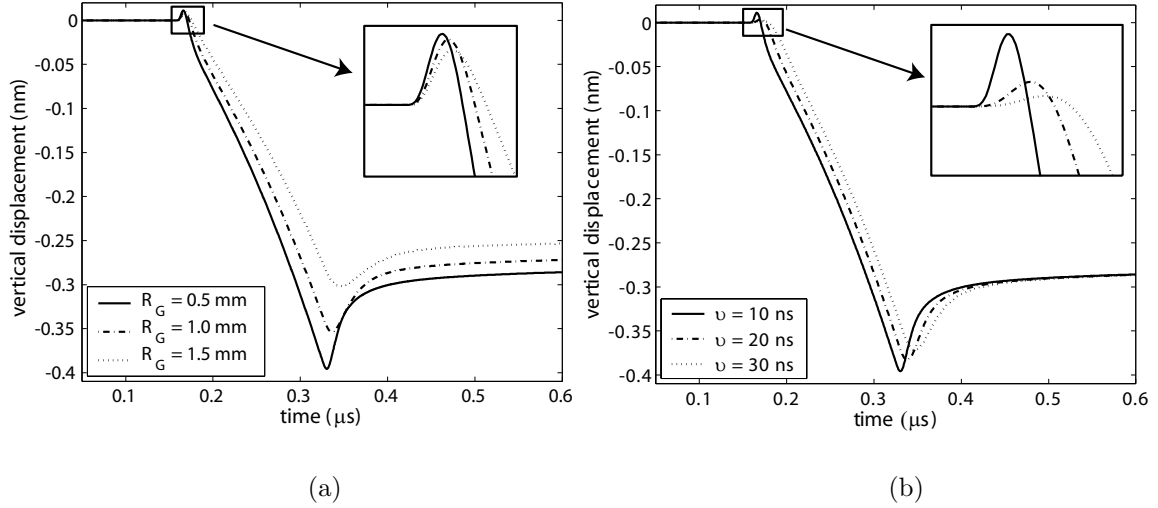


Figure 2.7: Influence of the width of the line-source (a) and the duration of the laser pulse (b) on the vertical displacement waveform at the epicentral axis.

signal becomes broader and its magnitude decreases. The width of the line-source has also an effect on the amplitude of the final part of the waveform as shown in Fig 2.7(a). In contrast, this amplitude appears not to be affected significantly by changes in the duration of the laser pulse according to Fig 2.7(b). In the same figure, a delay in the arrival of the signal can be noted as the energy deposition is spread in time. This effect may be explained by the shift in the position of the peak of the pulse as its duration (v) increases, according to Eq. 2.3. The same effects are even more noticeable in the shape of the precursor (see insets in Fig 2.7). Indeed, for larger or longer laser irradiation, the precursor appears smaller and broader. Its arrival is also delayed for longer pulse durations. These results agree with those reported in the literature for axially symmetric laser sources (McDonald, 1990).

2.6.4 Distribution of stresses

An understanding of the stress field generated by line-focused laser irradiation may be important for some applications. In particular, one may want to study the interactions of the laser generated field with surface breaking-cracks. For that purpose it is useful to introduce the concept of the scattered field, which is generated by tractions on the faces of the crack such that, when added to those produced by the incident field on the plane of the crack, the condition of traction free crack faces is met. Thus, in order to obtain the scattered field, one needs to know the stresses generated by the incident field, i.e. the field generated by the laser in the absence of the crack. Furthermore, if the laser source is swept across the test specimen as in the Scanning Laser Source technique, the stress field needs to be determined in detail both far and near the source (Arias and Achenbach, 2003a).

In this section we describe the stress field generated in an aluminum half-space by line-focused laser illumination. The theoretical results have been obtained with the thermoelastic model which accounts for thermal diffusion (model B), with $R_G = 0.45$ mm and $\nu = 10$ ns. We present snapshots of the spatial distribution of the stress components σ_{11} , σ_{33} and σ_{31} at different times (Fig. 2.8) and stress waveforms on the surface (Fig. 2.9) and on the epicentral axis (Figs. 2.10 and 2.11). In these figures, a positive normal stress indicates compression and a positive shear stress on the top face of an element points in the positive x_1 direction.

The stress field is governed by two phenomena that take place at two very different time scales and exhibit quite different characteristics. Over the duration of the pulse, the laser source deposits heat in a very thin region under the illuminated surface area. The depth of the energy deposition is determined by the thermal diffusion

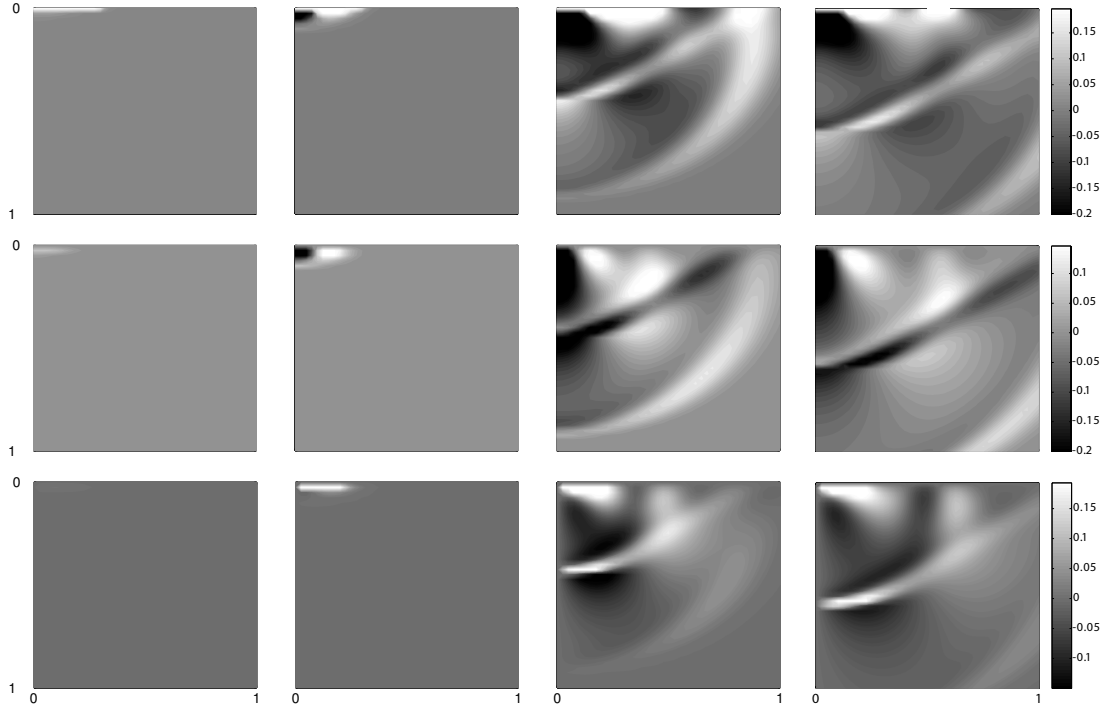


Figure 2.8: Snapshots of the stress components σ_{11} (top), σ_{33} (middle) and σ_{31} (bottom) due to the laser line-source at times 0.01 (left), 0.02 (center-left), 0.15 (center-right) and 0.2 μs (right), computed for $R_G = 0.45$ mm and $v = 10$ ns. The region shown corresponds to 1 mm in depth per 1 mm to the right of the epicentral axis. Positive normal stresses indicate compression.

length defined as $l_\kappa = \sqrt{4\kappa v}$. After the pulse, the diffusion of the heat into the bulk of the material takes place at a slow time scale. This phenomenon dominates the stress field in the region near the heat source and gives rise to smooth waveforms with relative high amplitude, such as those shown in Fig. 2.9 and in Figs. 2.10 and 2.11 for $x_1 \leq 0.2$ mm and $x_3 \leq 0.2$ mm, respectively. At larger distances from the heat source, the elastic wave propagation resulting from the rapid heat deposition becomes noticeable, as the thermal effects loose intensity. The propagation of elastic waves takes place at a much faster time scale and leads to sharper waveforms with smaller amplitudes as shown in Fig. 2.9 and Figs 2.10 and 2.11 for $x_1 \geq 0.5$ mm and $x_3 \geq 0.5$ mm, respectively.

The snapshots of the spatial stress distribution in the region defined by 1 mm in depth per 1 mm to the right of the epicentral axis at four different representative times shown in Fig. 2.8 provide further illustration for the above described effects. The first snapshots correspond to the instant when the peak of the laser pulse hits the surface ($t = 0.01 \mu\text{s}$). At this point, a thin portion of material under the illuminated spot is rapidly heated up. The surrounding material prevents the heated region from expanding laterally which results in a high localized σ_{11} compression of the heated material. The highest values of compression appear in the horizontal stress σ_{11} at the surface of the heated region. The corresponding waveforms are shown in Fig. 2.9 for $x_1 \leq 0.2$ mm. A smaller σ_{33} for compression appears beneath the heated material in the $t = 0.01 \mu\text{s}$ snapshot in Fig. 2.8. This compression can be identified as the precursor in the corresponding near-field ($x_1 \leq 0.2$ mm) waveforms on the epicentral axis shown in Fig. 2.11. A small shear stress appears also in this region, although it is not noticeable in the scale of the σ_{31} plots in Fig. 2.8.

A short time after the laser source stops acting on the surface ($t = 0.02 \mu\text{s}$ in Fig. 2.8), localized tensions and shear appear beneath the heated region. Intuitively, it is expected that the heated region expands over time both laterally and upwards towards the free surface. On the one hand, the fact that lateral expansion of the heated region is constrained by the surrounding material while the expansion upwards is free, as well as the temperature gradient, induces a slight bending of the thin heated portion of material. This creates a negative pressure under the heated region, thereby giving rise to both vertical and horizontal tensions. These tensions appear as dark spots in the σ_{11} and the σ_{33} stress maps in Fig. 2.8. A representative σ_{11} waveform for the region under tension is shown in Fig. 2.10 for $x_3 = 0.05 \text{ mm}$. The waveforms in Fig. 2.11 for $x_3 \leq 0.2 \text{ mm}$ show this effect for the σ_{33} stress component. On the other hand, the lateral expansion of the heated region shears the material under, which is not yet heated, thereby giving rise to the positive shear stress shown in Fig 2.8 for $t = 0.02 \mu\text{s}$.

At later times ($t = 0.15 \mu\text{s}$ and $t = 0.2 \mu\text{s}$ in Fig. 2.8), the elastic waves have travelled outside the near-field region, where the stress field is dominated by the quasi-static thermoelastic solution. Thus, the elastic wavefronts are noticeable in the plots and in the corresponding far-field waveforms (see Fig. 2.9 and Figs. 2.10 and 2.11 for $x_1 \geq 0.5 \text{ mm}$ and $x_3 \geq 0.5 \text{ mm}$, respectively). In the far-field waveforms for the normal stresses, σ_{11} and σ_{33} , on the epicentral axis (Figs. 2.10 and 2.11 for $x_3 \geq 0.5 \text{ mm}$), the precursor can be clearly identified as the sharp compressional spike at the arrival of the longitudinal wave. The longitudinal and the head wavefronts appear very clearly, especially in the snapshots of the normal stresses in Fig. 2.8. As expected, these two wavefronts meet in the surface as can be clearly seen in the

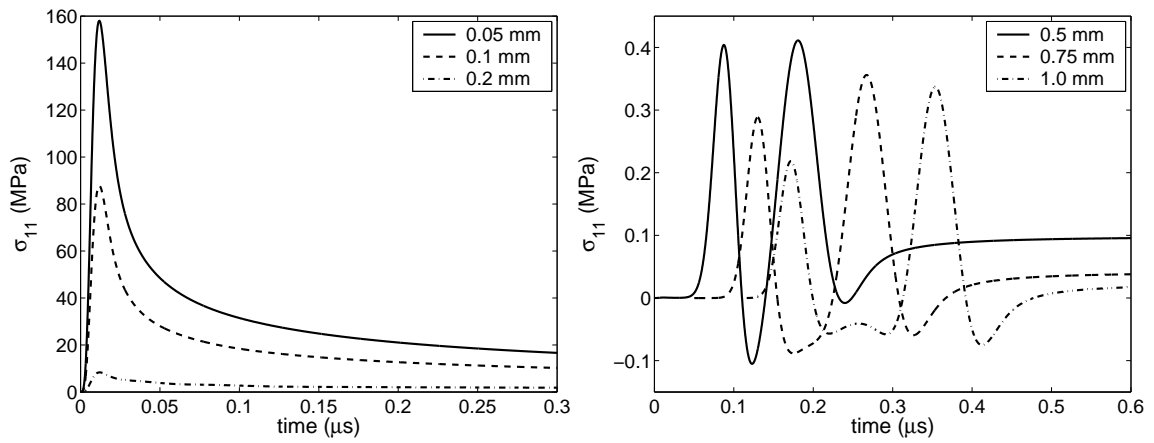


Figure 2.9: Stress component σ_{11} on the surface. The legend indicates the distance to the epicentral axis. A positive value indicates compression.

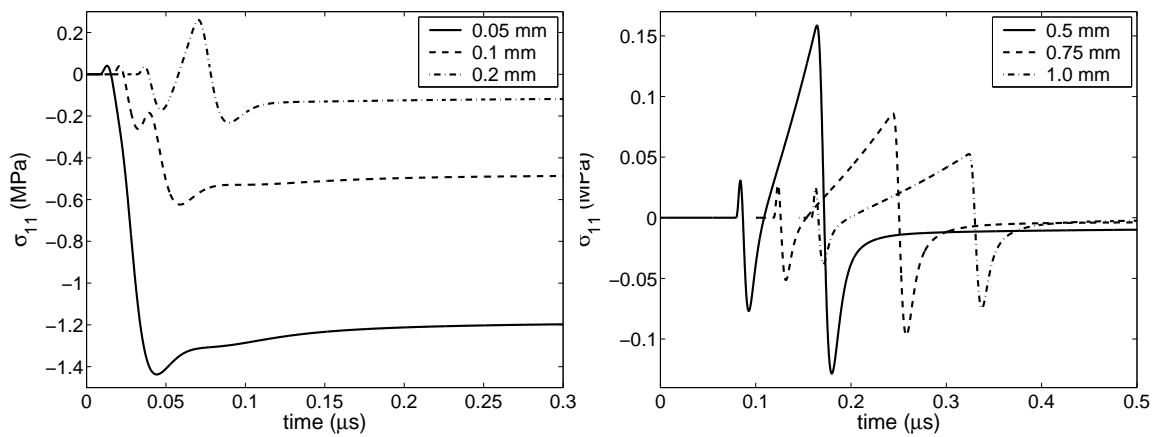


Figure 2.10: Stress component σ_{11} on the epicentral axis. The legend indicates the depth. A positive value indicates compression.

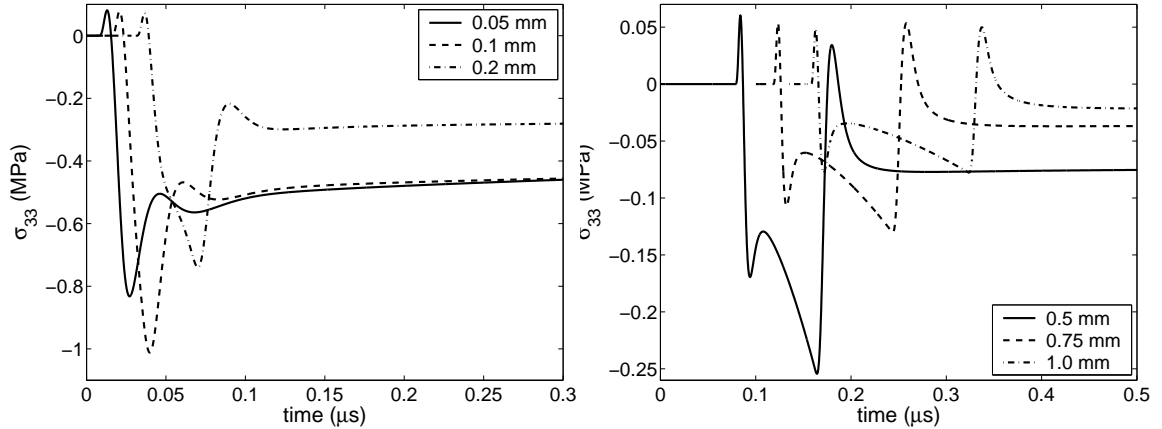


Figure 2.11: Stress component σ_{33} on the epicentral axis. The legend indicates the depth. A positive value indicates compression.

σ_{11} and σ_{33} snapshots for $t = 0.15 \mu\text{s}$. While the transverse wavefront is not as distinct in the snapshots of the normal stresses, it is quite visible in the shear stress snapshots. As expected, the head wavefront is tangent to the transverse wavefront. The Rayleigh wavefront can be identified in the σ_{11} snapshots in Fig. 2.8 especially for $t = 0.2 \mu\text{s}$ where it appears as a light spot on the surface distinct from the quasi-static compression. The far-field ($x_1 \geq 0.5 \text{ mm}$) σ_{11} waveforms on the surface in Fig. 2.9 show the Rayleigh wave as a monopolar compression pulse with two smaller tension pulses before and after. At much later times (not shown in Fig. 2.8), all the heat deposited in the solid eventually dissipates and the quasi-static field vanishes, since the laser pulse is of finite duration.

2.7 Conclusions

A two-dimensional theoretical model for the field generated in the thermoelastic regime by line-focused laser illumination of a homogeneous, isotropic, linearly elastic half-space has been presented. The model is obtained by solving the corresponding thermoelastic problem in plane strain, rather than by superposition of available three-dimensional solutions for the axially symmetric source, resulting in a smaller computational effort. The thermoelastic problem has been solved by Fourier–Laplace transform techniques. The solutions in the transformed domain have been presented in detail. The inversion of the transforms has been performed numerically to obtain theoretical waveforms.

The model takes account of the effects of thermal diffusion and optical penetration, as well as the spatial and temporal distribution of the source. Each of these effects can be easily neglected in the complete thermoelastic model by taking appropriate limits. By neglecting all of them, the well-known surface dipole model is recovered. Based on simple elasticity considerations, the strength of the dipole has been related to the heat input and certain material properties. The expression differs from that available in the literature by a factor related to the presence of the free surface.

Theoretical waveforms for normal surface displacements due to the Rayleigh wave have been compared with experimental measurements available in the literature and excellent quantitative agreement has been found. This result shows that the proposed thermoelastic model provides a quantitative basis for generation of ultrasound by line-focused laser illumination.

The effect of thermal diffusion has been investigated in vertical displacement

waveforms on the epicentral axis and on the surface of an aluminum half-space. As expected, this effect is significant near the heated region, while it is not noticeable in the far-field. If thermal diffusion is neglected in the model, the results have been estimated to be accurate only for distances several times larger than the width of the laser line-source on the epicentral axis and around 60% of the width of the laser line-source on the surface. The thermoelastic model predicts the precursor spike on the waveforms on the epicentral axis, which results from the subsurface sources arising in metals mainly due to thermal diffusion. A parametric study of the effects of the width of the laser line-source and the duration of the pulse has shown that the generated signal becomes broader and its magnitude decreases as the laser line-source is spread out in space and time. Finally, we have presented stress waveforms on the epicentral axis and at the surface, and snapshots of the stress distribution. These results provide illustration of the different effects under line-focused laser illumination, which have been explained by intuitive arguments.

Chapter 3

Rayleigh wave correction for the BEM analysis of two-dimensional elastodynamic problems in a half-space

A simple, elegant approach is proposed to correct the error introduced by the truncation of the infinite boundary in the BEM modeling of two-dimensional wave propagation problems in elastic half-spaces. The proposed method exploits the knowledge of the far-field asymptotic behavior of the solution to adequately correct the BEM displacement system matrix for the truncated problem to account for the contribution of the omitted part of the boundary. The reciprocal theorem of elastodynamics is used for a convenient computation of this contribution involving the same boundary integrals that form the original BEM system. The method is formulated for a two-dimensional homogeneous, isotropic, linearly elastic half-space and its implementation in a frequency domain boundary element scheme is discussed in some detail. The formulation is then validated for a free Rayleigh pulse travelling on a half-space and successfully tested for a benchmark problem with a known approxi-

mation to the analytical solution.

3.1 Introduction

The boundary element method (BEM) is ideally suited for the numerical analysis of problems of wave propagation in elastic media that are unbounded outside a bounded domain with boundary S , since only the boundary S needs to be discretized and the radiation conditions at infinity are naturally accounted for in the formulation. However, when the elastic medium is modeled as a half-space, with possibly some geometric features such as cracks, voids and inclusions, not only the domain but also its boundary are unbounded. In elastodynamics, the BEM formulation for a half-space is usually stated in terms of full-space – rather than half-space – Green’s functions, and thus the discretization over the boundary of the half-space is needed in order to enforce the appropriate boundary conditions. Obviously, the infinite extent of the boundary requires a special treatment in any numerical scheme.

The most straightforward approach consists in restricting the discretization to a finite part of the boundary, thereby truncating the boundary integrals. In three dimensional elastodynamics, this approach can lead to accurate solutions near the source region, as long as the computational mesh is extended far enough, since the waves propagating along the boundary, i.e. longitudinal, transverse, and Rayleigh waves, exhibit geometrical attenuation in the direction of propagation. Thus, the contribution to the integrals from regions far away from the zone of interest is negligible. However, in a two-dimensional geometry, Rayleigh surface waves propagate along the boundary without attenuation, and therefore the above approach will

produce inaccurate results due to spurious reflections from the ends of the computational mesh. This difficulty has been traditionally overcome by adding a small amount of damping to the material, which results in attenuation of all types of waves. This approach provides accurate solutions when the truncation points are at sufficient distances from the region of interest Domínguez (1993), which leads to an inefficient use of the computational resources.

A more efficient and sophisticated treatment of the infinite boundary is provided by the infinite boundary element technique first proposed by Watson (1979) and later presented in more detailed form in Beer and Watson (1989). This technique maps the omitted part of the boundary, which extends to infinity, into a finite region. The behavior of the displacements and the tractions in the infinite region is modelled through decay functions suitable for each particular problem. Zhang et al. (1991) developed decay shape functions to describe three-dimensional far-field wave propagation based on the asymptotic behavior of Stokes' solutions. Bu (1997) proposed an oscillatory shape function derived from three-dimensional Rayleigh wave propagation in the far-field. In all cases, the resulting integrals over the infinite element require special numerical integration schemes and are quite involved particularly for the case of oscillatory kernels.

In this Chapter, we present a simple, elegant approach to the treatment of infinite boundaries for time-harmonic problems. The formulation is detailed for a two-dimensional, homogeneous, isotropic, linearly elastic half-space in which the main objective is to allow the undamped Rayleigh waves to propagate to infinity. The proposed method consists of two parts.

First, common to other techniques, the knowledge of the general form of the

asymptotic far-field solution is exploited. For instance, in Domínguez and Meise (1991), when dealing with waves propagating in channels, a fictitious boundary is introduced to close the unbounded domain and the knowledge of the far field standing wave solutions is used to derive appropriate Robin boundary conditions. The derivation of this type of absorbing boundary conditions is not obvious in many applications. In the present Chapter, it is assumed that the numerical solution takes the known far-field general form of Rayleigh waves in the omitted part of the boundary, in principle, of unknown amplitude and phase. This assumption is used here to rewrite the integrals that represent the contribution of the omitted part or the boundary as the product of integrals of known quantities on the omitted part of the boundary and the unknown amplitudes and phases of the far-field Rayleigh waves. In order to eliminate these unknowns, the assumed far-field Rayleigh waves are matched to the nodal values at the end nodes of the computational boundary. Consequently, the coefficients of the original BEM displacement system matrix associated with the end nodes are modified.

Next, the integrals on the infinite omitted part of the boundary are computed. These integrals may be approximated numerically, as has been done in some applications of the infinite boundary element method (Bu, 1997). Also, in Heymsfield (1997a) and Heymsfield (1997b), which address the problem of soil amplification of seismic waves, the contribution of the completely known far field solution (given as data in these papers) are integrated numerically over the infinite part of the boundary. By contrast, in the present Chapter the reciprocity theorem of elastodynamics is invoked to derive a boundary integral representation for the known general form of the far-field solution, i.e. the unit amplitude Rayleigh wave, with the same

fundamental solution of the original formulation (Li and Achenbach, 1991). This representation involves the same integrals over the omitted part of the boundary that are needed to modify the original BEM system, integrals of known quantities on the originally discretized part of the boundary, and in some cases integrals on additional boundaries whose computational cost is very small. This simple approach provides a convenient way of computing the integrals over the omitted part of the boundary in terms of integrals on finite boundaries. Furthermore, it allows for a very efficient numerical implementation in terms of the same basic element integrals of the original BEM scheme. Consequently, the proposed technique comes at a very low, in many cases essentially negligible, additional cost as compared to the simple truncation of the boundary.

It should be noted that for the present method to be accurate, the discretized boundary needs to be extended far enough for the body waves to have substantially attenuated and thus, for the assumption that the Rayleigh waves dominate the solution in the omitted part of the boundary to hold. In return, no spurious reflections are produced, and the accuracy of the solution is not degraded near the ends of the mesh.

The method is developed in detail for Rayleigh waves in two-dimensional elastodynamics, but the basic ideas are applicable to a broader range of wave propagation problems. The best suited problems are those in which the far-field solution does not decay, such as Stoneley waves in material interfaces, or propagating Lamb modes in layers. However, it can also be useful for cases of decaying far-field solutions, such as occur in two-dimensional viscoelasticity. In this case, although the Rayleigh waves attenuate, they do so slower than the body waves, and consequently the present

technique can reduce the extent of the computational mesh.

In the following sections, the above described techniques are first formulated and their implementation in a frequency domain boundary element scheme is discussed. Then, the proposed method is validated for a free Rayleigh wave travelling on a half-space and tested for a benchmark problem with a known asymptotic approximation to the analytical solution.

3.2 Formulation

3.2.1 Reciprocity theorem in time-harmonic elastodynamics

The dynamic reciprocity theorem relates two elastodynamic states of the same bounded or unbounded body (Wheeler and Sternberg, 1968). These states are defined by sets of displacements and stresses which are the solution to two elastodynamic boundary value problems for the same body but with possibly different distributions of body forces, different initial conditions and different boundary conditions. For time-harmonic two-dimensional elastodynamics it can be stated as follows. Let Ω be an elastic region with boundary Γ and closure $\bar{\Omega}$. Consider two time-harmonic elastodynamic states of the same angular frequency ω on $\bar{\Omega}$ denoted with superscripts A and B , respectively. Then,

$$\begin{aligned} & \int_{\Omega} [f_{\alpha}^A(\mathbf{x}, \omega) u_{\alpha}^B(\mathbf{x}, \omega) - f_{\alpha}^B(\mathbf{x}, \omega) u_{\alpha}^A(\mathbf{x}, \omega)] d\Omega(\mathbf{x}) \\ &= \int_{\Gamma} [\sigma_{\beta\alpha}^B(\mathbf{x}, \omega) u_{\alpha}^A(\mathbf{x}, \omega) - \sigma_{\beta\alpha}^A(\mathbf{x}, \omega) u_{\alpha}^B(\mathbf{x}, \omega)] n_{\beta}(\mathbf{x}) d\Gamma(\mathbf{x}), \end{aligned} \quad (3.1)$$

where $f_\alpha^{A,B}$, $u_\alpha^{A,B}$, $\sigma_{\beta\alpha}^{A,B}$ represent body forces, displacements and stresses, respectively, and \mathbf{n} is the unit vector along the outward normal to Γ .

In the formulation of the boundary element method, Eq. (3.1) is invoked to derive an integral representation for the displacement solution of the problem to be solved (state A) at a point $\boldsymbol{\xi} \in \Omega$ by choosing the time-harmonic fundamental solution, i.e. the solution to a time-harmonic unit point load applied at $\boldsymbol{\xi}$, as elastodynamic state B . Then, a limiting process is followed to derive a boundary integral equation for points located on the boundary, i.e. $\boldsymbol{\xi} \in \Gamma$ (Domínguez, 1993). In this Chapter, the reciprocity theorem is invoked a second time to obtain an integral representation for the contribution of the omitted part of the boundary as described in section 3.2.4.

3.2.2 Asymptotic behavior of the displacement far-field solution

Let us consider a two-dimensional elastodynamic problem defined on a homogeneous, isotropic, linearly elastic half-space with boundary Γ . The corresponding frequency domain boundary integral equation for a point $\boldsymbol{\xi} \in \Gamma$ in the absence of body forces may be obtained from Eq. (3.1) as

$$c_{\alpha\beta}(\boldsymbol{\xi}) \bar{u}_\beta(\boldsymbol{\xi}, \omega) = \int_\Gamma [\bar{u}_{\alpha\beta}^*(\boldsymbol{\xi}, \mathbf{x}, \omega) \bar{t}_\beta(\mathbf{x}, \omega) - \bar{t}_{\alpha\beta}^*(\boldsymbol{\xi}, \mathbf{x}, \omega) \bar{u}_\beta(\mathbf{x}, \omega)] d\Gamma(\mathbf{x}), \quad (3.2)$$

$$\alpha, \beta = 1, 2,$$

where $\bar{u}_{\alpha\beta}^*$ and $\bar{t}_{\alpha\beta}^*$ are the full-space frequency domain elastodynamic fundamental solution displacement and traction tensors respectively (Domínguez, 1993). Note that $\bar{u}_{\alpha\beta}^*(\boldsymbol{\xi}, \mathbf{x}, \omega)$ and $\bar{t}_{\alpha\beta}^*(\boldsymbol{\xi}, \mathbf{x}, \omega)$ represent the “ β ” component of the displacement

and the traction on the boundary, respectively, at the point \mathbf{x} due to a unit time-harmonic load of angular frequency ω applied at the point $\boldsymbol{\xi}$ in the direction “ α ”. Also, $\bar{u}_\beta, \bar{t}_\beta$ are frequency domain displacements and tractions on the boundary, ω stands for the angular frequency and $c_{\alpha\beta}$ is called the jump coefficient given by:

$$c_{\alpha\beta}(\boldsymbol{\xi}) = \begin{cases} \frac{1}{2}\delta_{\alpha\beta}, & \text{if } \Gamma \text{ is smooth at point } \boldsymbol{\xi}, \\ c_{\alpha\beta}, & \text{if } \Gamma \text{ has a corner at point } \boldsymbol{\xi}, \end{cases} \quad (3.3)$$

where $\delta_{\alpha\beta}$ represents the Kronecker delta. The jump coefficient for corner points can be derived by an indirect approach as described in Domínguez (1993). The integrals in Eq. (3.2) are interpreted in the sense of the Cauchy Principal Value.

Let us assume that outside a localized region, Γ_1 , where the boundary may be irregular and submitted to various types of boundary conditions, the boundary is a straight surface free of tractions. Let Γ_0 be the part of this traction-free boundary which will be included in the discretization and Γ_∞ the remaining infinite part which will be omitted (see Fig. 3.1). In this case, Eq. (3.2) becomes

$$c_{\alpha\beta}(\boldsymbol{\xi}) \bar{u}_\beta(\boldsymbol{\xi}, \omega) + \int_{\Gamma_\infty} \bar{t}_{\alpha\beta}^*(\boldsymbol{\xi}, \mathbf{x}, \omega) \bar{u}_\beta(\mathbf{x}, \omega) d\Gamma(\mathbf{x}) + \int_{\Gamma_0 \cup \Gamma_1} \bar{t}_{\alpha\beta}^*(\boldsymbol{\xi}, \mathbf{x}, \omega) \bar{u}_\beta(\mathbf{x}, \omega) d\Gamma(\mathbf{x}) = \int_{\Gamma_1} \bar{u}_{\alpha\beta}^*(\boldsymbol{\xi}, \mathbf{x}, \omega) \bar{t}_\beta(\mathbf{x}, \omega) d\Gamma(\mathbf{x}). \quad (3.4)$$

The three characteristic waves along the traction-free boundary, namely the longitudinal, transverse, and Rayleigh waves, all contribute to the displacement field. However, it is well known that body waves exhibit geometrical decay in the propagating direction, whereas Rayleigh waves in two dimensions do not. Therefore, the

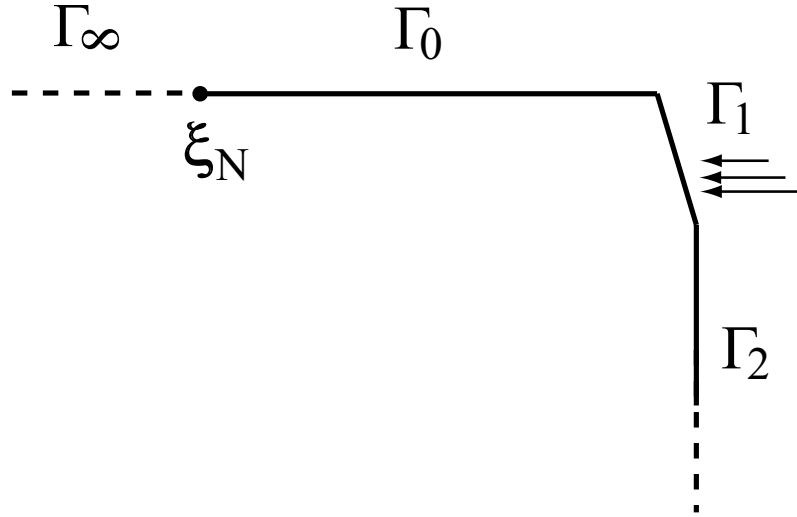


Figure 3.1: Schematic definition of the computational domain. $\Gamma^\pm = \Gamma_\infty^\pm \cup \Gamma_0^\pm \cup \Gamma_1^\pm$

displacement far-field solution can be approximated by the Rayleigh surface wave part of the solution, thereby neglecting the contribution of the body waves. Hence, if the truncation points ξ_1 and ξ_N are located far enough from the source region, then we can write for each side of the infinite boundary (Γ_∞^\pm)

$$\begin{aligned} \xi \in \Gamma_\infty^- : \bar{u}_\alpha(\xi, \omega) &\approx R^-(\omega) \bar{u}_\alpha^{SR}(\xi, \omega), \\ \xi \in \Gamma_\infty^+ : \bar{u}_\alpha(\xi, \omega) &\approx R^+(\omega) \bar{u}_\alpha^{SR}(\xi, \omega), \end{aligned} \tag{3.5}$$

where R^- and R^+ are the unknown complex amplitudes of the far-field Rayleigh waves at each side of the boundary and \bar{u}_α^{SR} represents the frequency domain displacements corresponding to unit amplitude time-harmonic Rayleigh surface waves of angular frequency ω propagating along the surface of the half-space in the positive direction. Note that the fact that the far field solution in the boundary extending to

$-\infty$ propagates in the negative direction will be taken into account in the complex coefficient R^- . The expressions for \bar{u}_α^{SR} can be found, for instance, in Achenbach (1973).

Hence, Eq. (3.2) can be rewritten as:

$$\begin{aligned}
R^-(\omega) \int_{\Gamma_\infty^-} \bar{t}_{\alpha\beta}^*(\boldsymbol{\xi}, \mathbf{x}, \omega) \bar{u}_\beta^{SR}(\mathbf{x}, \omega) d\Gamma(\mathbf{x}) + R^+(\omega) \int_{\Gamma_\infty^+} \bar{t}_{\alpha\beta}^*(\boldsymbol{\xi}, \mathbf{x}, \omega) \bar{u}_\beta^{SR}(\mathbf{x}, \omega) d\Gamma(\mathbf{x}) \\
+ c_{\alpha\beta}(\boldsymbol{\xi}) \bar{u}_\beta(\boldsymbol{\xi}, \omega) + \int_{\Gamma_0 \cup \Gamma_1} \bar{t}_{\alpha\beta}^*(\boldsymbol{\xi}, \mathbf{x}, \omega) \bar{u}_\beta(\mathbf{x}, \omega) d\Gamma(\mathbf{x}) \\
= \int_{\Gamma_1} \bar{u}_{\alpha\beta}^*(\boldsymbol{\xi}, \mathbf{x}, \omega) \bar{t}_\beta(\mathbf{x}, \omega) d\Gamma(\mathbf{x}).
\end{aligned} \tag{3.6}$$

Note that in Eq. (3.6) the complex amplitudes R^- and R^+ are unknown, but the integrands over the infinite boundaries Γ_∞^- and Γ_∞^+ are known. Therefore, these integrals might be approximated numerically. Here, however, we propose a more elegant approach based on the reciprocity theorem of elastodynamics. This approach is described in detail in section 3.2.4.

3.2.3 Matching with the far-field solution at the ends of the computational boundary

By the use of Eq. (3.5) the solution is described asymptotically as a Rayleigh wave of unknown amplitude and phase. In order to eliminate the unknowns R^- and R^+ in Eq. (3.6), the solution in the computational domain is matched to the far-field

solution at the end points, i.e. $\boldsymbol{\xi}_1$ and $\boldsymbol{\xi}_N$. Hence, Eq. (3.5) yields, in particular:

$$R^-(\omega) \approx \frac{u_\alpha(\boldsymbol{\xi}_1, \omega)}{u_\alpha^{SR}(\boldsymbol{\xi}_1, \omega)}, \quad R^+(\omega) \approx \frac{u_\alpha(\boldsymbol{\xi}_N, \omega)}{u_\alpha^{SR}(\boldsymbol{\xi}_N, \omega)}, \quad \alpha = 1, 2. \quad (3.7)$$

From Eq. (3.6) we can define:

$$A_\alpha^+(\boldsymbol{\xi}, \omega) = \frac{1}{\bar{u}_\alpha^{SR}(\boldsymbol{\xi}_N, \omega)} \int_{\Gamma_\infty^+} \bar{t}_{\alpha\beta}^*(\boldsymbol{\xi}, \mathbf{x}, \omega) \bar{u}_\beta^{SR}(\mathbf{x}, \omega) d\Gamma(\mathbf{x}), \quad \alpha = 1, 2. \quad (3.8)$$

Similarly, we can define $A_\alpha^-(\boldsymbol{\xi}, \omega)$ using $\boldsymbol{\xi}_1$ and Γ_∞^- instead of $\boldsymbol{\xi}_N$ and Γ_∞^+ . With these definitions, Eq. (3.6) can be rewritten as:

$$\begin{aligned} & c_{\alpha\beta}(\boldsymbol{\xi}) \bar{u}_\beta(\boldsymbol{\xi}, \omega) + A_\alpha^-(\boldsymbol{\xi}, \omega) \bar{u}_\alpha(\boldsymbol{\xi}_1, \omega) + A_\alpha^+(\boldsymbol{\xi}, \omega) \bar{u}_\alpha(\boldsymbol{\xi}_N, \omega) \\ & + \int_{\Gamma_0 \cup \Gamma_1} \bar{t}_{\alpha\beta}^*(\boldsymbol{\xi}, \mathbf{x}, \omega) \bar{u}_\beta(\mathbf{x}, \omega) d\Gamma(\mathbf{x}) = \int_{\Gamma_1} \bar{u}_{\alpha\beta}^*(\boldsymbol{\xi}, \mathbf{x}, \omega) \bar{t}_\beta(\mathbf{x}, \omega) d\Gamma(\mathbf{x}), \quad \alpha = 1, 2. \end{aligned} \quad (3.9)$$

It is convenient to cast Eq. (3.9) in matrix form as follows:

$$\begin{aligned} & \mathbf{A}^-(\boldsymbol{\xi}, \omega) \bar{\mathbf{u}}(\boldsymbol{\xi}_1, \omega) + \mathbf{A}^+(\boldsymbol{\xi}, \omega) \bar{\mathbf{u}}(\boldsymbol{\xi}_N, \omega) \\ & + \mathbf{c}(\boldsymbol{\xi}) \bar{\mathbf{u}}(\boldsymbol{\xi}, \omega) + \int_{\Gamma_0 \cup \Gamma_1} \bar{\mathbf{t}}^*(\boldsymbol{\xi}, \mathbf{x}, \omega) \bar{\mathbf{u}}(\mathbf{x}, \omega) d\Gamma(\mathbf{x}) = \int_{\Gamma_1} \bar{\mathbf{u}}^*(\boldsymbol{\xi}, \mathbf{x}, \omega) \bar{\mathbf{t}}(\mathbf{x}, \omega) d\Gamma(\mathbf{x}), \end{aligned} \quad (3.10)$$

where:

$$\mathbf{A}^\pm(\boldsymbol{\xi}, \omega) = \begin{bmatrix} A_1^\pm(\boldsymbol{\xi}, \omega) & 0 \\ 0 & A_2^\pm(\boldsymbol{\xi}, \omega) \end{bmatrix}. \quad (3.11)$$

It should be noted that the second line of Eq. (3.10) corresponds to the standard terms of the simply truncated boundary integral equation. The two terms of the first line represent the correction which accounts for the contribution of the omitted part of the boundary of the half-space on which a Rayleigh surface wave is assumed to be predominant.

3.2.4 Integral over the omitted part of the infinite boundary

Let us consider a time-harmonic Rayleigh surface wave of angular frequency ω and unit amplitude propagating along the free surface of the half-space in the positive direction. In order to be able to determine the integrals over Γ_∞^- and Γ_∞^+ independently, a multidomain approach is needed in general. Let Γ_2 be a fictitious boundary which divides the half-space into two quarter-spaces and Γ^\pm the parts of the boundary Γ contained in each quarter-space, respectively. Let us now choose the time-harmonic Rayleigh surface wave as elastodynamic state A and the time-harmonic full-space fundamental solution of the same frequency ω as elastodynamic state B . By virtue of the reciprocity theorem of elastodynamics stated in Eq (3.1), and after the limiting process of taking the relation to the boundary, an integral representation may be derived for each quarter-space. For instance, for the quarter-space on the positive side of the horizontal axis, i.e. $\boldsymbol{\xi} \in \Gamma^+$ the integral representation is given as:

$$c_{\alpha\beta}(\boldsymbol{\xi}) \bar{u}_\beta^{SR}(\boldsymbol{\xi}, \omega) = \int_{\Gamma_2 \cup \Gamma^+} [\bar{u}_{\alpha\beta}^*(\boldsymbol{\xi}, \mathbf{x}, \omega) \bar{t}_\beta^{SR}(\mathbf{x}, \omega) - \bar{t}_{\alpha\beta}^*(\boldsymbol{\xi}, \mathbf{x}, \omega) \bar{u}_\beta^{SR}(\mathbf{x}, \omega)] d\Gamma(\mathbf{x}). \quad (3.12)$$

Invoking the zero traction boundary conditions along Γ_0^+ and Γ_∞^+ , Eq. (3.12) becomes:

$$\begin{aligned} & \int_{\Gamma_\infty^+} \bar{t}_{\alpha\beta}^*(\boldsymbol{\xi}, \mathbf{x}, \omega) \bar{u}_\beta^{SR}(\mathbf{x}, \omega) d\Gamma(\mathbf{x}) = -c_{\alpha\beta}(\boldsymbol{\xi}) \bar{u}_\beta^{SR}(\boldsymbol{\xi}, \omega) \\ & - \int_{\Gamma_0^+ \cup \Gamma_1^+ \cup \Gamma_2} \bar{t}_{\alpha\beta}^*(\boldsymbol{\xi}, \mathbf{x}, \omega) \bar{u}_\beta^{SR}(\mathbf{x}, \omega) d\Gamma(\mathbf{x}) + \int_{\Gamma_1^+ \cup \Gamma_2} \bar{u}_{\alpha\beta}^*(\boldsymbol{\xi}, \mathbf{x}, \omega) \bar{t}_\beta^{SR}(\mathbf{x}, \omega) d\Gamma(\mathbf{x}). \end{aligned} \quad (3.13)$$

Thus, Eq. (3.8) yields:

$$\begin{aligned} \bar{u}_\alpha^{SR}(\boldsymbol{\xi}_N, \omega) A_\alpha^+(\boldsymbol{\xi}, \omega) &= -c_{\alpha\beta}(\boldsymbol{\xi}) \bar{u}_\beta^{SR}(\boldsymbol{\xi}, \omega) - \int_{\Gamma_0^+ \cup \Gamma_1^+ \cup \Gamma_2} \bar{t}_{\alpha\beta}^*(\boldsymbol{\xi}, \mathbf{x}, \omega) \bar{u}_\beta^{SR}(\mathbf{x}, \omega) d\Gamma(\mathbf{x}) \\ &+ \int_{\Gamma_1^+ \cup \Gamma_2} \bar{u}_{\alpha\beta}^*(\boldsymbol{\xi}, \mathbf{x}, \omega) \bar{t}_\beta^{SR}(\mathbf{x}, \omega) d\Gamma(\mathbf{x}), \quad \alpha = 1, 2. \end{aligned} \quad (3.14)$$

An analogous equation can be derived for A_α^- , by considering the boundaries of the quarter-space on the negative side of the horizontal axis, i.e. Γ_0^- , Γ_1^- and Γ_2 .

Note that the fictitious boundary Γ_2 is, in principle, infinite. However, since the integrand decays rapidly away from the surface of the half-space, the integration can be truncated at a relatively short distance from the surface without loss of accuracy. In fact, it is well known that Rayleigh surface waves penetrate into a material up to a distance of about one wavelength. This can serve as a guiding criterion of the required length of integration.

Note also that if a quarter-space is analyzed, for instance invoking the symmetry of the problem under consideration, the boundary Γ_2 is already present in the formulation as part of Γ_1^+ or Γ_1^- . Obviously, in this case only one of the correction

terms in Eq. (3.10) is necessary.

The key in the present approach is that, by virtue of reciprocity, the integrals extending to infinity in Eq. (3.10), which are implicit in \mathbf{A}^- and \mathbf{A}^+ through Eq. (3.11), and Eq. (3.8) and its analogous for A_α^- , can be computed by the use of Eq. (3.14) and its analogous for A_α^- in terms of integrals over the bounded boundaries of the problem and possibly an additional boundary which can be truncated without loss of accuracy. This provides a simple way of calculating the correction to account for the omitted part of the boundary represented by the first two terms in Eq. (3.10).

3.3 Numerical implementation

According to Eq. (3.10), the computational boundary that needs to be discretized is $\Gamma_0 \cup \Gamma_1$. In addition, in order to obtain the correction coefficients $A_\alpha^\pm(\boldsymbol{\xi}, \omega)$ two integrations along the fictitious boundary Γ_2 need to be performed.

The BEM system of equations is formed in the usual. After the discretization of the domain and the interpolation of the displacements and tractions, the discretized BIE may be written for each node $\boldsymbol{\xi}_j$, N being the total number of nodes, as:

$$\begin{aligned} & \mathbf{c}_j \bar{\mathbf{u}}_j(\omega) + \mathbf{A}_j^-(\omega) \bar{\mathbf{u}}_1(\omega) + \mathbf{A}_j^+(\omega) \bar{\mathbf{u}}_N(\omega) \\ & + \sum_{e \in B_0 \cup B_1} \sum_{k=1}^{N_e} \left\{ \int_{\Gamma_e} \bar{\mathbf{t}}^*(\boldsymbol{\xi}_j, \eta, \omega) \boldsymbol{\phi}_k(\eta) d\Gamma(\eta) \right\} \bar{\mathbf{u}}_k(\omega) \\ & = \sum_{e \in B_1} \sum_{k=1}^{N_e} \left\{ \int_{\Gamma_e} \bar{\mathbf{u}}^*(\boldsymbol{\xi}_j, \eta, \omega) \boldsymbol{\phi}_k(\eta) d\Gamma(\eta) \right\} \bar{\mathbf{t}}_k(\omega), \quad j = 1, N, \end{aligned} \quad (3.15)$$

where $\mathbf{c}_j = \mathbf{c}(\boldsymbol{\xi}_j)$ and $\mathbf{A}_j(\omega) = \mathbf{A}(\boldsymbol{\xi}_j, \omega)$ and, similarly, $\bar{\mathbf{u}}_j$ and $\bar{\mathbf{t}}_j$ are displacements

and tractions at node $\boldsymbol{\xi}_j$, respectively. Here, B_i is the set of elements corresponding to Γ_i , N_e is the number of nodes per element, $\boldsymbol{\phi}_k$ are 2 x 2 diagonal matrices containing the corresponding shape functions ϕ_k , and $\eta \in [-1, 1]$ represents the intrinsic coordinate of the parent element.

Following the notation in Domínguez (1993), we can define:

$$\hat{\mathbf{H}}_{jk}^e(\omega) = \int_{\Gamma_e} \bar{\mathbf{t}}^*(\boldsymbol{\xi}_j, \eta, \omega) \boldsymbol{\phi}_k(\eta) d\Gamma(\eta), \quad (3.16)$$

$$\mathbf{G}_{jk}^e(\omega) = \int_{\Gamma_e} \bar{\mathbf{u}}^*(\boldsymbol{\xi}_j, \eta, \omega) \boldsymbol{\phi}_k(\eta) d\Gamma(\eta), \quad (3.17)$$

which are 2 x 2 matrices that relate the collocation point $\boldsymbol{\xi}_j$ with the node k of element e . Then, Eq. (3.15) can be rewritten as:

$$\begin{aligned} & \mathbf{c}_j \bar{\mathbf{u}}_j(\omega) + \mathbf{A}_j^-(\omega) \bar{\mathbf{u}}_1(\omega) + \mathbf{A}_j^+(\omega) \bar{\mathbf{u}}_N(\omega) \\ & + \sum_{e \in B_0 \cup B_1} \sum_{k=1}^{N_e} \hat{\mathbf{H}}_{jk}^e(\omega) \bar{\mathbf{u}}_k(\omega) = \sum_{e \in B_1} \sum_{k=1}^{N_e} \mathbf{G}_{jk}^e(\omega) \bar{\mathbf{t}}_k(\omega), \quad j = 1, N. \end{aligned} \quad (3.18)$$

The above equation can be written in a more compact manner by defining:

$$\mathbf{H}_{jk}^e(\omega) = \begin{cases} \hat{\mathbf{H}}_{jk}^e(\omega) & \text{if } j \neq k, \\ \hat{\mathbf{H}}_{jk}^e(\omega) + \mathbf{c}_j & \text{if } j = k. \end{cases} \quad (3.19)$$

Then, assembling the matrices \mathbf{H}_{jk}^e and \mathbf{G}_{jk}^e into the global matrices \mathbf{H} and \mathbf{G} respectively, and the local vectors $\bar{\mathbf{u}}_k$ and $\bar{\mathbf{t}}_k$ into the global vectors \mathbf{U} and \mathbf{T} we can

write:

$$\mathbf{H}(\omega) \mathbf{U}(\omega) + \begin{bmatrix} \mathbf{A}_1^-(\omega) \\ \vdots \\ \mathbf{A}_N^-(\omega) \end{bmatrix} \begin{bmatrix} u_1(\boldsymbol{\xi}_1, \omega) \\ u_2(\boldsymbol{\xi}_1, \omega) \end{bmatrix} + \begin{bmatrix} \mathbf{A}_1^+(\omega) \\ \vdots \\ \mathbf{A}_N^+(\omega) \end{bmatrix} \begin{bmatrix} u_1(\boldsymbol{\xi}_N, \omega) \\ u_2(\boldsymbol{\xi}_N, \omega) \end{bmatrix} = \mathbf{G}(\omega) \mathbf{T}(\omega). \quad (3.20)$$

From Eq. (3.20) follows that the \mathbf{H} matrix for the corrected BEM scheme is obtained from the original \mathbf{H} matrix by adequately adding the correction coefficients \mathbf{A}_j^- and \mathbf{A}_j^+ to the columns corresponding to the end nodes, $\boldsymbol{\xi}_1$ and $\boldsymbol{\xi}_N$. Thus, the contribution from the omitted part of the boundary can be introduced in the formulation simply by adding to the original \mathbf{H} matrix the following correction matrix:

$$\mathbf{A} = \left[\begin{array}{cc|cccc|cc} A_1^-(\boldsymbol{\xi}_1, \omega) & 0 & \ddots & \vdots & A_1^+(\boldsymbol{\xi}_1, \omega) & 0 \\ 0 & A_2^-(\boldsymbol{\xi}_1, \omega) & & \ddots & 0 & A_2^+(\boldsymbol{\xi}_1, \omega) \\ \vdots & \vdots & \dots & \dots & \vdots & \vdots \\ A_1^-(\boldsymbol{\xi}_N, \omega) & 0 & & \vdots & A_1^+(\boldsymbol{\xi}_N, \omega) & 0 \\ 0 & A_2^-(\boldsymbol{\xi}_N, \omega) & & \vdots & 0 & A_2^+(\boldsymbol{\xi}_N, \omega) \end{array} \right]. \quad (3.21)$$

Hence, the corrected BEM system may be written as:

$$[\mathbf{H}(\omega) + \mathbf{A}(\omega)] \mathbf{U}(\omega) = \mathbf{G}(\omega) \mathbf{T}(\omega). \quad (3.22)$$

Equation (3.22) constitutes the BEM system modified to account for the contribution of the far-field Rayleigh surface wave through the correction matrix $\mathbf{A}(\omega)$. In the following, we propose a technique to compute the coefficients of the correction matrix by interpolating the known displacements and tractions of the Rayleigh wave

far-field solution with the same element shape functions implemented in the BEM scheme. Conveniently, this approximation allows for the correction coefficients to be computed with the same element matrices used to compute the original \mathbf{H} and \mathbf{G} matrices. Let us consider the correction \mathbf{A}_j^+ first. By interpolating $\bar{\mathbf{u}}^{SR}$ and $\bar{\mathbf{t}}^{SR}$ with the shape functions ϕ_k , Eq. (3.14) can be rewritten as:

$$\begin{aligned}
& \bar{u}_\alpha^{SR}(\boldsymbol{\xi}_N, \omega) A_\alpha^+(\boldsymbol{\xi}_j, \omega) = -c_{\alpha\beta}(\boldsymbol{\xi}_j) \bar{u}_\beta^{SR}(\boldsymbol{\xi}_j, \omega) \\
& - \sum_{e \in B_0^+ \cup B_1^+ \cup B_2} \sum_{k=1}^{N_e} \left\{ \int_{\Gamma_e} \bar{t}_{\alpha\beta}^*(\boldsymbol{\xi}_j, \eta, \omega) \phi_k(\eta) d\Gamma(\eta) \right\} \bar{u}_\beta^{SR}(\boldsymbol{\xi}_k, \omega) \\
& + \sum_{e \in B_1^+ \cup B_2^+} \sum_{k=1}^{N_e} \left\{ \int_{\Gamma_e} \bar{u}_{\alpha\beta}^*(\boldsymbol{\xi}_j, \eta, \omega) \phi_k(\eta) d\Gamma(\eta) \right\} \bar{t}_\beta^{SR}(\boldsymbol{\xi}_k, \omega), \\
& \qquad \qquad \qquad j = 1, N \quad \alpha = 1, 2,
\end{aligned} \tag{3.23}$$

and, recalling the definitions in Eqs. (3.16) and (3.17), we can write:

$$\begin{aligned}
& \mathbf{A}_j^+(\omega) \bar{\mathbf{u}}_N^{SR}(\omega) = -\mathbf{c}_j \bar{\mathbf{u}}_j^{SR}(\omega) - \sum_{e \in B_0^+ \cup B_1^+} \sum_{k=1}^{N_e} \hat{\mathbf{H}}_{jk}^e(\omega) \bar{\mathbf{u}}_k^{SR}(\omega) \\
& - \sum_{e \in B_2} \sum_{k=1}^{N_e} \hat{\mathbf{H}}_{jk}^e(\omega) \bar{\mathbf{u}}_k^{SR}(\omega) + \sum_{e \in B_1^+} \sum_{k=1}^{N_e} \mathbf{G}_{jk}^e(\omega) \bar{\mathbf{t}}_k^{SR}(\omega) + \sum_{e \in B_2} \sum_{k=1}^{N_e} \mathbf{G}_{jk}^e(\omega) \bar{\mathbf{t}}_k^{SR}(\omega), \\
& \qquad \qquad \qquad j = 1, N \quad \alpha = 1, 2.
\end{aligned} \tag{3.24}$$

Note that the fictitious boundary Γ_2 has been introduced in order compute the correction for each truncation point, $\boldsymbol{\xi}_1$ and $\boldsymbol{\xi}_N$, independently. Thus, the collocation point $\boldsymbol{\xi}_j$ never lies on Γ_2 and consequently, the additional matrices $\hat{\mathbf{H}}_{jk}^e$ and \mathbf{G}_{jk}^e for $e \in B_2$ are never singular. It should be pointed out as well that the discretization of

Γ_2 does not add degrees of freedom to the final BEM system of equations. Thus, the size of the modified BEM system in Eq. (3.22) is exactly the same as the original one.

Let us consider the assembly of the elements corresponding to the original boundary Γ^+ and the additional fictitious boundary Γ_2 independently. So, for elements and nodes that lie on Γ^+ , the local element matrices \mathbf{H}_{jk}^e and \mathbf{G}_{jk}^e and the local vectors $\bar{\mathbf{u}}_k^{SR}$, and $\bar{\mathbf{t}}_k^{SR}$ are assembled into the global matrices \mathbf{H}^+ and \mathbf{G}^+ and the global vectors \mathbf{U}_+^{SR} and \mathbf{T}_+^{SR} , respectively. Similarly, the local element matrices $\hat{\mathbf{H}}_{jk}^e$ and \mathbf{G}_{jk}^e and the local vectors $\bar{\mathbf{u}}_k^{SR}$, and $\bar{\mathbf{t}}_k^{SR}$ corresponding to Γ_2 are assembled into the global matrices \mathbf{H}_2 and \mathbf{G}_2 and the global vectors \mathbf{U}_2^{SR} and \mathbf{T}_2^{SR} , respectively. The the local matrices \mathbf{A}_j^+ , which are only defined for nodes lying on the original boundary Γ_∞^+ , are assembled into a global matrix \mathbf{A}^+ . Then, from Eq. (3.24) yields:

$$\mathbf{A}^+(\omega)\bar{\mathbf{u}}_N^{SR}(\omega) = - [\mathbf{H}^+(\omega) \mid \mathbf{H}_2(\omega)] \begin{bmatrix} \mathbf{U}_+^{SR}(\omega) \\ \mathbf{U}_2^{SR}(\omega) \end{bmatrix} + [\mathbf{G}^+(\omega) \mid \mathbf{G}_2(\omega)] \begin{bmatrix} \mathbf{T}_+^{SR}(\omega) \\ \mathbf{T}_2^{SR}(\omega) \end{bmatrix}. \quad (3.25)$$

The analogous equation for $\mathbf{A}^-(\omega)$ is derived in a similar manner.

Note that Eq. (3.25) allows to compute the coefficients of the correction matrix \mathbf{A} that appears in the modified BEM system in Eq. (3.22) by employing the same element matrices \mathbf{H}_{jk}^e and \mathbf{G}_{jk}^e that form the original BEM system and some additional but similar ones corresponding to the elements lying on the additional fictitious boundary Γ_2 . As previously indicated, the properties of the Rayleigh wave allow for the truncation of this boundary at a distance of a few Rayleigh wavelengths from the surface of the half-space. Thus, the cost of computing the additional element matrices is very low in general. Note also that no special numerical integration

scheme is required and the integrals can be computed using the same integration routines implemented in the standard BEM code.

Furthermore, in cases where the symmetry of the problems allows for its restriction to the quarter-space, the fictitious boundary Γ_2 coincides with the also fictitious symmetry boundary and, thus, belongs to the original boundary of the problem defined in the quarter-space. In this situation, no additional element matrix computation is required and the correction to account for the part of the boundary excluded from the discretization can be implemented at essentially no additional cost.

It should be pointed out as well that the above presented implementation is very simple and requires minimum modification of the routine which generates the \mathbf{H} and \mathbf{G} matrices. Once the original matrices are computed in the usual manner, they are used to obtain the correction matrices \mathbf{A}^\pm according to Eq. (3.25). Then the modified matrices are generated as indicated in Eq. (3.22).

3.4 Numerical results

The general formulation presented in the previous section is tested for two different problems. For each problem, the analytical solution is compared to two different BEM solutions. One is obtained by simple truncation of the integrals over Γ_∞ , the truncated numerical solution in short. The other BEM solution is obtained by the proposed technique, and is called the corrected numerical solution. Three-node quadratic elements have been used.

In the first problem, a free Rayleigh pulse travelling along a two-dimensional homogeneous, isotropic, linearly elastic half-space is analyzed. This example is

intended as a validation of the method, and, since the main assumption exactly holds, very accurate results are expected irrespective of the location of the truncation point. Then, Lamb's problem of a pulse load acting on a half-space with a Gaussian spatial distribution is studied. In this case, both body and Rayleigh waves are excited, and therefore it is representative of engineering applications. From the previous sections, we can anticipate that the corrected solution should be accurate for all times and everywhere in the computational domain, as long as the truncation point is chosen far enough for the body waves to be negligible at this point. In both examples, a quarter-space is analyzed, and therefore the corrected solution has the same computational cost as the truncated solution. The time pulse considered in each of these examples is a sinusoidal signal modulated by a Gaussian function, i.e.

$$g(t) = e^{-\kappa^2(t-t_0)^2} \sin [\Omega(t - t_0)], \quad (3.26)$$

where Ω is the central angular frequency, κ is twice the inverse of the Gaussian beam radius and t_0 is a time delay with respect to the initial time $t = 0^+$. This type of pulse corresponds to that generated by ultrasonic transducers. The parameters have been chosen for a central frequency of 2.56 MHz. The material properties are those of aluminum and no damping has been taken into account.

3.4.1 Free Rayleigh pulse problem

Consider the above described pulse of a unit amplitude Rayleigh wave propagating along the free surface of a half-space. This wave can be reproduced in the numerical method by considering a quarter-space, and by imposing on the fictitious vertical

boundary the known displacements corresponding to the Rayleigh wave. The truncated and corrected numerical schemes are employed to obtain displacements on the free surface, which are then compared to those of the Rayleigh wave. The time domain analytical displacements are obtained by convolution with the pulse.

Both the time and the space discretization have been designed according to the requirements of the central frequency. The sampling of the time signal for the discrete Fourier transform has been design so that the central period is represented with at least 6 sample points. The element size is selected to have at least 4 elements per Rayleigh wavelength λ_R . Finally, the domain has been truncated at distances of $10\lambda_R$ along the surface and $4\lambda_R$ along the fictitious vertical boundary of the quarter-space. Note that the assumed form of the far-field solution is exactly valid everywhere, since the propagating wave is a Rayleigh wave. Therefore, for this particular case, the corrected results are independent of the location of the truncation point.

Figures 3.2 and 3.3 show the time signal at two different locations on the surface, $x_1 = 0.5\lambda_R$ and the truncation point $x_1 = 10\lambda_R$, respectively. For both locations, the time signals of the analytical solution and those of the corrected numerical method show excellent agreement for all times, as expected. Although the time signals at only two points are depicted, this agreement holds throughout the computational domain, even for the truncation point $x_1 = 10\lambda_R$. By contrast, apparent spurious reflections can be observed in the truncated solution. For $x_1 = 0.5\lambda_R$, these reflections are well separated from the physical signal, and for short times, the truncated method provides accurate results. However, for longer times, or closer to the truncation point, the truncated numerical solution is noticeably distorted. Indeed, the

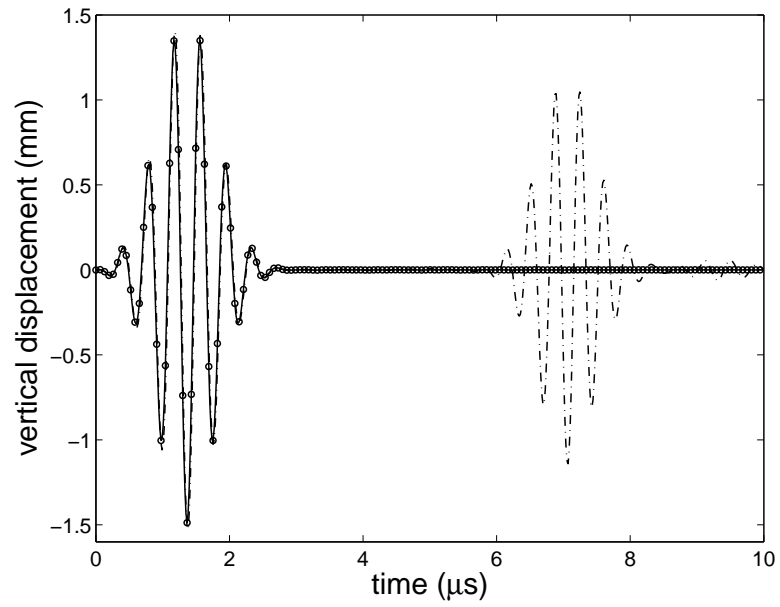


Figure 3.2: Time signal at $x_1 = 0.5\lambda_R$ (λ_R is the Rayleigh wavelength for the central frequency) for the free Rayleigh pulse problem. The solid line corresponds to the analytical solution. The dashed line and the circles correspond to the truncated and the corrected BEM models, respectively.

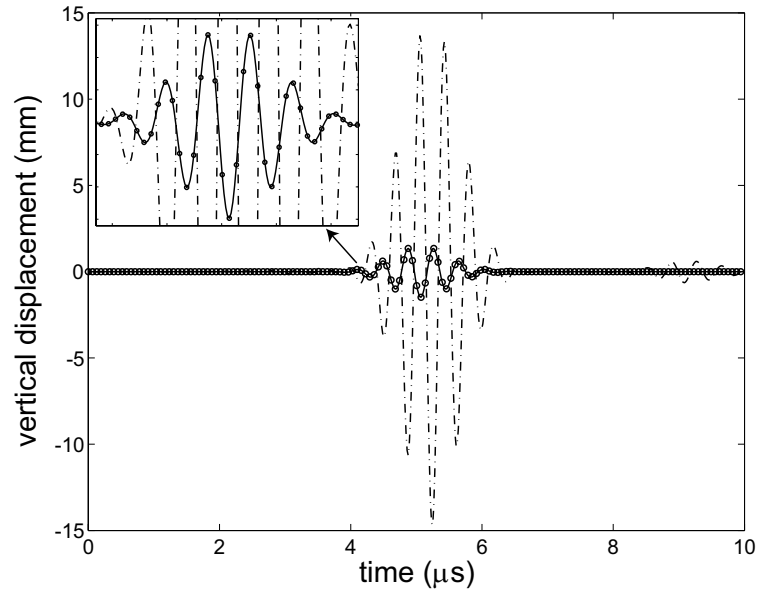


Figure 3.3: Time signal at the truncation point ($x_1 = 10\lambda_R$, λ_R being the Rayleigh wavelength for the central frequency) for the free Rayleigh pulse problem. The solid line corresponds to the analytical solution. The dashed line and the circles correspond to the truncated and the corrected BEM models, respectively.

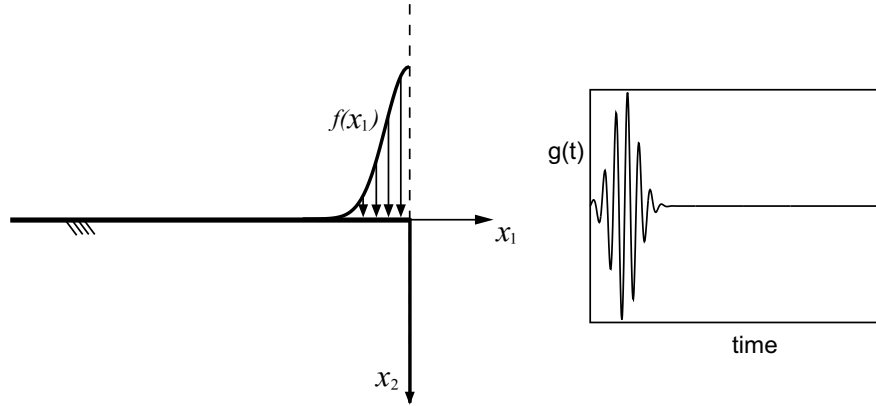


Figure 3.4: Schematic of Lamb's problem with Gaussian spatial distribution.

results in $x_1 = 10\lambda_R$ for the truncated method show an artificial amplification of the signal.

These results serve as a validation for our method. As expected, the numerically obtained value for R^- is one within machine precision.

3.4.2 Transient Lamb's problem

The aluminum half-space is subjected to the action of a pulsed vertical load with Gaussian spatial distribution. The time dependence is again given by Eq. (3.26). The radius of the Gaussian function has been taken as $0.3 \lambda_R$. Invoking the symmetry of the problem, only a quarter-space is analyzed with symmetry boundary conditions along the fictitious vertical boundary (see Fig. 3.4).

For this example, only an asymptotic analytical solution on the surface is available, which can be obtained from the solution for a concentrated load of time-harmonic dependence (Lamb, 1904) by convolution in time with the pulse, and superposition in space.

The distance at which the body waves have sufficiently attenuated to become negligible can be estimated given the frequency content of the signal. This guides the selection of the truncation point. Here, the truncation point on the surface is located at a distance of $60\lambda_R$ from the symmetry axis. Note that the fictitious boundary along the symmetry axis does not carry Rayleigh surface waves. Thus, the simple truncation of this boundary leads to accurate results and no correction is needed. Here, this boundary is truncated at a distance of $60\lambda_R$ from the surface.

Figures 3.5 and 3.6 show analogous results as in the previous example. The points at which the time signal is plotted are far enough from the source for the asymptotic analytical solution to be valid. Again, the corrected numerical solution shows excellent agreement with the analytical solution, and it does so for any time and location on the computational boundary. By contrast, the truncated solution exhibits spurious reflections. In particular, for $x_1 = 60\lambda_R$, i.e. right on the truncation point, the artificial reflection interferes with the direct signal.

These examples show that, as opposed to the simple truncation, the proposed correction allows for the undamped Rayleigh waves to escape the computational domain without producing reflections from its ends, provided the truncation point is located at sufficient distance from the source region. Thus, the corrected BEM numerical solution is accurate everywhere in the computational domain and for all computed times.

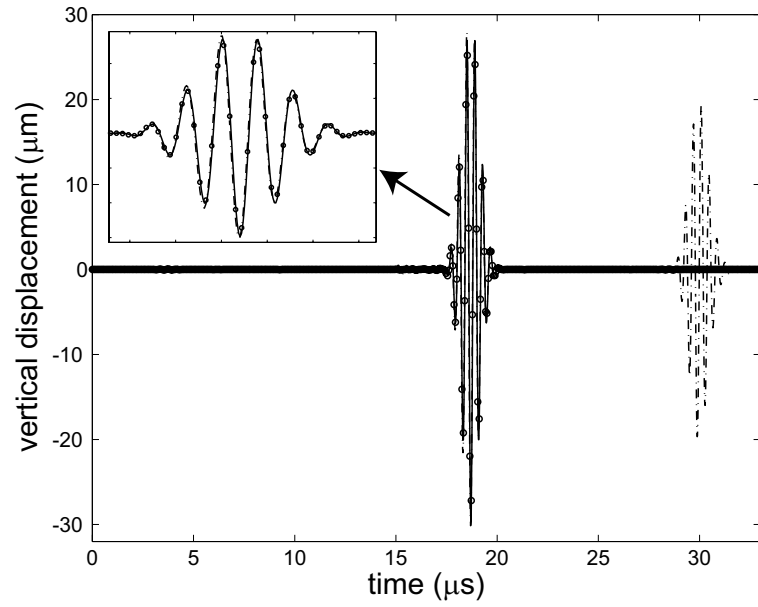


Figure 3.5: Time signal at $x_1 = 45\lambda_R$ (λ_R is the Rayleigh wavelength for the central frequency) for the transient Lamb's problem with Gaussian spatial distribution. The solid line corresponds to the analytical solution. The dashed line and the circles correspond to the truncated and the corrected BEM models, respectively.

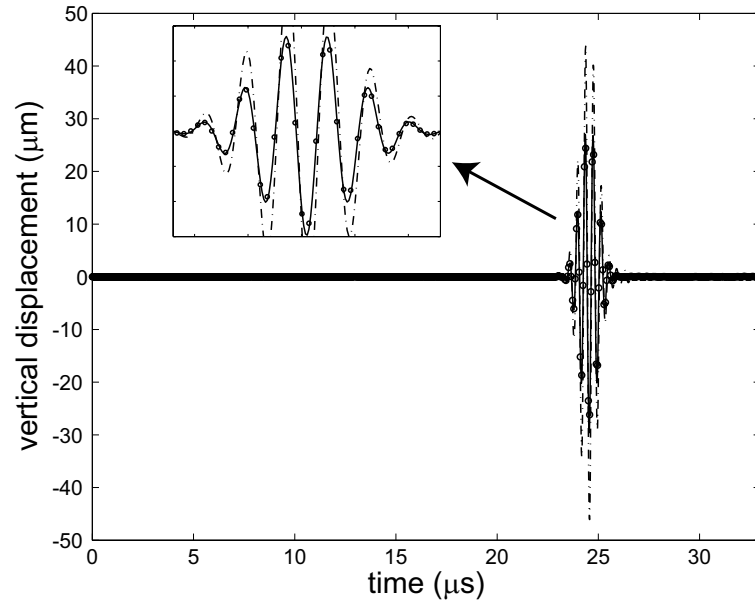


Figure 3.6: Time signal at the truncation point ($x_1 = 60\lambda_R$, λ_R being the Rayleigh wavelength for the central frequency) for the transient Lamb's problem with Gaussian spatial distribution. The solid line corresponds to the analytical solution. The dashed line and the circles correspond to the truncated and the corrected BEM models, respectively.

3.5 Conclusions

A simple, elegant approach is proposed to correct the error introduced by the truncation of the infinite boundary in the BEM modeling of elastodynamic wave propagation in semi-infinite domains. The proposed method exploits the knowledge of the asymptotic behavior of the solution to adequately correct the BEM displacement system matrix for the truncated problem to account for the contribution of the omitted part of the boundary. As opposed to the infinite element approach which requires special integration schemes in general, here the reciprocity theorem of elastodynamics is invoked to express this contribution in terms of integrals of known quantities over the discretized boundary of the domain and additional fictitious boundaries. By interpolating the far-field solution with the element shape functions, these integrals are directly obtained from the same element integrals that form the original BEM system. As a result, the proposed method is easy to implement and comes at very low additional cost as compared to the simple truncation of the boundary.

It is important to note that the additional boundaries are introduced for direct integration purposes only and do not add degrees of freedom to the final BEM system of equations. In some particular cases, e.g. a symmetric half-space which is analyzed as a quarter-space, no additional fictitious boundary is needed and the contribution from the omitted part of the boundary is expressed in terms of integrals over the discretized boundaries only with no additional cost. In general, the cost of computing the integrals over the additional fictitious boundaries is very low.

The formulation – although it can be extended to a broader range of problems – has been presented in detail in the context of the frequency domain BEM for two-

dimensional elastodynamic problems for a homogeneous, isotropic, linearly elastic half-space. In this type of problems, Rayleigh surface waves propagate along the surface of the half-space without attenuation. The simple truncation of the boundary then produces considerable reflections from the end points of the domain. It has been shown through simple test examples that the proposed treatment of the infinite boundary allows the Rayleigh waves to escape the computational domain without producing spurious reflections at the end points, and it therefore eliminates the need for artificial damping. The accuracy of the solution provided by the proposed model depends on the accuracy of the assumption that Rayleigh waves strongly dominate at the end points of the computational domain. However, once the computational domain is extended far enough from the source region for this assumption to hold, then the solution is accurate everywhere in the computational domain and for all computed times. This is not the case in the truncated model, where the accuracy of the solution is degraded near the ends of the computational domain and for sufficiently long times reflections are observed at any location.

Chapter 4

Modeling of the Scanning Laser Source technique

A model for the Scanning Laser Source (SLS) technique is presented. The SLS technique is a novel laser based inspection method for the ultrasonic detection of small surface-breaking cracks. The generated ultrasonic signal is monitored as a line-focused laser is scanned over the defect, and characteristic changes in the amplitude and the frequency content are observed. The modeling approach is based on the decomposition of the field generated by the laser in a cracked two-dimensional half-space, by virtue of linear superposition, into the incident and the scattered fields. The incident field is that generated by laser illumination of a defect-free half-space. A thermoelastic model has been used which takes account of the effect of thermal diffusion from the source, as well as the finite width and duration of the laser source. The scattered field incorporates the interactions of the incident field with the surface-breaking crack. It has been analyzed numerically by the boundary element method. A comparison with an experiment for a large defect shows that the model captures the observed phenomena. A simulation for a small crack illustrates the ability of the SLS technique to detect defects smaller than the wavelength of the generated

Rayleigh wave.

4.1 Introduction

Ultrasound has been widely applied in the field of nondestructive evaluation for the detection and characterization of anomalies of various kinds. Since the 1960's, pulsed lasers have emerged as an alternative to traditional techniques for the generation and detection of ultrasound. There are generally two mechanisms for such wave generation, depending on the amount of energy deposition by the laser pulse, namely ablation at very high power, and thermoelastic generation at moderate power operation. The latter does not damage the surface of the material, and is therefore suitable for applications in nondestructive evaluation.

The generation of ultrasound by laser irradiation provides a number of advantages over the conventional generation by piezoelectric transducers, namely high spatial resolution, non-contact generation and detection of ultrasonic waves, use of fiber optics, narrow-band and broad-band generation, absolute measurements, and ability to operate on curved and rough surfaces and at hard-to-access locations. On the receiving side, surface ultrasonic waves can be detected using piezoelectric (PZT) or EMAT transducers, or optical interferometers in a completely laser-based system. Ultrasound generated by laser irradiation contains a large component of surface wave motion, and is therefore particularly useful for the detection of surface-breaking cracks.

The laser illumination of a pristine surface generates a well-defined wave package. Traditional techniques for the detection of surface-breaking cracks rely on monitor-

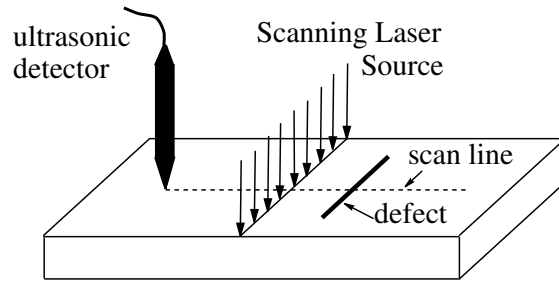


Figure 4.1: Configuration for the SLS technique.

ing the reflections (pulse-echo) or the changes in the amplitude of the transmission (pitch-catch) of this given incident signal caused by the presence of a defect. Nevertheless, for small defects relative to the wavelength of the generated Rayleigh wave, these reflections and changes in the transmission are often too weak to be detected with existing laser detectors. The recently proposed Scanning Laser Source technique (SLS) provides an alternative inspection method which overcomes these size limitations (Kromine et al., 2000a).

The Scanning Laser Source (SLS) technique employs a line-focused high-power laser source which is swept across the test specimen and passes over surface-breaking anomalies (Kromine et al., 2000b; Kromine et al., 2001; Fomitchov et al., 2002). The generated ultrasonic waves are detected with an ultrasonic detector located either at a fixed distance from the laser source or at a fixed position on the test specimen. Figure 4.1 sketches the inspection technique. The distinguishing feature of this method is that it monitors the changes in the laser generated signal as the illuminated region is swept over a defect, rather than the interactions of a well-established incident signal with the defect. The presence of a defect modifies the generation conditions and produces reflections, leading to clear differences in the

shape of the signal, its amplitude, and its frequency content, as compared to the signal generated on a defect-free surface. Thus, a distinct signature of the defect can be observed in the peak-to-peak amplitude and maximum frequency of the generated signal as the laser passes over the defect, as illustrated in the experimental observations and numerical simulations presented later in this Chapter. There is experimental evidence that this signature is noticeable even for cracks much smaller than the detection threshold for conventional methods and for arbitrary orientation of the crack with respect to the direction of scanning.

In this Chapter, a model for the SLS technique is presented and compared against experiments. The objective is to identify the relevant physical mechanisms responsible for the observed behavior, and possibly optimize the inspection technique. A scanning laser line-source whose axis is parallel to a relatively long surface-breaking crack in a structure is considered. This situation is modeled as a two-dimensional, plane strain thermoelastic problem and the test specimen is approximated by a homogeneous, isotropic, linearly elastic half-space. The surface-breaking crack is assumed to be mathematically sharp and perpendicular to the surface of the half-space. Sohn and Krishnaswamy (2002) have analyzed the SLS technique in the above situation numerically by modeling the wave propagation phenomena with a two-dimensional mass spring lattice model, and the line-focused laser source with a simplified shear dipole model which neglects thermal diffusion. Here, by virtue of linear superposition, the field generated by the line-focused laser source in the presence of the defect is decomposed into the incident and the scattered fields (see Fig. 4.2). The incident field is that generated by line-focused laser source illumination of the half-space in the absence of the defect, and is treated as a thermoelastic prob-

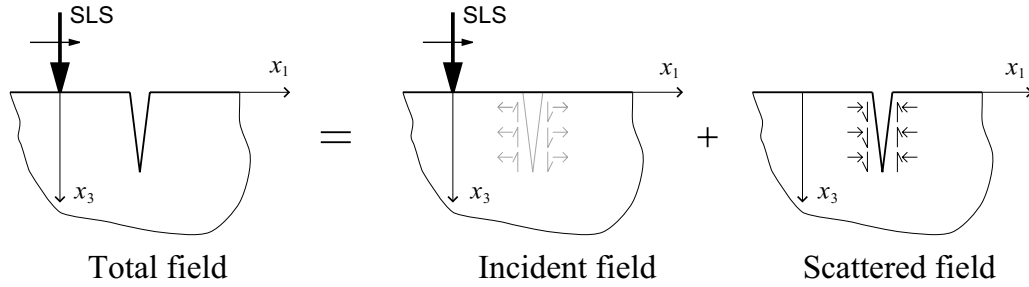


Figure 4.2: Decomposition of the total field into incident and scattered fields

lem. The scattered field is defined as the field generated in the cracked half-space by tractions acting on the crack faces that cancel out those produced by the laser line-source on the same plane, so that the condition of traction free crack faces is met after the superposition of the incident and the scattered fields. Each problem is then solved separately.

The problem of the incident field is that of thermoelastic laser-generation of ultrasound under plane strain conditions. Since the 1960's researchers have been studying the generation of ultrasound by lasers (Hutchins, 1988). Many models have been developed, most of them defining an elastic source equivalent to the laser source, and thereby neglecting its thermoelastic nature. As pointed out by earlier authors (Scruby and Drain, 1990), intuitively the actions of a local generation of a temperature field and the application of an elastic shear dipole acting on the surface should be expected to produce equivalent fields. This approximation assumes that all the energy is deposited at the surface and does not diffuse. Thus, it neglects the two basic physical mechanisms through which thermal energy penetrates into the bulk of material giving rise to subsurface thermal sources, namely optical absorption of the laser energy into the bulk material and thermal diffusion from the heat source.

The subsurface thermal sources have a localized effect which is significant near the laser source and becomes negligible far away from it. Therefore, while the purely elastic shear dipole model provides a good approximation of the far-field, it is unable to accurately predict the near-field. This fact becomes particularly noticeable in its inability to predict a basic feature of the near-field, the so-called precursor. The precursor is a small, but relatively sharp initial spike observed experimentally at the longitudinal wave arrival, which has been related to the presence of subsurface sources (Doyle, 1986). In the context of the SLS technique, the laser generated field has to be determined accurately as the source approaches the position of the crack, since the tractions generated on the plane that represents the position of the crack are the input for the scattering problem. Therefore, it is clear that, for our purposes, the effects of subsurface deposition of energy need to be included in the formulation of the problem of the incident near field.

Arias and Achenbach (2003c) have developed a two-dimensional model for the line-focused laser generation of ultrasound based on a unified treatment of the thermoelastic problem in plane strain. This model takes account of the finite width of the source, the temporal shape of the pulse and the subsurface sources arising from thermal diffusion and optical penetration. The thermoelastic problem in a homogeneous, isotropic, linearly elastic half-space is solved analytically in the Fourier-Laplace transform domain. The doubly transformed solution is inverted numerically to produce theoretical waveforms. The shear dipole model follows from appropriate limits. This thermoelastic model is used here to obtain an accurate description of the incident field in a metallic half-space. In metals, the subsurface sources arise mainly from thermal diffusion, since the optical absorption depth is

very small compared to the thermal diffusion length. Thus, the limit case of strong optical absorption is considered. The corresponding formulation is detailed in section 4.2 and some basic results relevant to the modeling of the SLS technique are presented.

The scattered field is defined as that generated on the cracked half-space by suitable tractions acting on the faces of the crack. These tractions are equal and opposite to those generated by the incident field in the un-cracked half-space when evaluated on the plane of the crack. By defining the scattered field in this manner, it is assumed that the crack does not affect the diffusion of heat in the specimen. This assumption allows for the coupled thermoelastic scattering problem to be reduced to an isothermal elastic problem of two-dimensional wave diffraction by a surface-breaking crack in a half-space. This simplification is considered to be realistic for small fatigue cracks and has proven to be sufficiently accurate. The scattering problem is solved numerically by the boundary element method (BEM). The details are presented in Section 4.3.

The two problems are solved separately to obtain vertical surface displacements waveforms for the incident and the scattered field at the receiver location. The superposition of these waveforms yields the theoretical SLS time signal for a certain position of the source. Then different SLS positions are considered and the peak-to-peak amplitude of each corresponding signal is plotted versus the SLS position to construct the theoretical amplitude signatures. Similarly, by considering the frequency content of each signal and plotting the maximum frequency versus SLS position, the frequency signature of the SLS technique is generated.

4.2 The incident field

The thermoelastic problem is formulated in the context of the generalized theory of thermoelasticity which assumes a hyperbolic description of heat conduction. The governing equations of the thermal and the elastic problems are in principle doubly coupled. However, in the thermoelastic regime, the heat produced by mechanical deformation can be neglected. With this so-called thermal stress approximation, the equations are coupled only one-way through the thermal stress term. The governing equations for an isotropic solid are:

$$\nabla^2 T - \frac{1}{\kappa} \dot{T} - \frac{1}{c^2} \ddot{T} = -\frac{q}{k}, \quad (4.1)$$

$$\mu \nabla^2 \mathbf{u} + (\lambda + \mu) \nabla(\nabla \cdot \mathbf{u}) = \rho \ddot{\mathbf{u}} + \beta \nabla T, \quad (4.2)$$

where T is the absolute temperature, \mathbf{u} is the displacement vector field, κ is the thermal diffusivity, c is the heat propagation speed which is taken to be equal to the longitudinal wave speed, k is the thermal conductivity, β is the thermoelastic coupling constant: $\beta = (3\lambda + 2\mu)\alpha_T$, α_T is the coefficient of linear thermal expansion and q is the heat source due to laser line-source illumination. A suitable expression for the surface heat deposition q in the solid along an infinitely long line is

$$q = E(1 - R_i)f(x_1)g(t), \quad (4.3)$$

with

$$f(x_1) = \frac{1}{\sqrt{2\pi}} \frac{2}{R_G} e^{-2x_1^2/R_G^2}, \quad (4.4)$$

and

$$g(t) = \frac{8t^3}{v^4} e^{-2t^2/v^2}, \quad (4.5)$$

where E is the energy of the laser pulse per unit length, R_i is the surface reflectivity, R_G is the Gaussian beam radius, v is the laser pulse risetime (full width at half maximum). The coordinate axis x_1 is directed along the surface perpendicularly to the line-source, and x_3 normal to the surface pointing inwards.

Equation (4.3) represents a strip of illumination since it is defined by a Gaussian in x_1 . The Gaussian does not vanish completely with distance, but its value becomes negligible outside a strip. The source is spread out in time according to the function proposed by Schleichert et al. (1989). For both the temporal and the spatial profile, the functional dependence has been constructed so that in the limit $v \rightarrow 0$ and $R_G \rightarrow 0$, an equivalent concentrated line-source is obtained.

The system of governing equations, which we consider in the plane strain approximation for the case of an infinitely long line-source, must be supplemented by initial and boundary conditions. The initial conditions are that the half-space is initially at rest. The boundary conditions include thermal and mechanical conditions. If the boundary is defined by $x_3 = 0$, then the considered thermal boundary condition is

$$\frac{\partial T}{\partial x_3} = 0, \quad \text{at } x_3 = 0. \quad (4.6)$$

This condition implies that heat does not flow into or out of the half-space via the boundary. The heat that is generated by the laser is deposited inside the half-space just under the surface. The mechanical condition is that the tractions are zero on

the surface ($x_3 = 0$), i.e.

$$\sigma_{31} = \mu(u_{3,1} + u_{1,3}) = 0, \quad \text{at } x_3 = 0, \quad (4.7)$$

$$\sigma_{33} = \lambda(u_{1,1} + u_{3,3}) + 2\mu u_{33,3} - \beta\Delta T = 0, \quad \text{at } x_3 = 0. \quad (4.8)$$

Equations (4.1) and (4.2) with the above boundary and initial conditions are solved using standard Fourier-Laplace transform techniques for two-dimensional, time dependent systems. The problem is first reformulated in terms of the usual displacement potentials: the dilatational potential ϕ and the rotational potential $\boldsymbol{\psi} = \nabla \times (0, 0, \psi)$, where ψ is set to satisfy the homogenous scalar wave equation. The exponential Fourier transform in the spatial coordinate x_1 and the one-sided Laplace transform in time are then applied to the governing equations, and the boundary and initial conditions. A closed form solution is obtained for the transformed potentials. The transformed displacements and stresses can be derived from the solution for the transformed potentials. The expressions in the limit case of

strong optical absorption are:

$$\tilde{u}_1 = ip \frac{\Gamma \kappa}{sR} \left\{ M e^{-\zeta x_3} + 2\eta(\eta^2 + p^2) \left(1 - \frac{\zeta}{\xi} \right) e^{-\eta x_3} - \frac{R}{\xi} e^{-\xi x_3} \right\}, \quad (4.9)$$

$$\tilde{u}_3 = \frac{\Gamma \kappa}{sR} \left\{ M \zeta e^{-\zeta x_3} + 2p^2(\eta^2 + p^2) \left(1 - \frac{\zeta}{\xi} \right) e^{-\eta x_3} - R e^{-\xi x_3} \right\}, \quad (4.10)$$

$$\begin{aligned} \tilde{\sigma}_{11} = \mu \frac{\Gamma \kappa}{sR} \{ & M(2\zeta^2 - b^2 s^2) e^{-\zeta x_3} \\ & + 4p^2 \eta(\eta^2 + p^2) \left(1 - \frac{\zeta}{\xi} \right) e^{-\eta x_3} + \frac{R}{\xi} (b^2 s^2 - 2\xi^2) e^{-\xi x_3} \}, \end{aligned} \quad (4.11)$$

$$\tilde{\sigma}_{33} = \mu \frac{\Gamma \kappa}{sR} (\eta^2 + p^2) \left\{ -M e^{-\zeta x_3} - 4\eta p^2 \left(1 - \frac{\zeta}{\xi} \right) e^{-\eta x_3} + \frac{R}{\xi} e^{-\xi x_3} \right\}, \quad (4.12)$$

$$\tilde{\sigma}_{13} = 2\mu ip \frac{\Gamma \kappa}{sR} \left\{ M \zeta e^{-\zeta x_3} + (\eta^2 + p^2) \left(1 - \frac{\zeta}{\xi} \right) e^{-\eta x_3} - R e^{-\xi x_3} \right\}, \quad (4.13)$$

with $\zeta^2 = p^2 + a^2 s^2$, $\eta^2 = p^2 + b^2 s^2$, $\xi^2 = \zeta^2 + \frac{s}{\kappa}$, $R = (\eta^2 + p^2)^2 - 4\zeta\eta p^2$, and $M = (\eta^2 + p^2)^2/\xi - 4\eta p^2$. Also, $\Gamma = \beta Q_0 Q_p(p) Q_s(s)/(\lambda + 2\mu)$ and

$$Q_0 = \frac{E}{k} (1 - R_i), \quad (4.14)$$

$$Q_p(p) = \frac{1}{\sqrt{2\pi}} e^{-p^2 R_G^2/8}, \quad (4.15)$$

$$Q_s(s) = \mathcal{L} \left\{ \frac{8t^3}{v^4} e^{-2t^2/v^2} \right\}, \quad (4.16)$$

where \mathcal{L} indicates Laplace transform, (t, s) is the Laplace pair and (x, p) is the Fourier pair, λ and μ are the Lamé constants, a and b are the slownesses of the longitudinal and the transverse waves, respectively. The Laplace transformed and the Fourier transformed fields are denoted with an bar and a tilde, respectively.

The solutions for the displacements and tractions in the domain of Fourier-Laplace transformed variables provide insight to the physics of the problem. Equa-

tions (4.9)-(4.13) indicate three modes of energy transport, namely longitudinal waves (associated with the terms proportional to $e^{-\zeta x_3}$), transverse waves (associated with the terms proportional to $e^{-\eta x_3}$) and thermal diffusion (associated with the terms proportional to $e^{-\xi x_3}$). These three mechanisms can be observed in the illustrative waveforms presented later in this Section.

The solution in the transformed domain is then inverted numerically. The integral of the inverse Fourier transform is evaluated by using a Romberg integration routine with polynomial extrapolation (Press et al., 1986). The general method used for the numerical inversion of the Laplace transform is based on a technique developed by Crump (1976).

In order to model the SLS technique, the tractions on vertical planes located at different positions with respect to the laser line-source (input for scattering problem) need to be computed, as well as vertical surface displacements (incident field for superposition). Here, the values for the parameters of the model are: $c_L = 6.321 \text{ mm}/\mu\text{s}$, $c_T = 3.11 \text{ mm}/\mu\text{s}$, $\alpha_T = 2.2 \cdot 10^{-5} \text{ 1/K}$, $\kappa = 6.584 \cdot 10^{-5} \text{ mm}^2/\mu\text{s}$, $k = 160 \text{ W/mK}$, $R_i = 91\%$, $E = 1 \text{ mJ}$ per unite length of the line-source, $R_G = 0.14 \text{ mm}$ and $v = 10 \text{ ns}$.

Figure 4.3 displays the theoretical waveforms of surface normal displacement at four different distances from the axis of the laser line-source, where a negative displacement is in the positive x_3 direction, i.e. inwards. All the waveforms correspond to distances far from the irradiated region, so that the thermal effects are negligible. Thus, the predictions of the thermoelastic model show excellent agreement with those of the shear dipole model, as expected (Arias and Achenbach, 2003c). In the far-field, the waveforms are dominated by the Rayleigh surface wave which

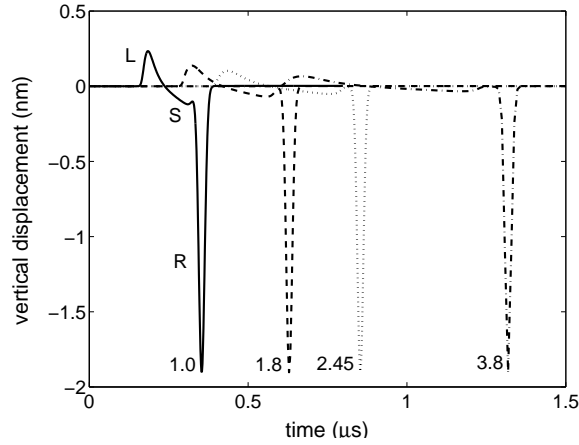


Figure 4.3: Normal displacement on the surface. The numeric labels next to the waveforms indicate the distance in mm from the axis of the laser line-source. The labels L, S and R denote longitudinal, shear and Rayleigh surface waves, respectively. A negative value represents an inward normal displacement.

travels along the surface without geometrical attenuation. The Rayleigh pulse is a monopolar inward displacement, whose temporal profile reproduces that of the laser beam, in contrast with the bipolar Rayleigh pulse produced by a point-source. The attenuating longitudinal and shear waves can also be identified in the waveforms.

Figure 4.4 shows the σ_{11} stress component on the surface at several distances from the axis of the laser line-source. The theoretical waveforms exhibit quite different behavior for small and large distances from the laser source. The stress field inside the heated region, i.e. $x_1 < 0.2$ mm in Fig. 4.4, is dominated by the thermal stresses generated by the laser induced temperature field, which diffuse into the material at a slower time scale as compared to the propagation of elastic waves. Well inside the irradiated region, i.e. $x_1 \leq 0.04$ mm, a high compressive σ_{11} field is generated since the rapid expansion of the heated region is laterally constrained by the unheated

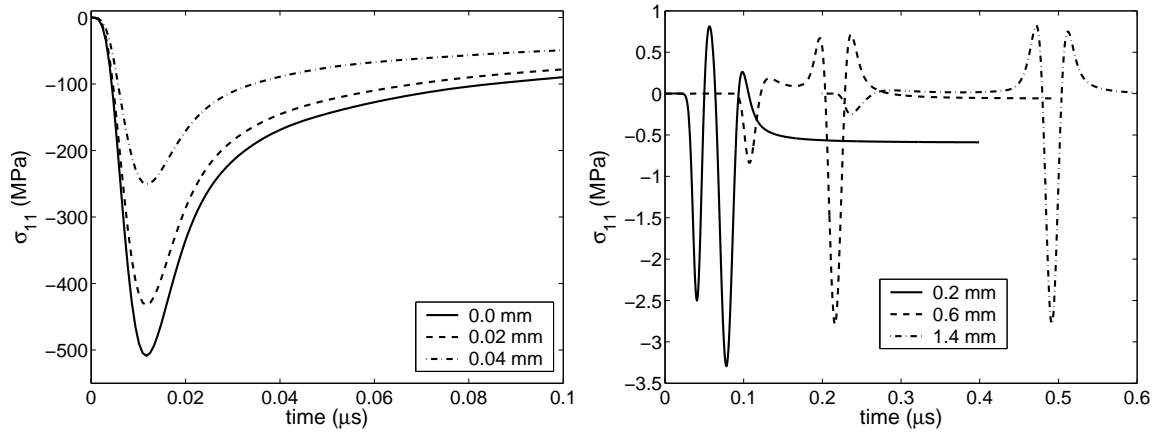


Figure 4.4: Stress σ_{11} on the surface. The legend indicates the distance to the epicentral axis. A negative value indicates compression.

surrounding material. Far away from the source the thermal effects are negligible and the propagation of elastic waves can be clearly identified. The Rayleigh surface wave induces a compressive σ_{11} pulse preceded and followed by smaller tensile pulses.

Figure 4.5 shows theoretical waveforms at various depths of normal σ_{11} and shear σ_{31} tractions on two vertical planes: one close to the axis of the laser line-source (two left-most plots) and the other far from it (two right-most plots). In these figures, a negative normal stress indicates compression and a positive shear stress on the top face of an element points in the negative x_1 direction. Again, the shape of the waveforms is qualitatively quite different for small and large distances from the laser source. The thermal stresses are apparent in the near-field for small depths. The propagation of the different wavefronts at different speeds is also apparent.

It is clear that, since the generated fields differ near and far from the laser source, the corresponding scattered fields produced by the interaction of these fields with the crack will also be very sensitive to the distance to the laser source. The analysis of the

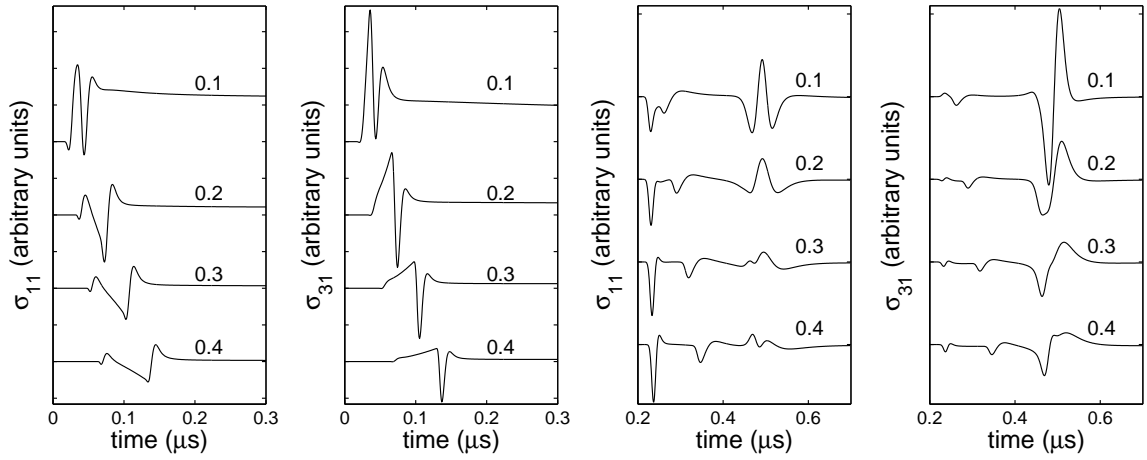


Figure 4.5: Traction on the vertical plane at 0.05 mm (left) and 1.4 mm (right) distance from the axis of the laser line-source at various depths. The numbers next to the waveforms indicate the depth in mm. A negative normal traction indicates compression and a positive shear traction on the top face of an element points in the negative x_1 direction.

incident field provides clues to interpret the experimental observations. For instance, analogously to the SLS crack signature in the maximum frequency evolution, the frequency content of the generated signal is shifted to higher frequencies as the distance to the laser source decreases and then drops for very small distances.

4.3 The scattered field

The interactions of a surface-breaking crack with the field generated by the laser in a half-space are analyzed next. By decomposing the scattered field into symmetric and anti-symmetric fields with respect to the plane of the crack, two boundary value problems for the quarter-space are obtained (see Fig. 4.6). The symmetric problem is defined by normal tractions acting on the plane of the crack which are equal and opposite to the ones generated by the incident field, whereas the anti-symmetric problem is defined by the corresponding shear tractions. Therefore, the boundary conditions for each problem are:

$$\left\{ \begin{array}{l} \sigma_{13}^{\text{sc}} = 0 \quad x = 0, \quad 0 \leq x_3 < \infty \\ \sigma_{11}^{\text{sc}} = -\sigma_{11}^{\text{in}}, \quad 0 \leq x_3 < a \\ u_1^{\text{sc}} = 0, \quad a \leq x_3 < \infty \end{array} \right. \quad (4.17)$$

for the symmetric problem and

$$\left\{ \begin{array}{l} \sigma_{13}^{\text{sc}} = -\sigma_{13}^{\text{in}}, \quad 0 \leq x_3 < a \\ \sigma_{11}^{\text{sc}} = 0 \quad x = 0, \quad 0 \leq x_3 < \infty \\ u_z^{\text{sc}} = 0, \quad a \leq x_3 < \infty \end{array} \right. \quad (4.18)$$

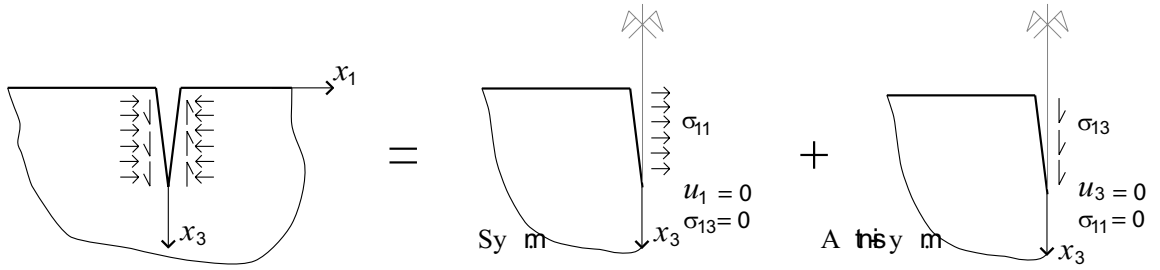


Figure 4.6: Decomposition into the symmetric and the anti-symmetric problems in a quarter-space.

for the anti-symmetric problem, where the superscripts “sc” and “in” stand for the scattered, and the incident fields respectively and a is the length of the crack. For both the symmetric and the anti-symmetric problem, the surface of the quarter-space is free of tractions. In addition, it is required that the scattered field represents outgoing waves. The governing equation for a homogeneous, isotropic, linearly elastic solid is Eq. 4.2, which in the isothermal case reduces to:

$$\mu \nabla^2 \mathbf{u}^{\text{sc}}(\mathbf{x}, t) + (\lambda + \mu) \nabla(\nabla \cdot \mathbf{u}^{\text{sc}})(\mathbf{x}, t) = \rho \ddot{\mathbf{u}}^{\text{sc}}(\mathbf{x}, t), \quad (4.19)$$

where $\mathbf{x} \in (-\infty, 0] \times [0, \infty)$ is the position vector and $t > 0$ represents time.

Each of these problems is solved numerically with a two-dimensional direct frequency domain quadratic boundary element method (Niwa et al., 1986). The symmetric and anti-symmetric problems are formulated in the frequency domain by the application of the Fourier transform to the equation and the boundary conditions, assuming a quiescent past. The resulting transformed equation of motion is:

$$\mu \nabla^2 \bar{\mathbf{u}}^{\text{sc}}(\mathbf{x}, \omega) + (\lambda + \mu) \nabla(\nabla \cdot \bar{\mathbf{u}}^{\text{sc}})(\mathbf{x}, \omega) + \rho \omega^2 \bar{\mathbf{u}}^{\text{sc}}(\mathbf{x}, \omega) = 0, \quad (4.20)$$

where ω stands for the angular frequency and the transformed displacement field is denoted with a bar. The corresponding boundary integral equations for a point $\boldsymbol{\xi}$ located on the boundary of the domain, Γ , are derived in the usual manner (Domínguez, 1993) as:

$$c_{\alpha\beta}(\boldsymbol{\xi}) \bar{u}_{\beta}^{\text{sc}}(\boldsymbol{\xi}, \omega) = \int_{\Gamma} [\bar{u}_{\alpha\beta}^*(\boldsymbol{\xi}, \mathbf{x}, \omega) \bar{t}_{\beta}^{\text{sc}}(\mathbf{x}, \omega) - \bar{t}_{\alpha\beta}^*(\boldsymbol{\xi}, \mathbf{x}, \omega) \bar{u}_{\beta}^{\text{sc}}(\mathbf{x}, \omega)] d\Gamma(\mathbf{x}),$$

$$\alpha, \beta = 1, 2, \quad (4.21)$$

where $\bar{u}_{\alpha\beta}^*$ and $\bar{t}_{\alpha\beta}^*$ are the full-space frequency domain elastodynamic fundamental solution displacement and traction tensors respectively. Note that $\bar{u}_{\alpha\beta}^*(\boldsymbol{\xi}, \mathbf{x}, \omega)$ and $\bar{t}_{\alpha\beta}^*(\boldsymbol{\xi}, \mathbf{x}, \omega)$ represent the “ β ” component of the displacement and the traction on the boundary, respectively, at the point \mathbf{x} due to a unit time-harmonic load of angular frequency ω applied at the point $\boldsymbol{\xi}$ in the direction “ α ”. Also, $\bar{u}_{\beta}^{\text{sc}}$, $\bar{t}_{\beta}^{\text{sc}}$ are frequency domain displacements and tractions on the boundary, and $c_{\alpha\beta}$ is called the jump coefficient given by:

$$c_{\alpha\beta}(\boldsymbol{\xi}) = \begin{cases} \frac{1}{2}\delta_{\alpha\beta}, & \text{if } \Gamma \text{ is smooth at } \boldsymbol{\xi}, \\ c_{\alpha\beta}, & \text{if } \Gamma \text{ has a corner at } \boldsymbol{\xi}, \end{cases} \quad (4.22)$$

where $\delta_{\alpha\beta}$ represents the Kronecker delta. The jump coefficient for corner points can be derived by an indirect approach as described by Domínguez (1993). The integrals in Eq. (4.21) are interpreted in the sense of the Cauchy Principal Value.

The boundary integral equations are solved numerically for the symmetric and anti-symmetric transformed displacements on the boundary. A discretization with isoparametric quadratic boundary elements is introduced. A singular traction quarter-

point boundary element has been used to reproduce the singular behavior of the stresses at the crack tip (Blandford et al., 1981). After solving the transformed problems, the transient solution is obtained by numerical inversion of the Fourier transform with a fast Fourier transform (FFT) algorithm.

Note that the above presented approach entails the solution of two boundary value problems on a quarter-space, instead of just one on the half-space. However, it avoids the well-known degeneracy of the conventional BEM for the flat cracks, which is essentially associated with the ill-posed nature of problems with two coplanar faces (Cruse, 1987).

It has been shown that the sharpness of the laser line-source generated signal increases as the line becomes narrower or the laser pulse shorter (Arias and Achenbach, 2003c). For instance, in the limit of the shear dipole, the generated Rayleigh surface wave is a monopolar pulse propagating along the surface of the half-space which reproduces the shape of the laser pulse. The high-frequency content of the incident field for narrow lines and short pulses imposes stringent conditions on the number of frequencies to be computed for an accurate sampling in a given time window. The requirement of describing a wavelength with about 10 nodes results in a quite small element size. On the other hand, in experiments the receiver is located at sufficient distance from the crack to allow for the scanning of the specimen surface, and thus the region of interest, where accurate solutions are needed, can be relatively large, leading to a high number of elements.

The infinite surface of the quarter-space has to be truncated for numerical calculation purposes. The simple truncation introduces spurious reflections from the ends of the computational boundary that distort the numerical solution in the region

close to the truncation point. Note that in a two-dimensional geometry, undamped Rayleigh waves do not exhibit geometrical attenuation, and will always produce reflections in a simply truncated mesh. This issue is typically addressed by extending the computational mesh far beyond the region of interest and adding a small amount of damping. Arias and Achenbach (2003b) formulated a correction for the truncation of the infinite boundary which allows the undamped Rayleigh waves to escape the computational domain without producing spurious reflections from its end nodes. This method exploits the knowledge of the asymptotic behavior of the solution – here Rayleigh surface waves are assumed to dominate the far-field solution – to adequately correct the BEM displacement system matrix for the truncated problem to account for the contribution of the omitted part of the boundary. The reciprocity theorem of elastodynamics allows for a convenient computation of this contribution involving the same element integrals that form the original BEM system. The proposed method is easy to implement and, in the case of a quarter-space, it comes at essentially no additional cost as compared to the simple truncation of the boundary. The accuracy of the solution provided by the proposed model depends on the accuracy of the assumption that Rayleigh waves strongly dominate at the end points of the computational domain. However, once the computational domain is extended far enough from the source region for this assumption to hold, then, unlike the simply truncated solution, the corrected solution is accurate everywhere in the computational domain and for all computed times. In situations where the region of interest extends far beyond the source region where waves are generated, the proposed method can reduce the extent of the computational boundary.

The facts pointed out lead to large computational meshes and, thus, high memory

requirements and computational times. In efforts to reduce the computational time, the natural parallelism of the frequency domain approach has been exploited in the computer implementation.

4.4 Representative examples

4.4.1 Comparison with experiment for a large notch

Sohn and Krishnaswamy (2003) have carried out experiments on an aluminum specimen in the presence of a notch of 2.5 mm in depth and 0.3 mm in width. A Q-switched line-focused laser was used at 10 mJ energy deposition. The width of the illumination strip was estimated to be around 200 μm width by burn marks on photosensitive paper. The duration of the pulse was 70 ns. The laser source scanned the specimen from a distance of 3.0 mm from the left face of the notch to a distance of 0.5 mm past the left face of the notch. A laser detector was used to record surface normal displacements at a distance of 16 mm from the left face of the crack in each scanning step (see Fig. 4.7). Both the signals recorded at the receiver and the resulting peak-to-peak amplitude evolution with the position of the laser source were provided.

A numerical example inspired in this experiment is presented next. The notch has been replaced by a surface-breaking crack of the same depth in the plane of the left face of the notch. It has been verified, that this approximation does not have a significant effect on the response of the system at the receiver for a notch of this depth relative to the wavelengths of the generated Rayleigh wave. The material properties used in the simulation are: $c_L = 5.9 \text{ mm}/\mu\text{s}$, $c_T = 3.1 \text{ mm}/\mu\text{s}$,

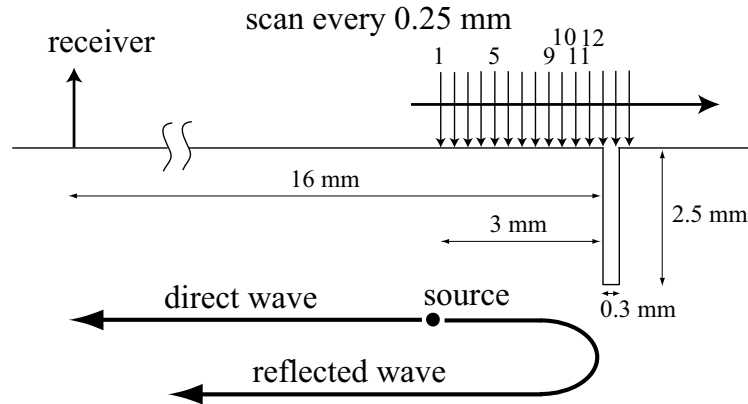


Figure 4.7: Experimental setup for the SLS inspection of a notched specimen.

$\alpha_T = 2.2 \cdot 10^{-5} \text{ 1/K}$, $\kappa = 1.0 \cdot 10^{-4} \text{ mm}^2/\mu\text{s}$, $k = 160 \text{ W/mK}$, $R_i = 91\%$. There are uncertainties concerning the exact spatial and temporal distribution of the energy deposition. Thus, the parameters of the laser source model have been selected to approximately reproduce the direct signal from.

Figures 4.8 and 4.9 show the experimental (left column), and the numerically predicted (right column) signals at the receiver when the laser is located at six different positions relative to the left face of the notch. The receiver is far enough so that most of the recorded waveforms correspond to Rayleigh waves. In the first plots, the monopolar direct signal and the reflection can be clearly distinguished. As the laser approaches the notch, these signals start to interfere with each other. An apparent increase in peak to peak amplitude and a sharp outwards surface displacement can be observed when the laser is close to the crack. Experiment and simulation show good qualitative agreement. Better quantitative agreement would follow from further adjustment of the parameters of the model.

Figure 4.10 shows the experimental and numerical evolution of the peak to peak

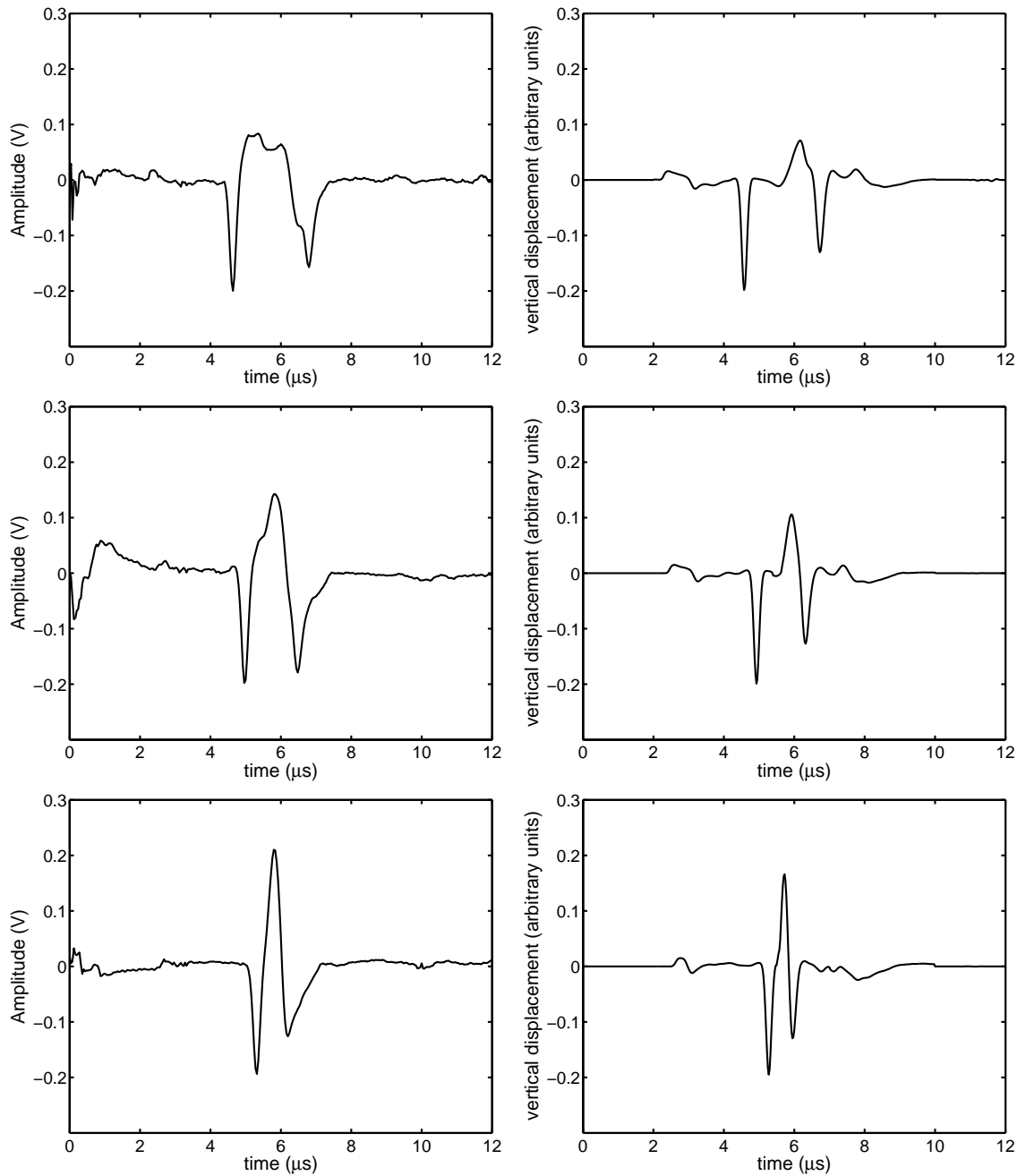


Figure 4.8: Experimental (left column) and simulated (right column) signals detected at the receiver when the laser is located at distances of 3 mm, 2 mm and 1 mm from the left face of the notch.

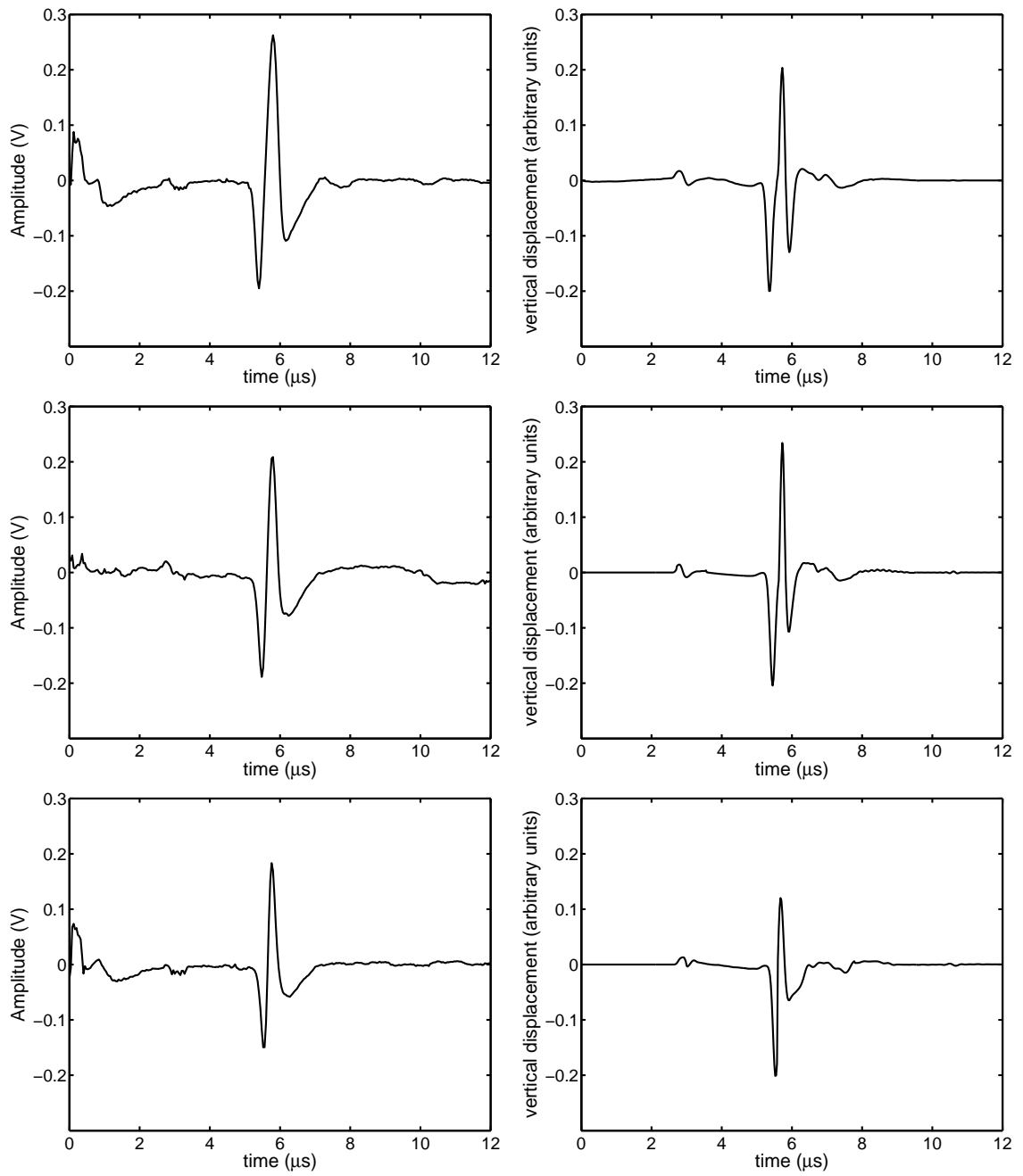


Figure 4.9: Experimental (left column) and simulated (right column) signals detected at the receiver when the laser is located at distances of 0.75 mm, 0.5 mm and 0.25 mm from the left face of the notch.

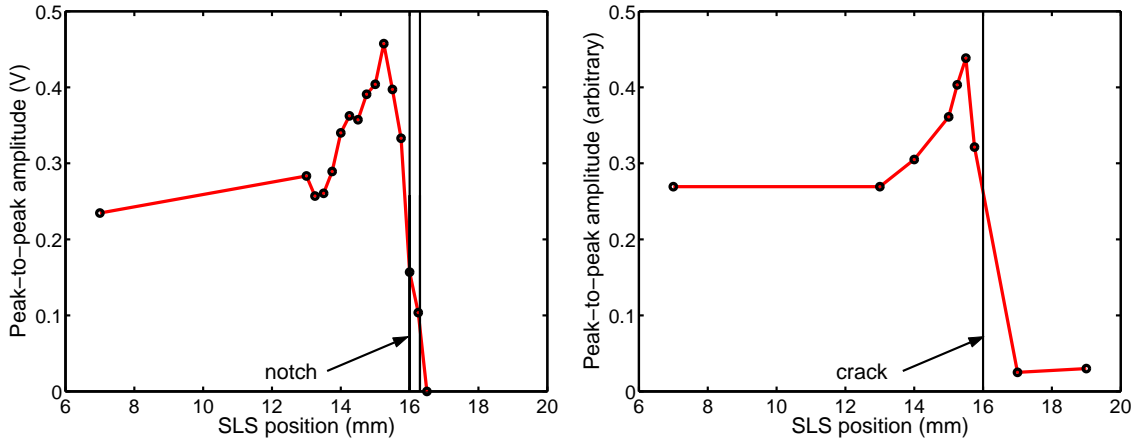


Figure 4.10: Experimental (left) and simulated (right) peak-to-peak amplitude vs. position of the source relative to the crack (SLS position).

amplitude. The characteristic signature of the discontinuity is well predicted by the model. Due to the large depth of the crack, a very small signal is predicted when the laser impinges of the right side of the notch. This signal cannot be distinguished from experimental records.

4.4.2 SLS simulation for a small surface-breaking crack

The illustrative theoretical analysis of a small surface-breaking crack of 0.4 mm depth is reported in this Section. The material and laser parameters are those of the example in Section 4.2, and the receiver is located at a distance of 2.4 mm from the plane of the crack. Figure 4.12 shows the simulated time signal at the receiver corresponding to the three representative positions of the laser relative to the crack: far ahead (I), very close to (II) and far behind (III) the crack (see Fig. 4.11). Again, the qualitative features observed in experiments are reproduced by the model.

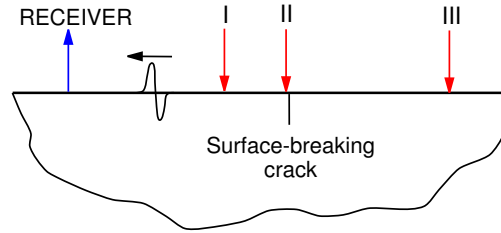


Figure 4.11: Configuration for the SLS technique. Three positions of the laser line-source (I,II, and III) are displayed.

When the laser source is far away from the crack, the direct signal can be clearly differentiated from the reflection. The direct signal is a monopolar inward displacement, as should be expected since the crack at sufficient distance from the illuminated region not to affect the generation process. Thus, the shape of the direct signal agrees with those shown in Fig. 4.3 for laser generation in a defect-free half-space. The reflected signal is also a monopolar inward displacement. As the laser source approaches the crack, the signal at the receiver becomes clearly bipolar and its amplitude increases significantly. This phenomenon could be related to scattering of body waves and mode conversion at the corner edge of the crack, as well as changes in the generation condition.

The peak-to-peak amplitude and the maximum frequency of the Rayleigh wave have been plotted versus the SLS position (see Fig. 4.13). The proposed model reproduces the characteristic variations observed experimentally as the SLS passes over the defect (Kromine et al., 2000a).

It should be noted that the difference between the amplitude level far ahead and far behind the crack is related to the depth of the crack relative to the center wavelength of the generated Rayleigh surface wave. Here, the depth of the crack is much smaller than the center wavelength, so that a substantial portion of the

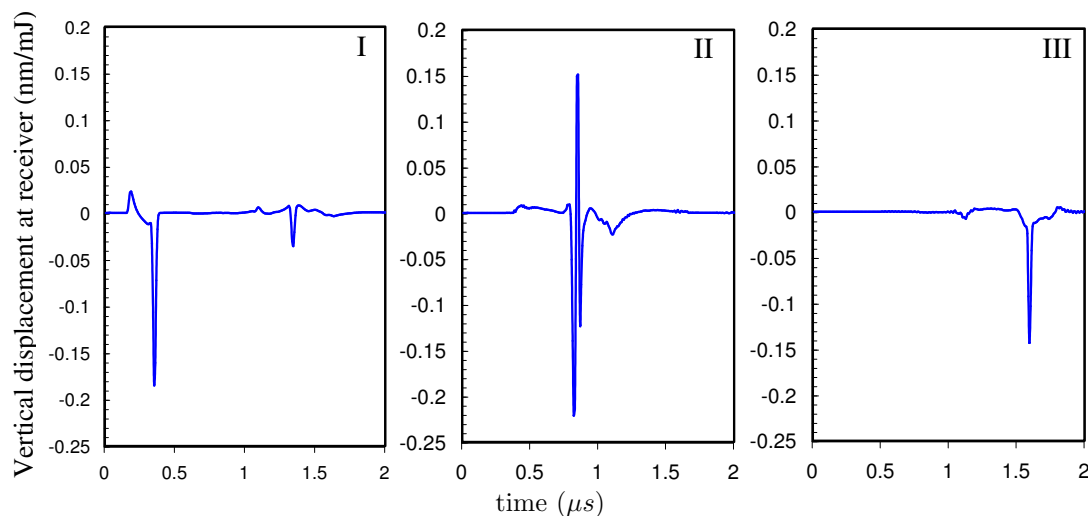


Figure 4.12: Characteristic time signal at receiver simulated for three different positions of the laser source relative to the crack.

incident energy is transmitted past the crack. Such a small crack produces weak echoes, and would be difficult to detect by a conventional technique. By contrast, Fig. 4.13 shows that the increase in the peak-to-peak amplitude as the laser source approaches the position of the crack is significant even for such a small crack. These results illustrate the enhanced sensitivity of the SLS technique as compared to conventional methods. It also illustrates the potential capabilities of this technique in the sizing of the defect.

4.5 Conclusions

A model for the Scanning Laser Source (SLS) technique for the ultrasonic detection of surface-breaking cracks has been presented. The generation of ultrasound by a line-focused laser source on a two-dimensional homogeneous, isotropic, linearly

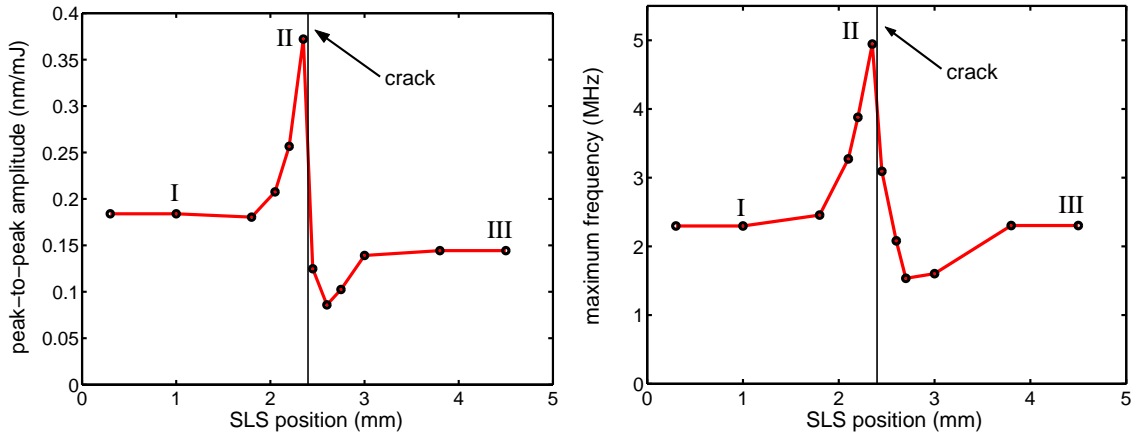


Figure 4.13: Simulated signatures of the defect in the ultrasonic amplitude (left) and the maximum frequency (right) of the generated signal as the laser source scans over a surface-breaking crack.

elastic half-space in the presence of a surface-breaking crack has been analyzed. The modeling approach is based on a decomposition of the generated field in the presence of the defect into the incident and the scattered fields. The incident field is that generated by the laser on a defect-free half-space. A thermoelastic model has been used which takes account of the effects of thermal diffusion from the source, as well as the finite width and duration of the laser source. The scattered field incorporates the interactions of the incident field with the discontinuity. It has been analyzed numerically by the boundary element method. A special treatment of the infinite boundary has been used which eliminates spurious reflections from the ends of the computational boundary. The SLS simulations are obtained by superposition of these two fields.

It is shown that the experimentally observed features characterizing the presence and size of surface-breaking cracks are well reproduced by the model. A comparison

of experimental and simulated signals at the receiver for the case of a large notch shows good qualitative agreement. Further adjustment of the parameters of the model is needed for a better quantitative agreement. An illustrative example with a very small surface-breaking crack demonstrates the ability of this inspection method to detect cracks smaller than the wavelength of the generated Rayleigh wave.

Chapter 5

Modeling of acoustic emission from surface-breaking and buried cracks

A computational study of the acoustic emission from nucleating surface-breaking and buried cracks, and the generated surface motions in elastic two-dimensional half-spaces are presented. This study benefits from the numerical technique developed in Chapter 3. Acoustic emission is potentially an advantageous NDE technique for continuously monitoring structures in service, and provides “real time” information of failure events occurring in the entire volume of the specimen. It presents practical and theoretical difficulties, such as the low signal-noise ratio, and the fact that the displacements at the surface due to the elastic waves radiated from a fracture event depend on the entire geometry of the specimen. This last difficulty is partially addressed here by considering the interactions of radiated stress-waves and the free surface of the half-space.

5.1 Introduction

Acoustic emissions (AEs) are transient stress waves within solids radiated from localized sudden changes in the stress state. They are usually associated with damage events in the material, such as crack nucleation and growth, plastic activity, or various debonding and fracture mechanisms in composite materials. This wave motion propagates through the solid and eventually produces disturbances in the surface, which in principle can be detected. Thus, acoustic emission can be used to monitor the damage activity in specimens, provided that the generated signals are large enough relative to the noise level. Acoustic emission techniques have been used in various situations, from analyzing the development of texture in martensitic materials (Marketz et al., 2003), to the monitoring of corrosion processes and welds in pressure vessels and bridges in service. Acoustic emission has also been applied to monitoring the fatigue crack growth in laboratory tests. A particularly fertile field of application is the analysis of damage in composite materials containing at least a brittle phase (Mummery et al., 1993).

Acoustic emission techniques are quite different from other nondestructive testing methods since internal flaws developing or evolving in all the sample can be detected by taking measurements in a limited region of the surface of the sample. Furthermore, AE techniques allow for continuous monitoring of components while they are in use, and damage events are active. This contrasts with conventional nondestructive techniques which analyze the integrity of components after all events have occurred. Nevertheless, AE as a nondestructive testing technique presents several weaknesses. Due to reflections with boundaries and other features of the sample, the recorded signals depend on the overall structure. Therefore, it is very difficult

to establish a direct correspondence between a disturbance on the surface and the particular event that caused it. On the other hand, the detection threshold is often hindered by the background noise, and weak AE events may remain unnoticed. This is particularly important since the AE signals cannot be enhanced. Another drawback of AE testing is its irreproducibility; once an event has occurred and the associated disturbance has decayed, it is not possible to record it again. As noted by Scruby (1985), a more fundamental difference between AE techniques and conventional NDE methods is the fact that the former detects the evolution of damage, rather than the level of damage itself. While in conventional NDE techniques the detection threshold is limited by the absolute size of the defect, detectability of AE signals depends on the rate of defect growth. Due to this inherent feature, AE is particularly useful for brittle materials, while for ductile materials significant defect growth may remain unnoticed (Achenbach and Harris, 1979; Scruby, 1985).

Due to the above mentioned difficulties to quantitatively interpret acoustic emissions, a statistical approach has often been followed. Cumulative counts of AE events are often used to characterize the different phases that lead to failure in laboratory fatigue tests (Gong et al., 1998; Pensec et al., 2000). However, increasing attention is being drawn to the waveforms of individual damage events. For instance, in Shi et al. (2000), the characteristic signals during the initial micro-cracking, further growth, and coalescence of micro-cracks into localized cracks complement the statistical analysis of the process. Similar attention to the individual waveforms is present in other experimental studies (Choi et al., 2000).

Theoretical efforts have been made to quantitatively analyze AE events. One approach borrowed from seismology consists on the representation of the AE pro-

cess by point-sources, analogously to the shear dipole point representation in laser generation of ultrasound (Scruby et al., 1980). The force dipole tensor provides a simple and convenient way to represent various types of fracture events, while retaining the fundamental physics (Scruby, 1985). This approach however does not account for the finite extent of the defect, and is therefore valid only in the far field. Besides, it assumed that all the stress changes in the fracture event occur simultaneously, i.e. it does not address the dynamic crack propagation. A more detailed asymptotic analysis including the finite size, the curvature of the crack front, and the crack propagation speed in an unbounded solid has been developed by Achenbach and Harris (1979). In particular, their analysis showed that brittle events generate stronger acoustic emission signals than ductile crack propagation. Similar analysis of the stress-waves radiated from sudden activity at the crack tip in an infinite body has been reported by Rose (1981). Harris and Pott (1984) analyzed the disturbances generated by the fracture processes of a buried penny-shaped crack on the free surface of a half-space.

In this Chapter, the quantitative characterization of AE events is explored computationally by a selected set of examples. The acoustic emission from nucleating surface-breaking and buried cracks is considered, and the generated surface motions in a two-dimensional homogeneous, isotropic, linearly elastic half-space are analyzed by the boundary element method. The numerical approach allows to consider defects of finite sizes, and analyze the surface disturbances both in the near and far fields.

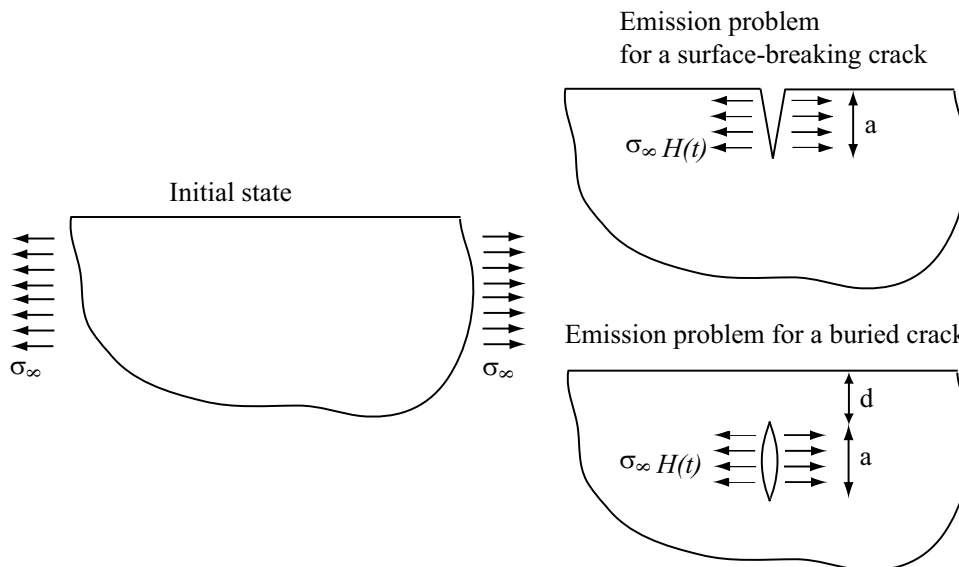


Figure 5.1: Modeling approach to the nucleation of surface-breaking and buried cracks.

5.2 Modeling approach

We consider a homogeneous, isotropic, linearly elastic half-space subject to a uniform tensile stress at infinity σ_∞ parallel to the surface (see Fig. 5.1). The general approach is similar to that of Chapter 4, by which the total field is decomposed into the incident and emitted fields (see Fig. 4.2). The uniform stress field can be understood as a static incident field. The nucleation of a vertical crack is viewed as a sudden release of the corresponding traction on the crack faces. Consequently, it is analyzed by considering the field generated by the sudden application of a horizontal traction of $-\sigma_\infty H(t)$ on the crack faces, $H(t)$ being the Heaviside step function. Thus, similarly to the point-source representation, we assume that all the changes in the source occur simultaneously. We consider surface-breaking cracks, as well

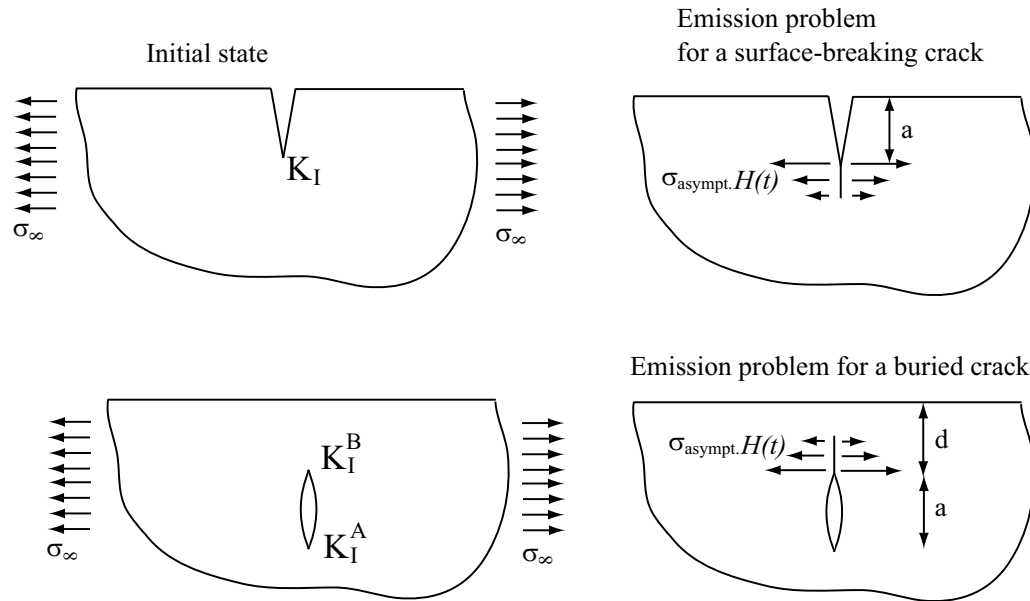


Figure 5.2: Modeling approach to the propagation of surface-breaking and buried cracks.

as buried cracks. Crack growth is modeled by suddenly releasing the asymptotic crack tip field (Tada et al., 2000), as illustrated in Fig. 5.2. Again, it is clear that this approach does not address the dynamic crack propagation phenomenon. Furthermore, the increment of the crack must be small compared to other dimensions of the problem for the asymptotic crack field solution to be valid. A singular traction quarter-point (STQP) element has been used to reproduce the $r^{-1/2}$ singularity of the asymptotic stress field at the crack tip. By displacing the mid-node of a quadratic boundary element with straight-line geometry to a quarter of its length and adequately modifying the element shape functions, the interpolated traction field in the element exhibits the appropriate asymptotic behavior at the crack tip (Blandford et al., 1981).

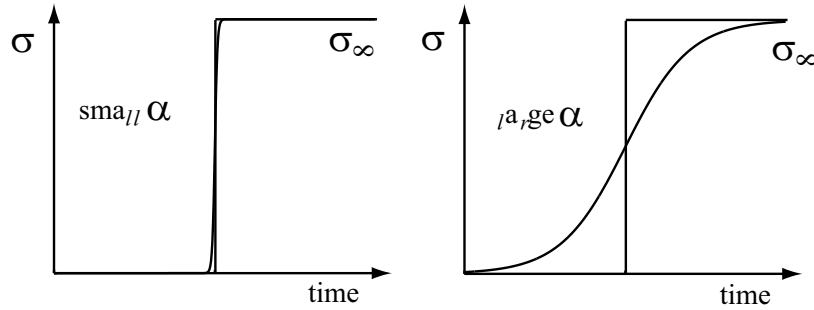


Figure 5.3: Regularized S-shaped step

The release of the stress in the crack faces is treated numerically by replacing the Heaviside step function by S-shaped functions $S_\alpha(t)$. The sharpness of this regularized step, which is controlled by the parameter α , is a simple model for the brittleness or ductility of the fracture process. The considered S-shaped functions are of the form (see Fig. 5.3)

$$S_\alpha(t) = \frac{1}{1 + e^{(t-t_0)/\alpha}}, \quad (5.1)$$

where t_0 is a time shift. In the numerical examples presented in Section 5.3, the values adopted for the parameters are: $\alpha = 0.08$ and $t_0 = 0.43\mu s$, which correspond to a brittle event.

The above described elastodynamic problems for a two-dimensional half-space are solved numerically by the direct frequency domain boundary element method with quadratic interpolations. The symmetry of the emission problems allows us to restrict the analysis to a quarter-space. The analysis of wave propagation in two-dimensional elastic quarter-spaces presents some difficulties, due to the propagation

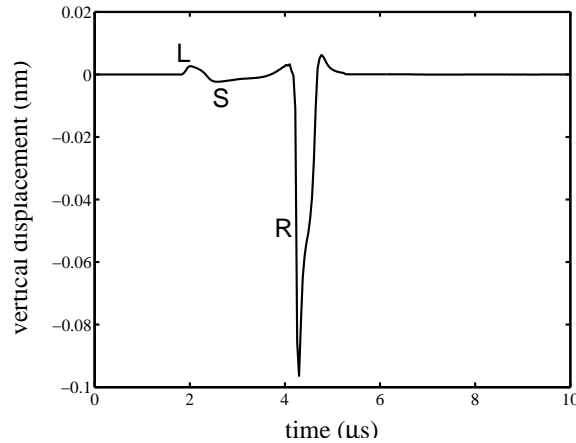


Figure 5.4: Surface normal displacement due to the acoustic emission from the nucleation of a very small surface-breaking crack ($a = 10\mu\text{m}$) at a distance of 12.0 mm from the plane of the crack. The labels L, S and R denote longitudinal, shear and Rayleigh surface waves, respectively.

of non-decaying Rayleigh waves along the unbounded surface. The numerical technique in Chapter 3 provides a convenient treatment of the infinite boundary which allows the undamped Rayleigh waves to escape the computational domain without producing spurious reflections.

5.3 Numerical simulations

As a first example, we study the acoustic emission from a very small nucleating surface-breaking crack. In the limit, the nucleation of a small surface-breaking crack near the surface can be modeled as a surface dipole. As noted by Scruby (1985), this representation is qualitatively similar to the shear traction dipole model for laser generation of ultrasound. Figure 5.4 shows that indeed, for a small, nu-

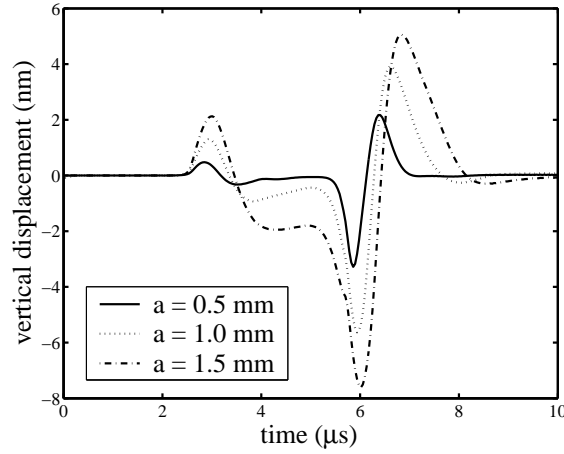


Figure 5.5: Surface normal displacement due to the acoustic emission from the nucleation of surface-breaking cracks of different lengths a at 16.0 mm distance from the plane of the crack.

creasing surface-breaking crack, the generated far field waveform tends to the characteristic monopolar Rayleigh-wave-dominated signal generated by a concentrated line-focused laser source with impulsive time dependence for the pulse (see Chapter 2).

The asymptotic analysis presented by Scruby (1985) predicts that the peak amplitude A of the acoustic emission pulse is proportional to the rate of change of size of the defect, i.e. $A \propto \Delta a / \Delta t$. Figure 5.5 shows the waveforms corresponding to the nucleation of three surface-breaking cracks of different sizes, for a fixed $S_\alpha(t)$, i.e. for a fixed Δt . For increasing Δa , we observe in the waveforms the corresponding increases in the peak amplitude, consistent with the predictions by Scruby (1985). Note that the reported surface disturbances are recorded far enough from the defect to be considered far field. Closer to the nucleating crack, these trends are not so clear. The increasing length of the nucleating crack also reflects in the extent of the

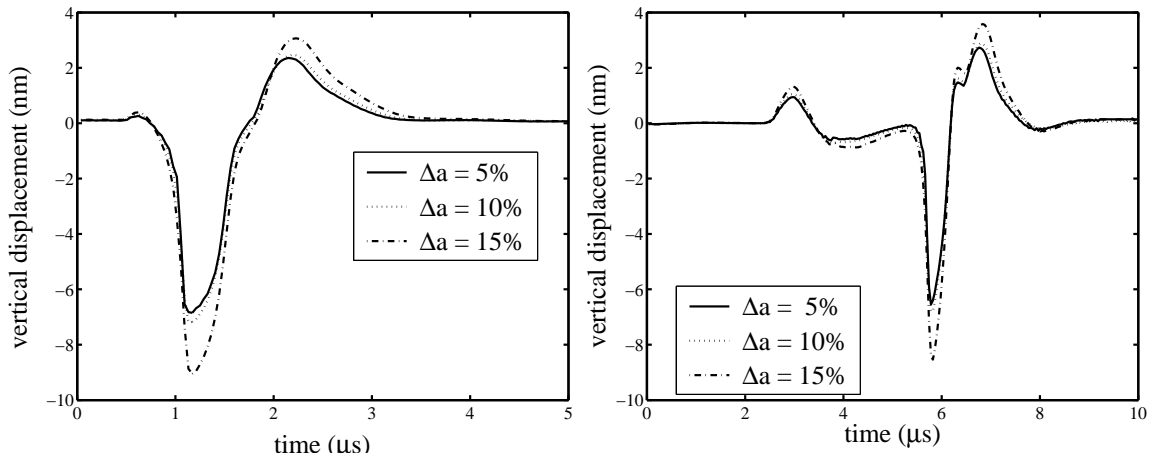


Figure 5.6: Surface normal displacement due to the acoustic emission from the propagation of a surface-breaking crack ($a = 1.0\text{mm}$) for different growth lengths Δa , at distances of 3 mm (left) and 16 mm (right) from the plane of the crack.

time signal.

The same trend is observed in the propagation of a surface-breaking crack. Three different growths Δa have been considered for a fixed $S_\alpha(t)$, i.e. for a fixed Δt , and the corresponding waveforms at the surface are depicted in Fig. 5.6 for distances of 3 mm and 16 mm from the plane containing the crack.

The acoustic emissions from the nucleation and propagation of buried cracks are studied next. Figure 5.7 shows the normal surface disturbances originated from the nucleation of three surface-breaking cracks of different sizes, for a given depth defined by the midpoint of the crack. Similarly to the case of surface-breaking cracks, the peak amplitude increases with the crack size for a given stress release rate.

Figure 5.8 presents surface normal displacements from the propagation of a crack

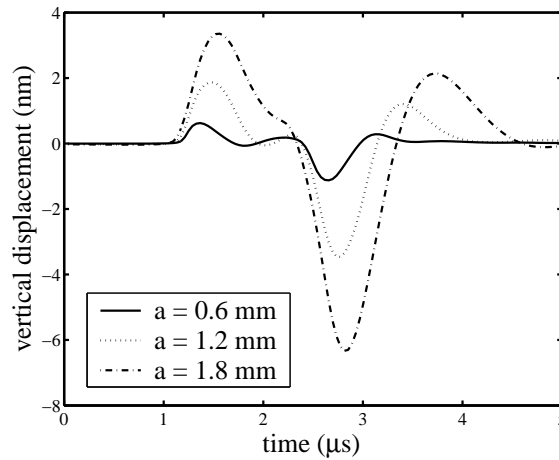


Figure 5.7: Surface normal displacement due to the acoustic emission from the nucleation of buried cracks of different lengths a at a distance of 5.0 mm from the plane of the crack. The midpoints of the cracks are located at a depth $d = 5.0$ mm beneath the surface.

of 1.0 mm length buried a distance of 1.0 mm from the surface to the midpoint of the crack. The crack is assumed to propagate upwards since the crack tip closer to the surface exhibits a larger SIF (Tada et al., 2000). Three different crack growth extents are considered and again the peak amplitude increases with increasing crack growth length for a fixed Δt . Qualitatively, the waveforms for a nucleating and a propagating buried crack are quite similar. It is apparent that in the waveforms shown in Fig. 5.8 the Rayleigh wave component is more significant due to the fact that the cracks in this case are closer to the surface. The effect of the depth of the crack on the surface displacement waveforms has been studied by considering the nucleation of crack of a specific size located at different distances beneath the surface. The corresponding surface disturbances at a distance of 5.0 mm from the plane of the crack are shown in Fig. 5.9. As pointed out, the relative significance of

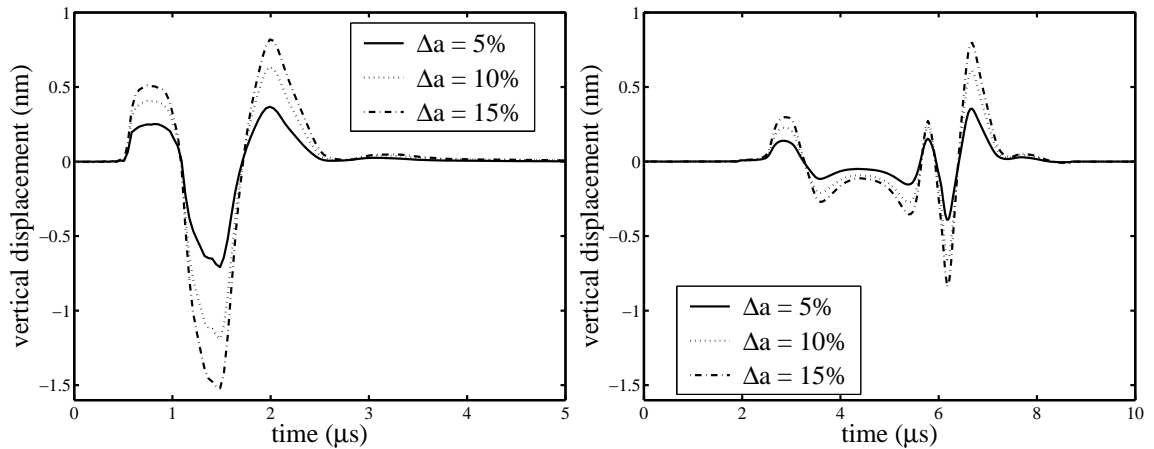


Figure 5.8: Surface normal displacement due to the acoustic emission from the propagation of a buried crack ($a = 1.0$ mm and $d = 0.5$ mm) for different growth lengths Δa , at distances of 4 mm (left) and 16 mm (right) from the plane of the crack.

the Rayleigh wave component with respect to the body wave components decreases as the crack depth increases.

In addition, it can be noted in Fig. 5.9 that the amplitude of the signals exhibit a maximum for an intermediate depth which suggests an angular dependency in the amplitude of acoustic emission signals. This has been further investigated by considering the variation along the surface of the half-space of the acoustic emission from a specific buried crack. Figure 5.10 displays the normal surface displacements at different observation points due to the nucleation of a crack of length $a = 1.0$ mm located at a distance of $d = 1.0$ mm beneath the surface. It can be noted that as the observation point departs from the crack position, the amplitude increases, reaches a maximum, and then decreases in the far-field. This observation is consistent with the results on the angular variation of the amplitude of the acoustic emission

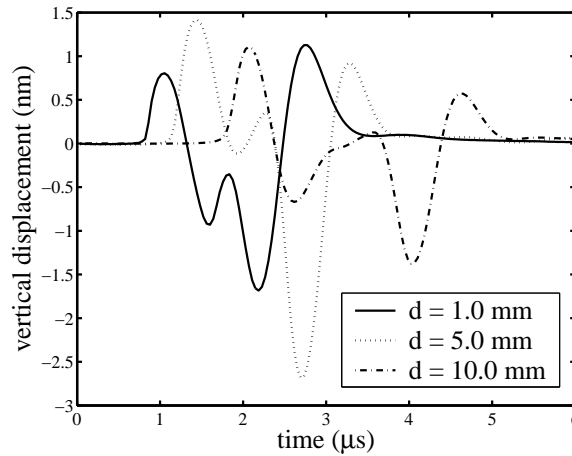


Figure 5.9: Surface normal displacement due to the acoustic emission from the nucleation of buried cracks of length $a = 1.0$ mm at a distance of 5.0 mm from the plane of the crack. The midpoints of the cracks are located at different depths d beneath the surface.

reported by Achenbach and Harris (1979).

5.4 Conclusions

The acoustic emissions from surface-breaking and buried cracks have been explored. A computational approach based on the boundary element method has been implemented. The treatment of the infinite extent of the boundary described in Chapter 3 has been useful. This technique produces numerical solutions which are highly accurate everywhere in the computational domain and for all computed times. This is particularly useful for studies of acoustic emission, since the observation point, which is often located far from the source region, can be brought close to the truncation point without loss of accuracy.

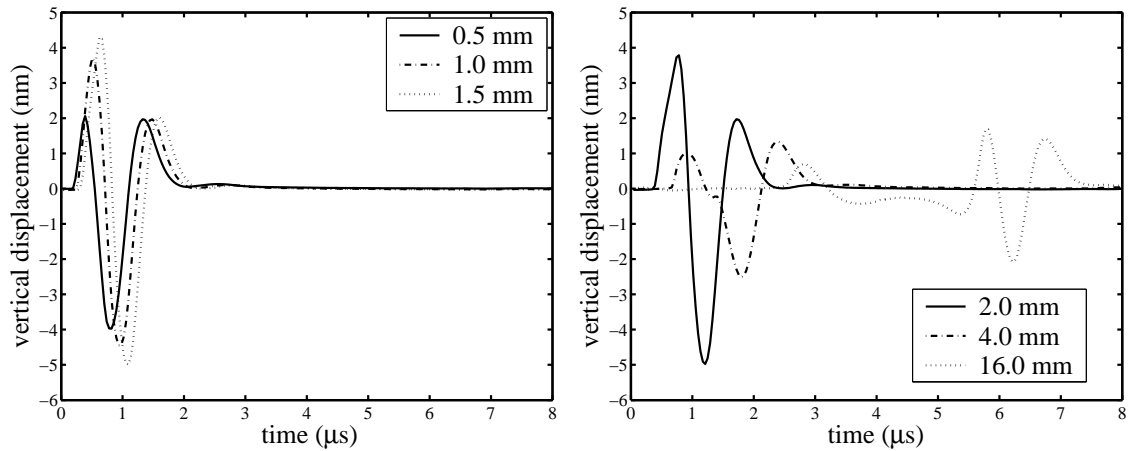


Figure 5.10: Surface normal displacement due to the acoustic emission from the nucleation of a buried crack ($a = 1.0$ mm and $d = 1.0$ mm) at different distances from the plane of the crack.

It has been shown that in the limit of a small nucleating surface-breaking crack, the surface disturbances tend to those generated by a shear dipole at the surface, as has been pointed out in previous studies. We have analyzed the effect of the size of the nucleating crack and the length of the crack growth for both surface-breaking and buried cracks. In addition, we have studied the effect of the buried depth in the surface disturbances originated from nucleating buried cracks. The analysis of the acoustic emission signals for nucleating buried cracks at different observation locations along the surface of the half-space has shown evidence of an angular dependence consistent with previous theoretical studies.

Chapter 6

Conclusions

A model for the Scanning Laser Source (SLS) technique for the ultrasonic detection of surface-breaking cracks has been presented. The generation of ultrasound by a line-focused laser source on a two-dimensional homogeneous, isotropic, linearly elastic half-space in the presence of a surface-breaking crack has been analyzed. The modeling approach is based on a decomposition of the generated field in the presence of the defect into the incident and the scattered fields, by virtue of linear superposition.

The incident field is that generated by line-focused laser illumination of a defect-free half-space. The model is obtained by solving the corresponding thermoelastic problem in plane strain, rather than by superposition of available three-dimensional solutions for the axially symmetric source. The thermoelastic problem has been solved by Fourier–Laplace transform techniques. The solutions in the transformed domain have been presented in detail. The inversion of the transforms has been performed numerically. The model takes account of the effects of thermal diffusion and optical penetration, as well as the spatial and temporal distribution of the source. Each of these effects can be easily neglected in the complete thermoelastic model

by taking appropriate limits. By neglecting all of them, the well-known surface dipole model is recovered. Based on simple elasticity considerations, the strength of the dipole has been related to the heat input and certain material properties. The expression differs from that available in the literature by a factor related to the presence of the free surface. Theoretical waveforms for normal surface displacements due to the Rayleigh wave have been compared with experimental measurements available in the literature and excellent quantitative agreement has been found. This result shows that the proposed thermoelastic model provides a quantitative basis for generation of ultrasound by line-focused laser illumination. The effect of thermal diffusion has been investigated. As expected, this effect is significant near the heated region, while it is not noticeable in the far-field. The thermoelastic model predicts the precursor spike on the waveforms on the epicentral axis, which results from the subsurface sources arising in metals mainly due to thermal diffusion. A parametric study of the effects of the width of the laser line-source and the duration of the pulse has shown that the generated signal becomes broader and its magnitude decreases as the laser line-source is spread out in space and time. Stress waveforms on the epicentral axis and at the surface, and snapshots of the stress distribution illustrate the different thermoelastic mechanisms under line-focused laser illumination, which have been explained by intuitive arguments.

The scattered field is defined as that generated on the cracked half-space by suitable tractions acting on the faces of the crack. These tractions are equal and opposite to those generated by the incident field in the uncracked half-space when evaluated on the plane of the crack. This problem is treated as an isothermal elastic problem of two-dimensional wave diffraction by a surface-breaking crack in a half-

space, and solved numerically by the boundary element method (BEM).

The infinite surface of the domain has to be truncated for numerical calculation purposes. The simple truncation introduces spurious reflections from the ends of the computational boundary, mainly due to undamped Rayleigh waves, that distort the numerical solution in the region close to the truncation point. The developed method exploits the knowledge of the asymptotic behavior of the solution – here Rayleigh surface waves are assumed to dominate the far-field solution – to adequately correct the BEM displacement system matrix for the truncated problem to account for the contribution of the omitted part of the boundary. The reciprocity theorem of elastodynamics allows for a convenient computation of this contribution involving the same element integrals that form the original BEM system. The proposed method is easy to implement and, in the case of a quarter-space, it comes at essentially no additional cost as compared to the simple truncation of the boundary. The accuracy of the solution provided by the proposed model depends on the accuracy of the assumption that Rayleigh waves strongly dominate at the end points of the computational domain. However, once the computational domain is extended far enough from the source region for this assumption to hold, then, unlike the simply truncated solution, the corrected solution is accurate everywhere in the computational domain and for all computed times. In situations where the region of interest extends far beyond the source region where waves are generated, the proposed method can reduce the extent of the computational boundary.

The SLS simulations are obtained by superposition of these two fields. It is shown that the experimentally observed features characterizing the presence and size of surface-breaking cracks are well reproduced by the model. A comparison of

experimental and simulated signals at the receiver for the case of a large notch shows good qualitative agreement. Further adjustment of the parameters of the model is needed for a better quantitative agreement. An illustrative example with a very small surface-breaking crack demonstrates the ability of this inspection method to detect cracks smaller than the wavelength of the generated Rayleigh wave.

The numerical technique for the treatment of wave propagation problems in a two dimensional half-space is applied to the analysis of acoustic emissions from nucleating surface-breaking and buried cracks. It has been shown that in the limit of a small nucleating surface-breaking crack, the surface disturbances tend to those generated by a shear dipole at the surface. We have analyzed the effect of the size of the nucleating crack, as well as the surface disturbances for various observation locations.

References

- Achenbach, J. (1973). *Wave propagation in elastic solids*. Amsterdam: North-Holland, Elsevier.
- Achenbach, J. and J. Harris (1979). Acoustic emission from a brief crack propagation event. *ASME Journal of Applied Mechanics* 46, 107–112.
- Arias, I. and J. Achenbach (2003a). A model for the ultrasonic detection of surface-breaking cracks by the scanning laser source technique. *Submitted for publication*.
- Arias, I. and J. Achenbach (2003b). Rayleigh wave correction for the bem analysis of two-dimensional elastodynamic problems in a half-space. Submitted for publication.
- Arias, I. and J. Achenbach (2003c). Thermoelastic generation of ultrasound by line-focused laser irradiation. *International Journal of Solids and Structures*. Accepted for publication.
- Beer, G. and J. Watson (1989). Infinite boundary elements. *International Journal for Numerical Methods in Engineering* 28, 1233–1247.
- Bernstein, J. and J. Spicer (2000). Line source representation for laser-generated ultrasound in aluminum. *Journal of the Acoustical Society of America* 107(3), 1352–1357.
- Blandford, G., A. Ingraffea, and J. Liggett (1981). Two-dimensional stress intensity factor computations using the boundary element method. *International Journal for Numerical Methods in Engineering* 17, 387–404.
- Bu, S. (1997). Infinite boundary elements for the dynamic analysis of machine foundations. *International Journal for Numerical Methods in Engineering* 40(21), 3901–3917.

- Choi, J., J. Luo, and I. Daniel (2000). Analysis of acoustic emission waveforms from propagating fatigue crack. In D. Thompson and D. Chimenti (Eds.), *Review of Progress in Quantitative Nondestructive Evaluation*, Volume 19, pp. 351–358. AIP Press, New York.
- Crump, K. (1976). Numerical inversion of laplace transforms using a fourier series approximation. *Journal of the ACM* 23(1), 89–96.
- Cruse, T. (1987). Fracture Mechanics. In *Boundary element methods in mechanics*, pp. 333–365. Amsterdam: North-Holland. D.E. Beskos (ed.).
- Domínguez, J. (1993). *Boundary elements in dynamics*. Computational mechanics publications, Elsevier applied science.
- Domínguez, J. and T. Meise (1991). On the use of the bem for wave propagation in infinite domains. *Engineering Analysis with Boundary Elements* 8(3), 132–138.
- Doyle, P. (1986). On epicentral waveforms for laser-generated ultrasound. *Journal of Physics D* 19, 1613–1623.
- Doyle, P. and C. Scala (1996). Near-field ultrasonic rayleigh waves from a laser line source. *Ultrasonics* 34, 1–8.
- Fomitchov, P., A. Kromine, Y. Sohn, S. Krishnaswamy, and J. Achenbach (2002). Ultrasonic imaging of small surface-breaking defects using scanning laser source technique. In D. Thompson and D. Chimenti (Eds.), *Review of Progress in Quantitative Nondestructive Evaluation*, Volume 21, pp. 356–362. AIP Press, New York.
- Gong, Z., D. DuQuesnay, and S. McBride (1998). Measurement and interpretation of fatigue crack growth in 7075 aluminum alloy using acoustic emission monitoring. *Journal of Testing and Evaluation* 26(6), 567–574.
- Harris, J. and J. Pott (1984). Surface motion excited by acoustic emission from a buried crack. *ASME Journal of Applied Mechanics* 51, 77–83.
- Heymsfield, E. (1997a). Infinite domain correction for anti-plane shear waves in a two-dimensional boundary element analysis. *International Journal for Numerical Methods in Engineering* 40(5), 953–964.

- Heymsfield, E. (1997b). Infinite domain correction for in-plane body waves in a two-dimensional boundary element analysis. *International Journal for Numerical Methods in Engineering* 40(9), 1687–1700.
- Hutchins, D. (1988). Ultrasonic generation by pulsed lasers. In *Physical Acoustics*, Volume XVIII, Chapter 2, pp. 21–123. W.P. Mason and R.N. Thurston (Academic, San Diego).
- Kromine, A., P. Fomitchov, S. Krishnaswamy, and J. Achenbach (2000a). Laser ultrasonic detection of surface breaking discontinuities: scanning laser source technique. *Materials Evaluation* 58(2), 173–177.
- Kromine, A., P. Fomitchov, S. Krishnaswamy, and J. Achenbach (2000b). Scanning laser source technique for detection of surface-breaking and sub-surface cracks. In D. Thompson and D. Chimenti (Eds.), *Review of Progress in Quantitative Nondestructive Evaluation*, Volume 19, pp. 335–342. AIP Press, New York.
- Kromine, A., P. Fomitchov, S. Krishnaswamy, and J. Achenbach (2001). Detection of subsurface defects using laser based technique. In D. Thompson and D. Chimenti (Eds.), *Review of Progress in Quantitative Nondestructive Evaluation*, Volume 20, pp. 1612–1617. AIP Press, New York.
- Lamb, H. (1904). On the propagation of tremors over the surface of an elastic solid. *Philosophical Transactions of the Royal Society (London)* A303, 1–42.
- Li, Z. and J. Achenbach (1991). Interaction of a rayleigh wave with a disbond in a material interphase normal to a free surface. *Ultrasonics* 29, 45–52.
- Marketz, W., F. Fischer, and H. Clemens (2003). Deformation mechanisms in TiAl intermetallics—experiments and modeling. *International Journal of Plasticity* 19, 281–321.
- McDonald, F. (1989). Practical quantitative theory of photoacoustic pulse generation. *Applied Physics Letters* 54(16), 1504–1506.
- McDonald, F. A. (1990). On the precursor in laser-generated ultrasound waveforms in metals. *Applied Physics Letters* 56(3), 230–232.
- Mummery, P., B. Derby, and C. Scruby (1993). Acoustic emission from particulate-reinforced metal matrix composites. *Acta Metallurgica et Materialia* 41(5), 1431–1445.

- Niwa, Y., S. Hirose, and M. Kithara (1986). Application of the boundary integral equation (bie) method to transient response analysis of inclusions in a half-space. *Wave Motion* 8, 77–91.
- Pensec, R., A. Laksimi, C. Herve, and M. Cherfaoui (2000). Discrimination of flaws evolution patterns during pressure vessels static and dynamic cycles of loading thanks to the acoustic emission method. In D. Thompson and D. Chimenti (Eds.), *Review of Progress in Quantitative Nondestructive Evaluation*, Volume 19, pp. 375–382. AIP Press, New York.
- Press, W., B. Flannery, S. Teulosky, and W. Vetterling (1986). *Numerical recipes: the art of scientific computing* (third ed.). Cambridge University Press.
- Rose, L. (1981). The stress-wave radiation from growing cracks. *International Journal of Fracture* 17, 45–60.
- Rose, L. (1984). Point-source representation for laser-generated ultrasound. *Journal of the Acoustical Society of America* 75(3), 723–732.
- Royer, D. (2001). Mixed matrix formulation for the analysis of laser-generated acoustic waves by a thermoelastic line source. *Ultrasonics* 39, 345–354.
- Sanderson, T., C. Ume, and J. Jarzynski (1997). Laser generated ultrasound: a thermoelastic analysis of the source. *Ultrasonics* 35, 115–124.
- Schleichert, U., K. Langenberg, W. Arnold, and S. Fassbender (1989). A quantitative theory of laser-generated ultrasound. In D. Thompson and D. Chimenti (Eds.), *Review of Progress in Quantitative Nondestructive Evaluation*, Volume 8A, pp. 489–496. AIP Press, New York.
- Scruby, C. (1985). *Research techniques in nondestructive testing*, Volume VIII, Chapter Quantitative acoustic emission techniques, pp. 141–210. London: Academic Press.
- Scruby, C., R. Dewhurst, D. Hutchins, and S. Palmer (1980). Quantitative studies of thermally-generated elastic waves in laser irradiated metals. *Journal of Applied Physics* 51, 6210–6216.
- Scruby, C. and L. Drain (1990). *Laser Ultrasonics: Techniques and Applications*. New York: Adam Hilger.

- Shi, Z., J. Jarzynski, S. Bair, S. Hurlebaus, and L. Jacobs (2000). Characterization of acoustic emission signals from fatigue fracture. *Journal of Mechanical Engineering Science* 214(9), 1141–1149.
- Sohn, Y. and S. Krishnaswamy (2002). Mass spring lattice modeling of the scanning laser source technique. *Ultrasonics* 39, 543–552.
- Sohn, Y. and S. Krishnaswamy (2003). *Private communication*.
- Spicer, J. (1991). *Laser ultrasonics in finite structures: comprehensive modelling with supporting experiment*. Ph. D. thesis, The John Hopkins University.
- Spicer, J. and D. Hurley (1996). Epicentral and near epicenter surface displacements on pulsed laser irradiated metallic surfaces. *Applied Physics Letters* 68(25), 3561–3563.
- Tada, H., P. Paris, and G. Irwin (2000). *The stress analysis of cracks handbook* (3rd Ed. ed.). The American Society of Mechanical Engineers.
- Thompson, R. and T. Gray (1986). Use of ultrasonic models in the design and validation of new nde techniques. *Philosophical Transactions of the Royal Society of London. A* 320, 329–340.
- Watson, J. (1979). Advanced implementation of the boundary element method for two- and three-dimensional elastostatics. In *Developments in Boundary Element Methods – I*, pp. 31–63. London: Elsevier Applied Science Publishers. ed. Banerjee P.K. and Butterfield R.
- Wheeler, L. and E. Sternberg (1968). Some theorems in classical elastodynamics. *Archive for Rational Mechanics and Analysis* 31, 51–90.
- White, R. (1963). Generation of elastic waves by transient surface heating. *Journal of Applied Physics* 34(12), 3559–3567.
- Zhang, C., C. Song, and O. Pekau (1991). Infinite boundary elements for dynamic problems of 3-d half-space. *International Journal for Numerical Methods in Engineering* 31, 447–462.